THERMOCHEMISTRY AND PHASE DIAGRAM STUDIES IN THE Cu-In-Ga-Se
SYSTEM

By

MUHSIN IDER

ACKNOWLEDGMENTS

I would like to acknowledge the many people who encouraged and supported me during my graduate career. First, I would like to thank my supervisor, Dr. Tim Anderson, for providing me with his guidance and support during my research. I am grateful to my supervisory committee members for agreeing to be in my defense committee and for offering their insight and expertise in understanding my results. I am grateful to Dr. Crisalle and Dr. Sheng Li for administering many useful discussions during regular CIS group meetings in which I learned many different aspects of my research area and experienced how to be a team member. Dr. Crisalle and Dr. Fan Ren receive my greatest admiration for their professional approach to problems and communication methods. I learned much in Dr. DeHoff's materials thermodynamics class and I would like to thank him for writing a thermodynamics book so comprehensive and so explicable at the same time.

I would like to thank many co-workers in my research group, in particular Dr. Alex Chang, Robert Lowrey, Lei Li Kerr, Serkan Kincal and Suku Kim. I am indebted to Dr. Jianyun Shen, Dr. Weidong Zhuang and Dr. Albert Davydov for sharing their expertise in thermodynamic modeling and calculation software. I would like to thank a group of friends, Omar Bchir, Min Huang and Steve Johnston particularly, for their close friendship and social discussions which helped me feel comfortable when I felt alone and a stranger.

TABLE OF CONTENTS

THERMOCHEMISTRY AND PHASE DIAGRAM STUDIES IN THE CU-IN-GA-SE
SYSTEM

By

Muhsin Ider

MAY 2003

Chair: Timothy J. Anderson
Major Department: Chemical Engineering

Polycrystalline $Cu(In,Ga)Se_2$ and related semiconductors show great potential as alternative materials in production of high efficiency solar cells. This dissertation reports the experimental determination of Gibbs energy changes and phase diagram calculations for selected sections of the Cu-Ga-In-Se system. The Gibbs energy changes were measured with solid-state electrochemical cells and this data along with selected literature data were assessed and model parameters suggested.

The homogeneity range of $\beta\text{-}Cu_{2\text{-}x}Se$ was measured by coulometric titration and the thermodynamic properties for defect species estimated. The composition difference between the Se-rich and the Cu-rich boundaries was measured at 900K. A defect model was developed based on vacancy formation on the Cu sublattice. The gas phase equilibrium data for Cu-Se system and the results of a recent assessment of selenium unary system were used to predict defect concentrations.

A thermodynamic description of the $Cu_2Se-In_2Se_3$ was obtained by optimization of the available phase equilibrium and thermodynamic information along with the direct results of EMF experiments. The Gibbs energy of formation of α-$CuInSe_2$ was directly measured by a solid oxide galvanic cell experiment. The transformation enthalpy and Gibbs energy data for $CuIn_3Se_5$ and $CuIn_5Se_8$ were estimated. The Redlich-Kister model with a 3-coefficient expression was employed to define the Gibbs energy of the liquid phase. The intermediate β-$CuIn_3Se_5$ and γ-$CuIn_5Se_8$ phases were modeled with a 2-coefficient expansion of the Redlich-Kister model. The α and δ modifications of $CuInSe_2$ phases were modeled with a specific sublattice model. A reasonable agreement between the model calculated values and the thermodynamic phase equilibrium data was achieved.

The thermochemistry and phase diagram of GaSe system was critically studied. The activity of Ga was measured along the liquidus between 800-1000K. Selected invariant phase transition temperatures were measured and transition enthalpies were calculated from the EMF measurements. A self-consistent thermodynamic data was obtained. The associated and sublattice models were used to represent the Gibbs energy of the liquid and α-Ga_2Se_3 phases, respectively. The Gibbs energy of formation of $CuGaSe_2$ was measured by an EMF experiment. The phase diagram of Cu-Ga system was calculated and the liquid phase Ga activity measurements was measured for 2 Ga rich compositions.

CHAPTER 1
INTRODUCTION

The development of cheaper, renewable and environmentally benign power generation has always been one of the most popular concerns of mankind. The major conventional energy sources of the world are not only limited but conversion efficiencies and environmental effects such as global warming have recently become fundamental issues. Although various renewable energy sources have been studied and used, there is still not a single renewable source that can accommodate the world's energy needs cheaper than fossil fuels. Power generation with solar photovoltaic modules, however, is rapidly gaining popularity compared to other renewable sources due to the potential for improvements in cost and efficiency.

Photovoltaic (PV) systems are based on the idea of converting solar energy to electrical energy. Photovoltaic technology is used in a wide range of simple systems including small calculators and in more complicated systems such as water pumps, communications equipment, home lightning, and space applications. Photovoltaic modules are usually made up of solid-state semiconductor materials that are constructed so as to work as p-n junctions. The technology has matured to produce dependable and adaptable devices for different weather conditions with considerable conversion efficiencies. The production is flexible since a PV system can be constructed to any size depending on energy requirements. The improvements can also be made for future needs. Although some applications may also require storage of energy, which may increase production costs, the fuel for PV systems is abundant and cheap and environmental

1

benefits make PV modules attractive. PV cells are used both for stand-alone, remote power as well as for utility-connected applications. Because of the rapid growth in industry's production, PV modules find a variety of applications. Although, the largest application potential for PV modules is predicted in areas without grid connection, where they replace conventional diesel generators as an economical alternative, the higher efficiency device development and improvements in production cost could soon make PV technology competitive for all terrestrial applications. Since the marketing and cost are strongly interrelated, it is anticipated that PV power generation systems will become available much cheaper than conventional energy sources. The fact that more than one third of world population live without any access to electricity, and the versatility in application of PV technology in remote areas as well as grid connected applications make this assumption realistic.

French physicist Edmond Becquerel established the first description of photovoltaic effect in 1839. Later studies in solids such as selenium resulted in PV cells converting light to electricity with an efficiency of 2%. However, the major developments in technology did not begin until the 1940`s since the process of producing electric current in a solid material was not exactly understood. In the second half of the 20th century, knowledge of photovoltaic effect was considerably advanced and the process was more fully explained. After the development of the Czochralski crystal growth process and production of highly pure crystalline silicon, which resulted in a photovoltaic cell with an efficiency of 4%, PV conversion efficiencies improved considerably. The current research is implicitly focused on improving power conversion efficiencies, versatility, endurance and reducing production costs.

Parallel to the requirements and developments of the computer industry, most of today's PV modules use wafers made out of silicon. Silicon is a widely available and relatively cheap material. The silicon production technology is very stable and mature. However, significant cost reductions in silicon technology are not very promising due to limitations enforced by production methods and processing conditions. The method requires high-energy input due to high operating temperatures (>1,000°C) and material and handling costs during production are considerable. Hence, many major PV manufacturers are studying alternative materials and processing technologies to improve efficiency and lower cost requirements.

Thin film technology has been considered for some time as an alternative to the single and multi-crystalline wafer technology. Chalcopyrite semiconductors have recently emerged as the most promising absorber materials for thin film solar cell applications. The most considered and studied chalcopyrite material is $CuInSe_2$ (CIS) with a suitable band gap of 1.0 eV for solar cell applications. Thin-film solar cells fabricated with CIS absorber layers are currently holding world-record energy conversion efficiencies. The considerable radiation resistance and long term stability of CIS solar cells facilitate the compound as a promising world leader in the field. It is also predicted that these cells will play a significant role in future space exploration missions. One of the main advantages of thin film and especially CIS based semiconductors is that band gap, defect chemistry and device structure can be modified during the production, obtaining high efficiency production possibilities with less cost. Thin film technology also allows working various substrate materials as well as different temperature ranges and geometric configurations. Many groups have been working on the optimization and characterization of the thin film

deposition and absorber formation and device characteristics of CIS and related compounds. Although some industrial scale production exists, the relation between process parameters in CIS solar cell production and the related material parameters are not yet fully understood. Many different methods were examined for enhancement of grain growth and electrical parameters of the solar cells. Different solid solutions, device structures and doping mechanisms were also investigated. Figure 1.1 summarizes the structural behavior and band gap of some selected I-III-VI$_2$ compounds. However, knowledge of equilibrium nature of binary and ternary compounds is not fully established.
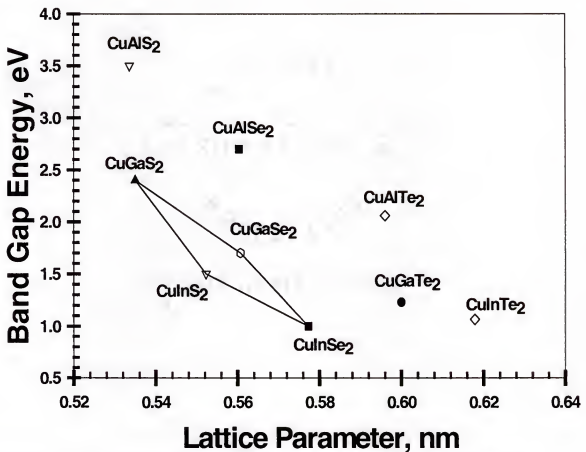
Figure 1.1 Structural behavior and band gap of some selected I-III-VI$_2$ compounds.

Many different aspects related to the production of efficient cell structure are studied. A review of current CuInSe$_2$-based photovoltaic technology and current understanding and future research and development challenges is given by Chang [1] Most of the experimental effort is directed at improving and developing the physical device structure including absorber formation, junction formation, and material and device analyses. Gallium and sulfur addition along with the defect chemistry, alternative hetero-junction process design and different reaction pathways are some of the important research fields. The basis of CuInSe$_2$ (CIS) technology is a highly absorbing p-type semiconductor (p-CIS) combined with an n-type front electrode, which is usually CdS/ZnO. When sunlight strikes the surface of a PV cell, a characteristic built in electrical field provides momentum and direction to light-stimulated electrons, resulting in a flow of current when the solar cell is connected to an electrical load. The efficiency of today's CIS-based solar cells has reached over 21%. This value was achieved recently by NREL as the highest value for any thin film material combination. Parallel to the demands of the rapidly advancing high tech industry and market cost demands, it is desirable to further increase the bandgap of the CIS thin-film solar cells to 1.4 to 1.6 eV for improved module performance. This is usually accomplished by creating solid solutions by addition of other elements such as gallium and sulfur. Several methods of producing layered device structures are studied. In general, thin layers of semiconductor materials each with different properties can be deposited by epitaxial processes. This allows building better designed and more efficient devices with less cost.

CIS shows great potential in polycrystalline form and unlike conventional binary semiconductors (e.g., GaAs or ZnSe), it can tolerate a large range of anion-to-cation off-

stoichiometry (Cu-deficient and/or In-deficient stoichiometries are stable and useful). This brings an advantage in terms of possibilities in band gap tailoring and defect chemistry modifications. However, the full description of the complex behavior of several non-stoichiometric compounds is not completed and the phase diagram optimization of these compounds requires complex thermodynamic modeling. $CuInSe_2$ can be produced with p and n type resistivity characteristics by introduction of native defects, with or without extrinsic impurities. However, the doping mechanism and point defect chemistry of $CuInSe_2$ are not well understood at the fundamental level. It is important to understand these properties to further improve the cell efficiency and reduce the cost of solar energy.

The difficulty in taking this technology to a production level lies in the difficulty in avoiding the formation of undesired defects during deposition that prevent the formation of uniform layers. It is also required to alter defect structure and combine different semiconducting layers for best performance. The knowledge of equilibrium and diffusion characteristics of multi-layer structures becomes most important for better and cheaper process design. A recent publication by Godecke [2] shows the equilibrium structure of this ternary system. The ternary phase relations in CIS system are still not complete and many equilibrium regions are not well studied. Although many experimental studies exist and preliminary experimental results propose some new phases and equilibrium regions, there is still uncertainty on the phase diagram of CIS system. The difficulties arise from uncertainties in experimental observations of multiple non-stoichiometric compounds. Optimization of phase equilibria is also difficult due to problems in modeling of complex compounds and the lack of thermochemical data in

some phase regions. Figure 1.1 shows a schematic of ternary phase relations in Cu-In-Se system proposed by Godecke [2], which is based on his experimental results. There are 15 phases presented in ternary cross-section of Figure 1.1. The α phase ($CuInSe_2$) establishes equilibria with eight solid phases and one liquid phase L_4 in general. The In-Cu boundary introduces η-Cu_7In_3, δ-$Cu_{16}In_9$ and α-Cu equilibria. The β-Cu_2Se high temperature equilibrium phase from the Cu-Se boundary and InSe and In_4Se_3 from the In-Se boundary constitute the other solid phase equilibria. According to Figure 1.1, the α phase also generates phase equilibria with δ_R and δ_H ternary compounds. The compound denoted with the symbol δ_R is defined by Godecke as the large homogeneity compound with the chemical formula of $Cu_1In_3Se_5$. Accordingly, the δ_H phase is defined as the high temperature modification of δ_R phase. These compounds are referred with different homogeneity ranges and different formulas in the literature especially the homogeneity range of high temperature δ_H phase is reported rather wide with compositions corresponding to values lower than stoichiometric α-$CuInSe_2$ and up to compositions that correspond to the $CuIn_3Se_5$. In this work, the stable compound that is in equilibria with the α phase is described by the formula β-$CuIn_3Se_5$ and the high temperature phase is referred to the high temperature modification of α phase with the symbolic representation of δ-$CuInSe_2$. Based on calculations of pseudo-binary section of Cu_2Se-In_2Se_3 phase diagram, the equilibrium phase between the high temperature and low temperature stoichiometric phase of δ-α does not exist at 773K. The stability range of δ-$CuInSe_2$ is also calculated to be rather smaller than Godecke`s results.

Figure 1.1 Isothermal section of Cu-In-Se system at 773K (500 °C)by Godecke [2] along with the binary sub-systems; In-Cu phase diagram assessed by Okamoto [3], Cu-Se and In-Se phase diagrams assessed by Chang [1].

The objectives of this thesis are:

To understand and suggest a general defect equilibrium mechanism for Cu_2Se defect compound through the use of coulometric titration and defect modeling.

To obtain a consistent phase diagram and thermodynamic information for the Cu-In, and Ga-Se systems to give better understanding of processing conditions for solar cell and other semiconductor technology applications.

To investigate and develop consistent computer calculation methods for binary and ternary systems such as CIS and CGS, which include large homogeneity range compounds.

Chapter 2 summarizes the rudimental knowledge for EMF measurements along with thermodynamic descriptions related to the physics of the experimental design. Electrochemical equilibrium is defined and experimental difficulties and important design considerations are also described. Chapter 3 focuses on the general procedure of phase diagram calculations. The physical representation of current optimization methods is discussed. A general overview and optimization capabilities of phase diagram calculations is presented. The importance of solution modeling and predictability of binary and higher order phase diagrams are discussed in Chapter 3. Chapters 4-7 describe EMF experimental studies, data assessment, and phase diagram calculations of selected subsystems in the Cu-In-Ga-Se system.

CHAPTER 2
ELECTROCHEMICAL MEASUREMENTS FOR DETERMINATION OF
ELEMENTAL THERMODYNAMIC FUNCTIONS IN THE CU-IN-GA-SE SYSTEM

Introduction

Electrochemistry is defined as the study of the interchange of chemical and electrical energy. In electrochemistry and ElectroMotiveForce (EMF) measurements, it is usually desired to extract work from chemical reactions in terms of electricity. The EMF theory is based on electrical potential difference measurements between two distinct electrodes by placing a potentiometer into the circuit. This measured potential is an indication of the nature of the chemical reactions and the driving force on electrons to flow in the circuit. This correlation is associated with the Gibbs energy change of processes with the well-known Nernst equation,

$$\Delta G = -nFE \tag{2.1}$$

In general, thermodynamic investigations of appropriate galvanic cells permit the determination of following properties:

1-- Gibbs energy change of chemical reactions in galvanic cells.

2-- Chemical potential or activity measurements or partial pressure.

3-- Reaction enthalpies or transformation enthalpies depending on the phase diagram information.

The solid electrolyte plays the most important role as the rate-limiting step of cell reactions during the experiments. The electrochemical reactions appear on its boundaries and the reaction rates are dependent on the diffusivity and conductivity of charged species through the solid electrolyte. Yittria stabilized zirconia YSZ is used as the solid

10

electrolyte throughout this research. YSZ, is a pure solid O^{2-} ionic conductor and ionic charge transfer is observed usually between 600 and 800 °C. In the temperature ranges of experimental study of this work, the electrical conductivity by electronic species is negligible compared to ionic conductivity, which means that the electrical conduction is driven by ionic species. The maximum electrical work done on the system is measured by a simple voltage measurement and the Gibbs energy change of the corresponding process is calculated. However, since there is no net current measured or applied for an open circuit measurement, the value of electrical work done is not explicit for an open circuit EMF measurement.

The diffusion and ionic conductivity information of YSZ is well established in the literature. However, some information such as the maximum available work done during the experiment, solid vapor equilibrium and ohmic or rectifying contact potential drop are specific to every individual experiment.

Galvanic Cells and Thermodynamics of Solid Electrolytes

The galvanic cell is a device in which chemical energy is converted to electrical energy. Solid-state galvanic experiments are mainly composed of reference and test electrodes separated by a solid electrolyte. Both electrolytes usually contain powdered chemicals or pressed pellets of the mixtures of solid compounds and elements. During the experiment, the electrodes may experience phase transformations such as liquid-solid or solid-solid. When two solid electrodes containing chemical compounds with different electrical potentials are interconnected, some electrical work will be done due to the flow of charge through the solid electrolyte.

The measurement of open circuit voltage data over a range of temperature yields the calculation of some fundamental thermodynamic functions based on the electrochemical equilibrium assumption and Gibbs energy change of chemical reactions. Equilibrium condition definitions for an electrochemical system are different from those for chemical equilibrium due to the involvement of electrical charge and field. Due to the nature of solid electrolyte, the relationship between electrochemical potential and the Gibbs energy change becomes significant and requires the definition of new conditions for electrochemical equilibrium, which is specific to galvanic cell experiments.

Electrochemical Equilibrium

At equilibrium, according to the first law of thermodynamics the state functions of internal energy U and Gibbs energy G are given by the following relations:

$$dU = TdS - PdV + \delta W' \tag{2.2}$$

$$dG = -SdT + VdP + \delta W' \tag{2.3}$$

For a constant temperature and pressure process in an isolated system $dT=0$ and $dP=0$. The Gibbs energy change of the process is given by

$$dG = dW'_{T,P} \tag{2.4}$$

$dW'_{T,P}$ is the total maximum reversible work done on the system other than mechanical work. This work may appear as a result of phase transformation, chemical reaction or charge transfer during the process. It appears as a result of O^{2-} ion transfer through the YSZ electrolyte in particular. The amount of work done to transfer a unit charge from one point to another in an electric circuit is equal to the difference between potential energies of the two points. Electrostatic(or electric) potential is expressed in units of joules per coulomb, or volts. Since the potential of a point is the work done in

carrying a unit positive charge from infinity to that point, it is a scalar quantity. This potential difference can be represented by the work functions since it is a material specific property for both metals and semiconductors. The work function is defined as the difference between the Fermi energy of semiconductor and the energy of a free electron outside the metal or semiconductor, which is characterized as the vacuum level or zero energy state. The Fermi energy is given by the symbol E_F and is also called chemical potential of conduction electrons.

When two conducting materials with different work functions are brought in to contact, electrons pass over from the metal with the lower work function to that with the higher one until their Fermi levels are equal. There appears a depletion region due to the charge transfer between surface regions of the contacting materials. The electric double layer formation leads to a discontinuous jump of the electrostatic potential V at the junction. This potential drop is resulted by the difference between the chemical potentials(E_F)

$$e^-V_A - e^-V_B = \Phi_A - \Phi_B = (E_\infty - E_{FA})_{Flat\ band} - (E_\infty - E_{FB})_{Flat\ band} \tag{2.5}$$

where e^- denotes the charge of an electron and Φ refers to the work function, which is linked to the chemical potential of conduction electrons. V_A and V_B are the electrostatic potentials at points A and B. For n number of charges in one mole of an ion, the charge can be represented by

$$Q = -nF \tag{2.6}$$

where F is the Faraday's number, 96,485 coulomb/mol, and n is the valence of the ionic charge. The Gibbs energy change related to this process can be represented as

$$\Delta G = \Delta W'_{T,P} = -nF(V_A - V_B) \tag{2.7}$$

For the galvanic cell EMF experiments, points A and B usually represent the two ends of the solid electrolyte where the O^{2-} ions are transferred. Since only chemical potential difference of the oxygen ions induces the charge transfer, there is not an actual depletion layer through YSZ and the chemical potential of O^{2-} is determined by individual chemical reactions taking place in individual compartments. There is no net current through the system due to open circuit situation. Thus, the ionic transfer of O^{2-} is balanced by the transfer of electrons in the opposite direction.

The Nernst equation, which is obtained above for the general case, is derived by the assumption of an equilibrium process, which is Fermi level equilibrium. However, there is no chemical equilibrium since chemical reactions take place in different cells separately. At this point, the definition of electrochemical potential term is helpful to explain the conditions for equilibrium.

The general representation for electrochemical potential is given by

$$\eta_i = \left(\frac{\partial G}{\partial n} \right)_{T,P,n_j \neq n_i} \tag{2.8}$$

and the general condition for equilibrium can be represented as

$$\Delta G = \sum_i \nu_i \eta_i = 0 \tag{2.9}$$

The electrochemical potential is denoted by the symbol η_i and it is a function of both chemical and electrical potentials,

$$\eta_i = \mu_i + n_i F (V_i - V_\infty) \tag{2.10}$$

where V_∞ is the vacuum level potential, which is by definition assumed to be zero as a reference state. Electrical potential term disappears in the case of no applied field; then the standard chemical balance condition is obtained.

Lets assume an isolated electrochemical system with the following half-cell reactions:

$3e^{-1} + ½ In_2O_3(s) + 2Cu_2Se(s) \leftrightarrow CuInSe_2(s) + 3Cu(s) + 3/2 O^{2-}$ Test

$\underline{In(l) + 3/2 O^{2-} \leftrightarrow ½ In_2O_3(s) + 3e^-}$ Reference

$2Cu_2Se(s) + In(l) \leftrightarrow CuInSe_2(s) + 3Cu(s)$ Overall
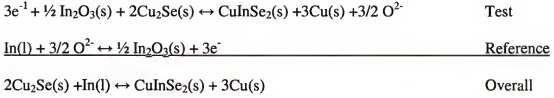
In this system, the reference and test electrodes are separated by a solid ionic electrolyte (Figure 1.1) and isolation constraints are enforced. As soon as the system is isolated, an ionic charge transfer through the electrolyte will take place. A constant potential will be achieved after the system reaches electrochemical equilibrium. This equilibrium condition will be interrelated to the chemical potential of O^{2-} ions and half-cell reactions. However, a general relationship can still be derived from the overall reaction.

The galvanic cell can be evaluated as a multi-component multiphase and reacting system. Considering the two electrodes as two separate phases can represent the total entropy change for such a system,,

$$dS_{sys} = dS_\alpha + dS_\beta \tag{2.11}$$

where α and β represents the two distinctive electrodes separated by the solid electrolyte. The internal energy function from the combined statements of the first and second laws can be given as

$$dU^\alpha = T^\alpha dS^\alpha - P^\alpha dV^\alpha + \eta^\alpha dn^\alpha \tag{2.12}$$

where $\eta = \left(\dfrac{\partial U}{\partial n} \right)_{S,V}$

To investigate the conditions for equilibrium for such a system the change of entropy function must be written individually for each phase.

Cell I α-phase In, In_2O_3	Cell II β-phase In_2O_3, Cu_2Se, Cu, $CuIn_2Se_3$

$$dS_{sys}=d(S^\alpha+S^\beta)=dS^\alpha+dS^\beta \tag{2.13}$$

$$dS^\alpha = \frac{1}{T^\alpha}dU^\alpha + \frac{P^\alpha}{T^\alpha}dV^\alpha - \sum_{k=1}^{n}\frac{\eta_k^\alpha}{T^\alpha} \tag{2.14}$$

$$dS^\beta = \frac{1}{T^\beta}dU^\beta + \frac{P^\beta}{T^\beta}dV^\beta - \sum_{k=1}^{n}\frac{\eta_k^\beta}{T^\beta} \tag{2.15}$$

Isolation constraints enforce energy conservation $dU^\alpha = -dU^\beta$ ($dU_{sys}=0$) and the total constant volume assumption $dV^\alpha = -dV^\beta$ ($dV_{sys}=0$). The total mass is also kept constant $dm_k=0$ where m is the total number of grams of elements. The total mole numbers are not constant ($dn_k \neq 0$) because of chemical reactions; however, the relation between dm_k and dn_k can be obtained from the stoichiometry. In this example:

β-phase reactions (test electrode):

$$3e^{-1} + \frac{1}{2} \ In_2O_3(s)+2Cu_2Se(s) = CuInSe_2 \ (s) +3Cu(s) +3/2 \ O^{2-} \qquad \textbf{Test}$$

$m_O=3 \times n_{In_2O_3}+ n_{O2-}$,$dm_O=0$, $dn_{O2-}=-3 \times dn_{In_2O_3}$

$m_{Cu}=2 \times n_{Cu_2Se}+ n_{CuInSe_2}+ n_{Cu}$,$dm_{Cu}=0$, $dn_{CuInSe_2} = -2dn_{Cu_2Se}- dn_{Cu}$

$m_{In}=2 \times n_{In_2O_3}+ n_{CuInSe_2}$,$dm_{In}=0$, $dn_{CuInSe_2} = -2 \times dn_{In_2O_3}$

$m_{Se}=n_{Cu_2Se}+ 2 \times n_{CuInSe_2}$,$dm_{Se}=0$, $dn_{CuInSe_2}=-1/2dn_{Cu_2Se}$

$0=n^\beta_{e^-} + 2 \times n_{O2-}$,$dn^\beta_{e^-} = -2 \times dn_{O2-}$

The latter condition is a result of the assumption that there is no net current passing through the system. The total charge in the system must be kept constant.

Similarly for the α-phase reactions (reference electrode):

$In(l) + 3/2\ O^{2-} = \frac{1}{2} In_2O_3 + 3e^{-1}$ **Reference**

$m_{In} = n_{In} + 2 \times n_{In_2O_3}$ $, dm_{In} = 0$ $, dn_{In} = -2 \times dn_{In_2O_3}$

$m_O = n_{O^{2-}} + 3 \times n_{In_2O_3}$ $, dm_O = 0$ $, dn_{O^{2-}} = -3 \times dn_{In_2O_3}$

$0 = n^{\alpha}_{e^-} + 2 \times n_{O^{2-}}$ $, dn^{\alpha}_{e^-} = -2 \times dn_{O^{2-}}$

By applying boundary conditions and variable constraints, the overall entropy function becomes

$$dS_{sys} = dS^{\alpha} + dS^{\beta} = \frac{1}{T^{\alpha}} dU^{\alpha} + \frac{P^{\alpha}}{T^{\alpha}} dV^{\alpha} - \left[-2\eta^{\alpha}_{In} - 3\eta^{\alpha}_{O^{2-}} + \eta^{\alpha}_{In_2O_3} - 6\eta^{\alpha}_{e} \right] dn^{\alpha}_{In_2O_3} +$$
$$\frac{1}{T^{\beta}} dU^{\beta} + \frac{P^{\beta}}{T^{\beta}} dV^{\beta} - \left[-6\eta^{\beta}_{e} + \eta^{\beta}_{In_2O_3} + 4\eta^{\beta}_{Cu_2Se} - 2\eta^{\beta}_{CuInSe_2} + 3\eta^{\beta}_{O^{2-}} + 4\eta^{\beta}_{Cu} \right] dn^{\beta}_{In_2O_3}$$

The new isolation constraints can be summarized as

$$dU^{\alpha} = -dU^{\beta} \tag{2.16}$$

$$dV^{\alpha} = -dV^{\beta} \tag{2.17}$$

$$dn^{\alpha}_{In_2O_3} = -dn^{\beta}_{In_2O_3} \tag{2.18}$$

By substituting new conditions and rearranging for common terms,

$$dS_{sys,isolated} = \left(\frac{1}{T^{\alpha}} - \frac{1}{T^{\beta}} \right) dU^{\alpha} + \left(\frac{P^{\alpha}}{T^{\alpha}} - \frac{P^{\beta}}{T^{\beta}} \right) dV^{\alpha} + \tag{2.19}$$
$$\left\{ 6 \left[\eta^{\alpha}_{e} - \eta^{\beta}_{e} \right] - \left(2\eta^{\beta}_{CuInSe_2} + 6\eta^{\beta}_{Cu} - 2\eta^{\beta}_{In} - 4\eta^{\beta}_{Cu_2Se} \right) \right\} dn^{\alpha}_{In_2O_3}$$

The condition for an extremum or equilibrium is obtained by setting each bracket to zero. The first two brackets lead to a very common representation of equilibrium, which is known as thermal (constant T) and mechanical (constant P) equilibrium. The 3rd

bracket, however, brings a new information, which is the relation between the Gibbs energy change of the reaction and the electrochemical potential difference between two ends of the electrodes,

$$\left[\eta_e^\beta - \eta_e^\alpha \right] = \left[nF(V_{e^-}^\beta - V_{e^-}^\infty) \right] - \left[nF(V_{e^-}^\alpha - V_{e^-}^\infty) \right]$$
$$nF(V_{e^-}^\beta - V_{e^-}^\alpha) = \left(\mu_{CuInSe_2}^\beta + 3\mu_{Cu}^\beta - \mu_{In}^\alpha - 2\mu_{Cu_2Se}^\beta \right) \tag{2.20}$$

This expression is the basis for the EMF experiments. Only the potential difference between β and α is needed to obtain the Gibbs energy change of the reaction. However, the measurements are sensitive to any potential drops between the contact points. Potentiostat is connected to the two ends of wire leads and these wire leads are also connected to cell electrodes. Between the junction points, potential drop may be observed. Even small drops may become very important for the dependability of EMF experiments since regular activity measurements are usually in the range of millivolt levels. The connection type is an important factor in determining the influence of potential drop at contacts. It is usually preferred to have ohmic contacts because of the small potential drop at the metal semiconductor junction. However junction potential drop is not the only factor for design considerations ; the oxidation of materials, melting temperature and conductivity of the selected material are also important. There is additional potential drop when rectifying contact is established and it becomes drastic when current is applied to the cell. Figure 2.1 shows a schematic of a potential drop throughout an EMF experiment.

Figure 2.1 Schematic of an EMF system (closed system, T, P constant, open circuit condition)

Experimental Considerations

Metal Semiconductor Contact

The metal–semiconductor contact plays a very important role in the stability of EMF measurements. There are basically two types of metal semiconductor contacts. The rectifying contact, referred as the Schottky diode, is usually not preferred for EMF measurements due to its I-V and potential barrier characteristics. On the other hand, non-rectifying or ohmic-like contact is favored due to the low potential barrier for charge carriers. A Schottky barrier is formed when a metal is deposited or contacted on a p-type semiconductor such that $\Phi_M < \Phi_S$ and on a n-type semiconductor with $\Phi_M > \Phi_S$. The other possible combinations are summarized in Table 2.1.

Table 2.1 Electrical characteristics of metal-semiconductor contacts

Work Function Comparison	p-type semiconductor	n-type semiconductor
$\Phi_M < \Phi_S$	Rectifying	Ohmic
$\Phi_M > \Phi_S$	Ohmic	Rectifying

The metal work function Φ_M is an invariant property for metals and defined as the energy difference between vacuum level and the Fermi energy. However, for semiconductors Φ_S is composed of two distinct parts,

$$\Phi_S = \chi + (E_c - E_f) \tag{2.21}$$

E_c-E_f term is constant only for flat band conditions but χ is an invariant fundamental property of the semiconductor. χ is defined as the electron affinity which remains unaffected by the contacting process and is given by the following relation:

$\chi = E_\infty - E_c$

where E_∞ is the vacuum energy state, which is taken as zero.

Suppose a metal with $\Phi_M > \Phi_S$ and a n-type semiconductor are brought together. Assuming no interdiffusion, no impurities and no oxide layers on the surface, the contact formed can be defined as ideal. Equilibrium conditions for semiconductors require that any material or materials that are interconnected must have the same Fermi level. As a result of this condition electrons start to transfer from semiconductor to the metal. The electrical double layer or a depletion layer is created by the diffusion of electrons from semiconductor to the metal. The region where the depletion of electrons occur will be charged positively relative to the bulk material and there will be a growing barrier against the electron transfer due to the electric field at the depletion layer. When diffusion rate

and the depletion layer electric field are balanced, E_f becomes the same throughout the structure. The corresponding band diagram is illustrated in Fig 2.2.
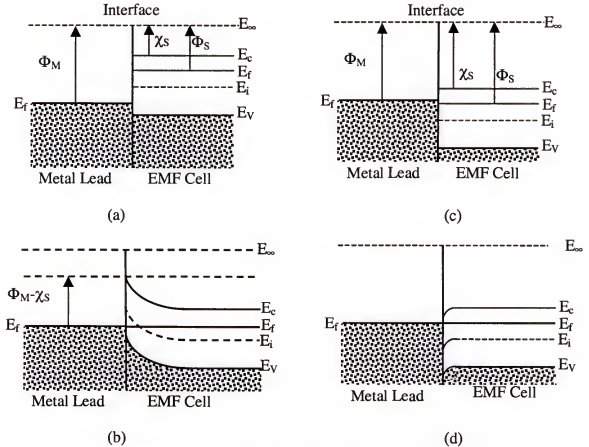
Figure 2.2 Energy band diagram for metal and n-type semiconductor. (a) instant contact, no equilibrium for $\Phi_M > \Phi_S$, (b) after equilibrium band bending and depletion layer formation, (c) instant contact for $\Phi_M < \Phi_S$, (d) no potential barrier to current flow after equilibrium for $\Phi_M < \Phi_S$.

In Figure 2.2 (b) there is a potential barrier for electrons and in Figure 2.2 (d) there is no potential barrier for electrons. This potential barrier or built in voltage created by rectifying contact becomes more important when electric voltage needs to be applied. In this case, no Fermi level equilibrium can be observed. In Figure 2.2 (b), applying $V_a > 0$ raises the Fermi level of the semiconductor and reduces the barrier seen by the electrons in the semiconductor and leads a net forward current. On the other hand,

applying Va<0 increases the potential barrier and blocks the flow of electrons. This reverse bias current will be relatively small. When doing titration (EMF) experiments, it is very important to know the characteristics of metal contacts since applied voltage can not be converted to a current in the system in the case of rectifying contact. On the contrary, in the case of Figure 2.2 (d) there is no potential barrier to the electrons and an ohmic contact behavior is observed, which has a negligible contact resistance relative to bulk or series resistance of the semiconductor. Similar principles also apply for metal p-type contacts.

YSZ Solid Electrolyte

Zirconium dioxide (ZrO_2) is a refractory material with high chemical and corrosion resistance to temperatures well above 2000 °C. It is electrically conductive by an ionic mechanism above 600 °C and has many uses in oxygen sensors and as the heater in some high temperature applications. Pure zirconia exists in three crystal phases at different temperatures. Above 2370°C the material is stable in the form of a cubic structure. Between 1170 and 2370 °C it has a tetragonal structure. At low temperatures (below 1170°C) the material transforms to the monoclinic. The phase transformation from tetragonal to monoclinic occurs with a rapid 3 to 5 percent volume expansion, which causes extensive cracking in the material during cooling processes. Zirconia is usually stabilized by substituting host Zr^{4+} ions with di- or trivalent cations to slow down or eliminate these crystal structure changes. Several oxides that dissolve in the zirconia crystal structure are used. Commonly used effective additives are MgO, CaO, and Y_2O_3. When sufficient amounts are added, cubic solid solutions of fluorite type structure are formed and this structure can be maintained to room temperature.

Stabilized zirconia adopts the Fluorite structure CaF_2, which is the structure of pure zirconia at high temperature. The lattice is face-centered cubic (fcc) and the space group is *Fm3m*. The unit cell embodies effectively 4 zirconium atoms and 8 oxygen atoms. Zirconium cations occupy the positions (0,0,0) of the lattice and oxygen anions occupy the positions (1/4,1/4,1/4) and (1/4,3/4,1/4). Each Zr cation is surrounded by eight oxygen ions, which are contained in tetrahedrons formed by zirconium ions. The oxygen ions form a cubic sublattice of half the lattice parameter of the fcc cell.

In general, the conductivity of solid electrolytes is several orders of magnitude higher than normal ionic compounds and fluorite crystal structure appears to be particularly suitable for high anionic conductivity. Due to its high ionic conductivity and transport and electrical properties, stabilized zirconia has been studied for many years. Yittria (Y_2O_3) incorporation into zirconia (ZrO_2) structure enhances oxide-ion conductivity of the material by creating oxide-ion vacancies and by further stabilizing the cubic fluorite crystal structure. Structurally, introduction of Y into Zr lattice sites requires the formation of either anion vacancies or cation interstitials. In fact, individual experiments confirm that anion vacancy formation is dominant and mostly responsible for the high ionic conductivity of YSZ. Typical conductivity ranges of YSZ or other solid electrolytes approach to the ionic conductivity ranges of molten salts ($\sigma=10^{-2}$ ohm^{-1}cm^{-1}) where free anion and cation movement is possible.

Yittria stabilized zirconia (YSZ) is a popular solid electrolyte for many applications such as galvanic and fuel cells, oxygen detectors and oxygen separators. It has been established in the literature that YSZ oxygen self-diffusion and ionic conductivity take place by a vacancy replacement mechanism. However, the mobility and

the relation between the concentration of free vacancies and mass transport are not well understood. In addition, YSZ defect reaction mechanisms can be quite complex since cubic zirconia is stabilized by the addition of large concentrations (8.5 mol%) of Yittria. It has been observed that the maximum electrical conductivity occurs around the compositions of 8 to 10 mole% Y_2O_3, which lie close to the monoclinic–cubic solid solution phase boundary.

Oxygen partial pressures are strongly related to the electron hole and defect concentrations. For 8.5 % mole Y_2O_3 doped zirconia, oxygen vacancy domination can be represented by anti-Frenkel disorder mechanism and external equilibrium reaction can be written for the solid gas adjacent interface,

$$O_O^x + 2h \leftrightarrow [V_O^{..}] + \tfrac{1}{2}O_2 \quad \text{or,} \tag{2.22}$$

The equilibrium constant is given by

$$K_X = \left([V_O^{..}] \cdot P_{O_2}^{1/2}\right)/p^2 \tag{2.23}$$

For every one mole of Y_2O_3 doped in ZrO_2, 2 Y atoms replace 2 Zr atoms. Yittria can be considered a shallow acceptor and completely ionized at the temperature of interest. This leads to a fixed acceptor concentration for $[Y_{Zr}']$ of $1.02374*10^{23}$ particle/cm³.

The formation of anti-Frenkel defects leads to following relation:

$$K_d = [V_O^{..}] [O_i''] \tag{2.24}$$

The formation of an electron-hole pair is given by the relationship:

$$K_i = [e'] [p^{.}] \tag{2.25}$$

The electroneutrality condition can also be applied as

$$2[O_i''] + [e'] + [Y_{Zr}'] = [p^{\cdot}] + 2[V_O^{\cdot\cdot}]$$ (2.26)

Now all the defect concentrations in the solid structure and their dependencies with stoichiometry of the host material and the fixed solute concentration can be evaluated. If these equations are expressed as a function of one independent concentration and appropriate boundary conditions are applied, the defect equilibrium diagram can be completed as given in Figure 2.3.
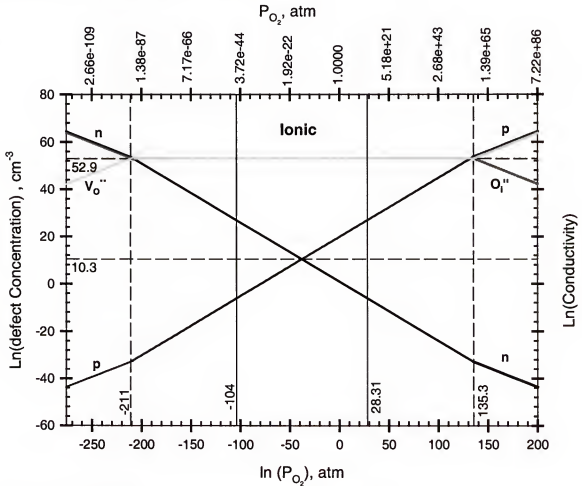

Figure 2.3 Defect concentration isotherm for YSZ at 873K.

Figure 2.3 illustrates the defect equilibrium diagram for 8.5 % mole Y_2O_3 stabilized zirconia at 873 K. The lower oxygen equilibrium pressure limit for ionic conductivity is 6.81356E-46 and the higher P_{O_2} pressure limit is 1.97186E+12. The external equilibrium constant is calculated as K_x=6.5414E+23. The electronic equilibrium constant K_i is calculated to be 1.06E+09. Zirconia was assumed to be non-degenerate at given temperature range with a band gap of 5.4 eV and the Fermi level of 1.6 eV (Ev+3kT<Ef<Ec-3kT). The reason for narrower ionic conductivity range can be explained by the fact that the higher mobility values for electrons and holes in the ionic range increase the conductivity of electronic charge carriers.

Test and Reference Electrode Materials

The EMF cells used in these studies maintained oxygen equilibrium pressures that lie within the range of electrolytic domain at working temperatures of solid electrolyte (1 atm and 600 to 800 °C). Operating outside of the electrolytic domain results in non-equilibrium conditions and unstable measurements. The EMF cell generally uses a reference electrode and working electrode. The purpose of the reference electrode is to fix the activity of the oxygen by using metal/metal oxide chemical system in one electrode and to measure working electrode activities accordingly. One of the most important factors in determining the reference electrode is the chemical stabilities of components at given temperature and pressure conditions. Cu_2O and Ga_2O_3 are used as reference electrode materials throughout in EMF experiments in this research. The stability of electrode materials with respect to solid electrolyte is compared in Figure 2.4.
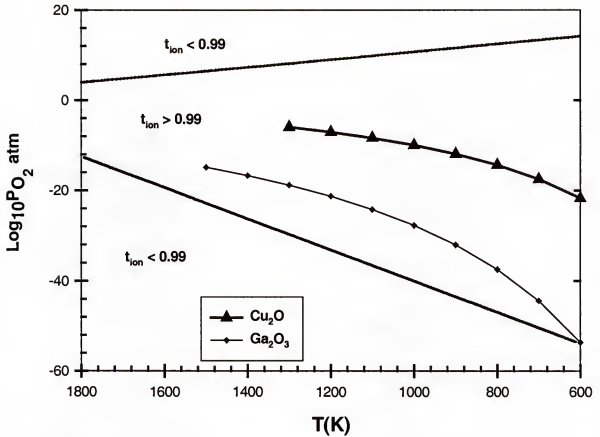
Figure 2.4 Electrolytic domain of YSZ for Cu_2O and Ga_2O_3 equilibrium pressures.

Figure 2.4 shows the electrolytic domain of YSZ and the behavior of Cu_2O and Ga_2O_3 in the ionic conductivity region. In the working temperature and oxygen partial pressure range of YSZ electrolyte, both oxides maintain their stabilities although a general exponential dependency is evident. The equilibrium partial pressure of Ga_2O_3 is similar to the value of YSZ ionic-electronic conductivity transition line at 600 K. Hence, Ga_2O_3 cannot be used effectively below that temperature. For experiments that include pure solid and oxide phases of both copper and gallium elements, the relative stabilities of these oxides also become a factor for proper electrode material selection.
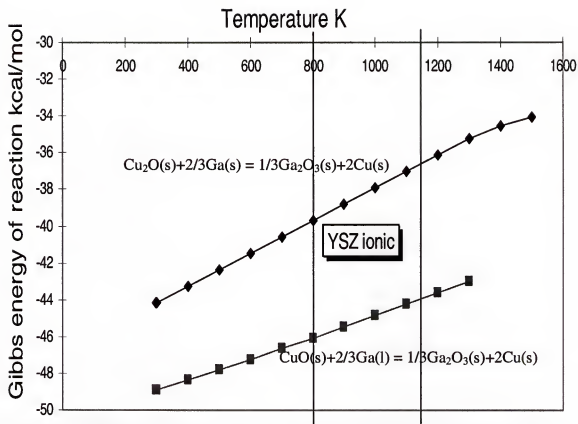
Figure 2.5 Gibbs energy of formation of copper and gallium oxides in the conductivity range of YSZ solid electrolyte.

Figure 2.5 compares the stabilities of copper and gallium oxide mixtures with temperature. CuO and Cu_2O are given as the two stable solid oxide formations of copper in the working temperatures of experiments. Gallium has only one stable oxide form, which is Ga_2O_3 in the solid phase. Gibbs energies of the following chemical reactions were calculated for stability analysis:

$Cu_2O(s) + 2/3Ga(l) = 1/3Ga_2O_3(s) + 2Cu(s)$ $\quad\quad \Delta G_R = 0.009T(K) - 46.873$ kcal/mol

(298.15-1300K).

$CuO(s) + 2/3Ga(l) = 1/3Ga_2O_3(s) + Cu(s)$ $\quad\quad \Delta G_R = 0.0059T(K) - 50.745$ kcal/mol

(300-1300K).
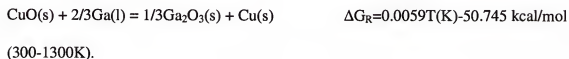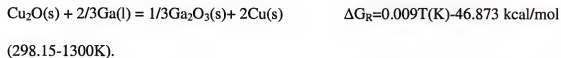
The reaction between CuO and Ga produce more negative Gibbs energy change since Cu_2O is more stable than CuO. Both reactions involving Ga_2O_3 formation produce Gibbs energy values lower than –20 kcal/mol, which verifies that Ga_2O_3 is the most stable phase in given environment. Hence, gallium and gallium oxide was selected as the reference electrode material when gallium and copper were both present in working electrode.

All the EMF experiments are subject to experimental errors. When current is passed through the electrochemical cell, electrode and electrolyte polarization is a problem. For large values of applied current, electrode and extension wire resistances between the cell and potentiostat can also be significant. One of the most important problems for open circuit measurement is to maintain gas-solid equilibrium under inert gas flow. This difficulty is encountered especially when one of the components has a very high equilibrium pressure. When selecting electrode materials, high electrical conductivity materials are preferred, however, the chemical stability and chemical inertness are the limiting factors. For EMF experiments there is not many choices for electrode materials since the reference electrode activity must be chosen from the test electrode materials. Another problem is to maintain constant inert gas flow rate and to avoid gas phase reactions between two separate electrodes. Inert gas flow not only minimizes materials from evaporating but also prevents them establishing an electrical contact through gas phase reactions. Experiments have shown that the use of inert gas flow experiments is not desirable for systems that include high vapor pressure components. For high vapor pressure component systems pressure tight systems are

suggested to maintain individual equilibrium and isolation constraints for reference and test electrodes.

Summary

Electrochemical measurements provide effective opportunities for measuring critical missing thermodynamic properties from related chemical reactions such as Gibbs energy and enthalpy of transformation data. EMF experiments allow measuring Gibbs energy of formation of intermediate compounds that are not usually measured by conventional methods. The solid electrolyte used is the most important part of the experimental setup due to its influence on the behavior of electrochemical reactions and equilibrium. YSZ functions properly only under certain conditions of temperature and partial oxygen pressure. This limits the selection of materials that can be used in the galvanic cell arrangement. EMF experiments involve electrochemical equilibrium. Electrochemical potential is derived to explain reversible work done on the system for an open cell system. Electrical contact types for EMF experiments play an important role in reliability of the measured data. Junction potential drops are important factors to determine the characteristics of ohmic contact. Solid electrolyte conductivity range and defect equilibrium diagrams were calculated by applying an anti-Frenkel defect formation mechanism. Stabilities of reference electrode materials were analyzed and compared with the working temperatures of the YSZ electrolyte. The derived relationships for the electrochemical equilibrium establish the basis of electrochemical calculations in the following chapters.

OPTIMIZATION AND ASSESSMENT METHODS FOR THERMOCHEMICAL AND
PHASE DIAGRAM DATA

Introduction

A phase diagram is one of the most essential tools for scientists and engineers in many fields. The equilibrium state of a system with respect to pressure and temperature is summarized by simple graphical representation. In general, the stability of materials, meta-stable compound information and solution phase behavior are obtained by phase diagram assessment. The synthesis and characterization of new materials, improvement of material quality, process design and many other engineering applications require accurate phase diagram information. The utilization of efficient and logical phase diagram calculation procedures based on thermodynamic principles and the prediction capability of undetermined phase regions are of practical importance. Because multi-component and multiphase equilibria require exhausting calculation steps, computer calculation procedures and standard models for complex systems are developed. In addition, the developments in computer modeling capabilities along with speed and storage improvements in computer technology stimulates the interest on advanced theories for better physical representation and understanding of complex disorder behavior. However, the utilization of complicated models has not proven to be successful for all systems. Because the derivation of some models are based on only mathematical theories, the physical and chemical aspects of solution and disordered phase behavior are not always be well represented. To assess phase diagrams carefully, phase models must

be standardized and well coordinated with the computer calculation procedures. Mathematical models used in optimization procedures usually consist of polynomials whose parameters are selectively optimized with temperature and composition. The phase diagram is the result of calculations that combine experimental data with thermodynamic principles. However, the current optimization methods are mainly based on trial and error methods of fitting the model parameters to the set of experimental data or to the predicted constraints, which may not be estimated correctly. The current curve fitting procedures usually bring on calculation uncertainties since the outcome of a phase diagram may be varying according to the starting boundary conditions. The type of applied mathematical model or the error limits of calculations may also vary the overall outcome of the assessment. Most of the models can be fitted within given precise approximation limits because the optimization technique is constructed to be self-consistent mathematically. However, thermodynamic excess properties may not be reliable when extrapolation of thermodynamic parameters from subsystems to higher component systems is required. As a result, the number of model parameters for solution models must be kept as small as possible to prevent unnecessary complexity in mathematical calculations.

Theory of CALPHAD

The theory of relationship between thermodynamics and phase equilibria was established a long time ago. However, the development of the phase diagram calculation techniques has become practical mostly due to rapid developments in computational technology. Josiah Willard Gibbs first formulated the "Gibbs Phase Rule" in 1896. The first mathematical foundation between the Gibbs energy concepts and phase equilibria by J. J. Van Laar followed in 1908. However, it was not until before 1970 that the CALculation of PHAse Diagrams (CALPHAD) [4] technique was first specified by

Kaufman and Bernstein [5]. Since then, the CALPHAD procedure has improved comprehensively. It incorporates the general characteristics of the calculation of phase diagrams with computer programs.

Many computer software packages have been developed for optimization and calculations [6]. The most frequently used programs are Thermo-Calc, Lukas, ChemSage, and MTDATA. However, the optimization procedures and user interfaces are not standardized. Calculations involve systematic trial and error methodology to adjust the model parameters. The overall system is optimized by assigning appropriate error limits to measured phase diagram and thermodynamic data. Several databases were also constructed to associate different sources of experimental and thermodynamic assessments. A consistent and more systematic method that takes in to account different types of calculation methods is necessary since every individual calculation method, mathematical model or starting parameters results in different outcomes. This can be accomplished by formulating new extrapolation techniques and building the computer calculation routines on a more reasonable physical meaning. The utilization of simulation methods in optimization procedures will eventually be required.

Thermodynamic Basis of Phase Diagrams and Solution Modeling

Mathematical description of phase equilibrium is built on the energy minimum and the entropy maximum principle. By definition, the entropy function must attain an extremum value at equilibrium. Gibbs energy is another way of representing this phenomenon. The direction of spontaneity is indicated by the negative sign of Gibbs energy, which approaches a minimum at equilibrium. Other thermodynamic state functions, Helmholtz free energy and enthalpy function, are also associated with the

condition for spontaneity although they are derived for different constraints. The Gibbs energy function is defined in terms of state functions as

G=U+PV-TS=H-TS   (3.1)

dG=-SdT+VdP   (3.2)

The latter representation is most commonly used for phase equilibrium applications since phase diagrams are usually calculated for constant pressure systems and only entropy change with temperature is needed. The Entropy of condensed phases is usually obtained by simple heat capacity measurements in combination with the third law and phase transformation properties are also obtained experimentally. Phase equilibria are calculated directly from the Gibbs energy functions, which are assessed from experimental and calculated data.

Mathematical Strategy

The mathematical strategy of phase diagram calculations is based on obtaining the optimum parameters, which satisfy the conditions stressed by the energy minimum and the entropy maximum principle [7]. Entropy is continuous, differentiable and monotonically increasing function, which reaches its maximum value at equilibrium processes. The derivative of entropy function becomes zero at this extremum point. In general, the differential of a function $z=z(x,y,m,n......)$ with independent variables of $x,y,m,n...$ is given by the formula

$$dz = \left(\frac{\partial z}{\partial x}\right)dx + \left(\frac{\partial z}{\partial y}\right)dy + \left(\frac{\partial z}{\partial m}\right)dm\left(\frac{\partial z}{\partial n}\right)dn + ...$$ (3.3)

The z function has extreme points for the condition in which the right hand side of the Equation (3.3) effectively vanishes or all the partial derivative terms given in brackets converge to zero at once. For systems with a higher number of independent variables,

simultaneous solution of these set of coefficients may require the help of computer programs. Unconstrained maximum is described when all the variables of a function are independent of each other. Thermodynamically, the entropy function is derived for isolated systems and some variables can be interrelated. Thus, the Gibbs energy function has constrained extremes although it is monotonic in nature. It is usual in binary systems or solution phases that the Gibbs energy has an extremum for composition while it decreases monotonically with temperature. This situation is more explicit during common tangent construction procedure in free energy-composition diagrams.

Conditions for Thermodynamic Equilibrium

A general strategy for a one component system with two equilibrium phases requires an expression for the change of entropy for both phases. The total entropy change for such a system is given as

$$dS_{sys} = dS^{\alpha} + dS^{\beta} \tag{3.4}$$

where α and β represent distinct phases in a unary system. From the combined statements of the first and second laws,

$$dU^{\alpha} = T^{\alpha} dS^{\alpha} - P^{\alpha} dV^{\alpha} + \mu^{\alpha} dn^{\alpha} \tag{3.5}$$

where μ is called the chemical potential and related to the Gibbs free energy function as

$$\mu = \left(\frac{\partial G'}{\partial n} \right)_{T,P} = G \tag{3.6}$$

where G' is the extensive property representing the overall value of Gibbs energy function. By applying boundary conditions and variable constraints, overall entropy function becomes

$$dS_{sys,\ isolated} = dS^{\alpha} + dS^{\beta} \tag{3.7}$$

$$= \frac{1}{T} dU^{\alpha} + \frac{P^{\alpha}}{T^{\alpha}} dV^{\alpha} - \frac{\mu^{\alpha}}{T^{\alpha}} dn^{\alpha} + \frac{1}{T}(-dU^{\alpha}) + \frac{P^{\alpha}}{T^{\alpha}}(-dV^{\alpha}) - \frac{\mu^{\alpha}}{T^{\alpha}}(-dn^{\alpha}) \qquad (3.8)$$

The equation (3.6) leads to the well-known conditions for equilibrium [7] given as

$T^{\alpha}=T^{\beta}$, $P^{\alpha}=P^{\beta}$, $\mu^{\alpha}=\mu^{\beta}$ \hfill (3.9)

These conditions are proven to be valid for any equilibrium system and independent of whether the system is isolated or not in the process of reaching the equilibrium state.

Thermodynamic Models for Multi-component Systems

Various thermodynamic models have been developed for multi-component system equilibria. Individual phases are represented by Gibbs energy functions with pressure, temperature and composition dependencies. CALPHAD method implements several models to describe multi-component systems. The general form of the Gibbs energy of a phase is given by

$G=G(T,P,x,\beta)$ \hfill (3.10)

where T,P, and x represents the contributions of temperature, pressure and composition. β is the magnetic contribution to the Gibbs energy, which is applicable for paramagnetic materials [5]. The simplest form of this model, which is mostly applied to stoichiometric compounds, contains only temperature dependence and is usually expressed with a reference point.

$G-H^{SER} = a+bT+cTlnT+dT^{2}+e/T+fT^{3}+ \ldots\ldots$ \hfill (3.11)

where H^{SER} is the enthalpy of the substances in their standard element reference states at 298 K.

The change of Gibbs energy can be calculated freely when all the functions are defined for the same standard state. The definition that Gibbs energy of formation of all elements are zero in their standard states at 298 K makes that assumption practical.

In general, the Gibbs energy of solution phases can be represented as

$$G^{solution} = G^0 + G^{ideal\ mixing} + G^{excess} \tag{3.12}$$

The first term corresponds to the contribution of the Gibbs energy of pure components; the second term represents the ideal mixing and the last term is introduced for the non-ideal interactions during the mixing process. The G^{excess} function is usually an unknown function of both temperature and composition. The outcome of a phase diagram is directly related to the particular behavior of excess energy function.

Thermodynamic Models for Ordered Phases

The CALPHAD approach describes the Gibbs energy of a binary stoichiometric phase of A_xB_y as

$$G = x_A G^0_A + x_B G^0_B + \Delta G^f \tag{3.13}$$

where ΔG^f is the formation energy of the compound. Ideal mixing term is not included because stoichiometric phases are accepted as ordered phases and no mixing is applicable.

Thermodynamic Models for Disordered Phases

Disordered phases such as solutions and defect compounds with large homogeneity ranges are usually represented by the assistance of general random mixing formulation,

$$G^{mix} = x_A G^0_A + x_B G^0_B + RT[x_A ln(x_A) + x_B ln(x_B)] + G^{excess} \tag{3.14}$$

where K is the solution interaction variable, which is related to bonding energies between molecules. The excess term is often represented by the Redlich-Kister polynomial [8], which is given as

$$G^{excess} = x_A x_B \sum_{i=1}^{n} K_i (x_A - x_B)^i \qquad (3.15)$$

where K_i is a temperature dependent parameter, which can be represented as

$$K_i = a_i + b_i T + c_i T \ln T + \ldots\ldots \qquad (3.16)$$

where a_i, b_i, c_i .... are constants.

More complicated models such as the associated solution model, ionic and sublattice models are used frequently. However, all the other models can be derived from the general representation of Redlich-Kister formalism by changing the order and arrangement of parameters.

The simplest form of excess mixing energy equation is called the regular solution model, which includes only the zeroth term of the Redlich-Kister polynomial.

$$G^{excess} = K_0 x_1 x_2 \qquad (3.17)$$

K_0 is related to the solution behavior in view of the positive and negative attractions between molecules. Positive values of K_0 indicate the dominance of repulsive forces and negative values mean attractive interactions between the molecules. In other words, a continuous solution is formed due to higher attractive forces between two components when K_0 is negative. When highly repulsive forces prevent molecules from mixing randomly, the excess term starts to overcome ideal mixing term. Consequently the solution lowers its Gibbs energy by forming a two-phase structure between the two minimums of the mixing function [7]. A general procedure of the CALPHAD approach

for the assessment of thermochemical and phase diagram data is given in Figure 3.1. The

similar calculation flowchart of the data assessment procedure is also given in Figure 3.2.
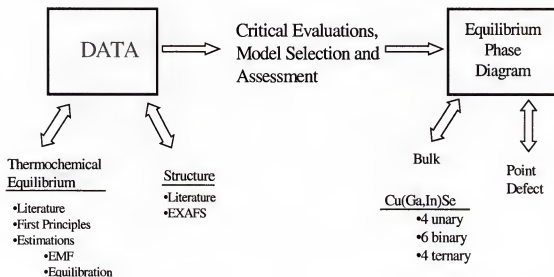

Figure 3.1 Schematic of the CALPHAD approach for thermodynamic phase diagram assessment.
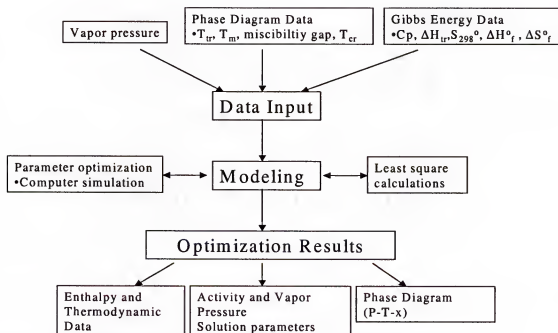

Figure 3.2 A general flowchart of the calculation procedure for phase diagram calculations.

THERMODYNAMIC DEFECT EQUILIBRIUM FOR CUPROUS SELENIDE AND
DETERMINATION OF THE HOMOGENEITY RANGE BY COULOMETRIC
TITRATION

Introduction

Consistent phase diagram and thermochemistry information for the Cu-Se system

is essential to better understand and better engineer thin film deposition processes for CIS

and CIGS based solar cells. Various experimental phase diagram data based on DTA, X-

Ray diffraction, microscopy, micro-hardness and electrical conductivity techniques have

been published for the Cu-Se system [11]-[18]. Those reported data have been reviewed

and assessed [1],[19] a few times; however, a full description of the system including

defect equilibria and phase boundary information for the β-Cu$_{2-x}$Se solid solution is not

available. β-Cu$_{2-x}$Se and its low temperature modification of α-Cu$_{2-x}$Se are two important

precursors during the synthesis of CuInSe$_2$. The other confirmed stable phases, CuSe,

Cu$_3$Se$_2$ and CuSe$_2$, are characterized as line compounds. Although the β-Cu$_{2-x}$Se is the

most stable and studied phase, the relationship between metal deficient semiconductor

properties and defect formation mechanisms are not well studied. As a result, the defect

structure of CuInSe$_2$ phase cannot be well defined. The understanding of defect structure

will be beneficial for future solar cell applications that will presumably require the

monitoring of defect properties during growth processes.

In this study, the equilibrium solid-state defect chemistry of Cu$_2$Se is explored.

The homogeneity range of β-Cu$_{2-x}$Se is measured and the thermodynamic functions for

defect species are estimated. The homogeneity range of β-$Cu_{2-x}Se$ was measured by coulometric titration in a solid-state galvanic cell. The Cu mole fraction change between the selenium-rich and the copper-rich boundaries was measured as Δx=0.012 at 900K. A defect model was developed based on vacancy formation on the Cu sublattice by associating the gas phase equilibrium with defect formation reactions. Temperature dependent defect equilibrium constants were estimated and a defect equilibrium diagram was calculated at 298K. Defect formation enthalpies were calculated with the assistance of partial free energy relations. Vibrational entropy changes for all defect reactions were found to be dependent on both temperature and defect concentrations.

Literature Review

The binary compound $Cu_{2-x}Se$ is a p-type semiconductor with carrier concentration dependency on x. The band gap is also reported to be variable between 1.1 and 1.7 eV [20], [21]. The semiconducting properties of $Cu_{2-x}Se$ are related to the point defect structure and directly attributed to the vacancies on the Cu sites. The electronic transport properties of this compound are characterized by positive signs of thermal EMF and the Hall constant and by a negative temperature coefficient of electrical resistivity [22],[23]. The di-chalcogenide, $CuSe_2$ with a pyrite type structure, is a superconductor with a critical temperature between 2.30 and 2.43K [24]. All the compounds in Cu-Se system except Cu_2Se, are stoichiometric in composition with negligible homogeneity range.

The homogeneity range of β-$Cu_{2-x}Se$ at room temperature is reviewed by Chakrabarti and Laughlin [19]. Different experimental studies, including DTA, X-Ray diffraction [12],[15],[25]-[28] and electrical conductivity [16] and have been used to

study the homogeneity range and the reported range is taken to be approximately between 35.4 to 36.0 at.% Se, corresponding to $0.18 \leq x$ in $Cu_{2-x}Se \leq 0.22$. The homogeneity range increases further at higher temperatures. The width of the phase field between 348 and 773K was determined from the break of the lattice parameter values [13],[18] Lorenz and Wagner [29] observed an extension of the $Cu_{2-x}Se$ phase field to Cu/Se ratio less than 1.86 (>35 at. Se) at 673 K by coulometric titration. Further, they estimated that the composition of the copper-rich boundary for β-$Cu_{2-x}Se$ at 673 K is $Cu_{1.9975}Se$ by interpreting their experimental results using classical statistics.

The homogeneity range of fcc β-$Cu_{2-x}Se$ was reported by Singh and Bhan [30] and Stevels and Jellinek [25] as $0.15 \leq x$ in $Cu_{2-x}Se \leq 0.2$ at room temperature. Several researchers suggested the existence of the two-phase region, α-$Cu_{2-x}Se$ and β-$Cu_{2-x}Se$, below 300K; however, the higher temperature homogeneity limits for β-$Cu_{2-x}Se$ are not well studied. Frangis *et al.* [31] reported the α to β-$Cu_{2-x}Se$ transition temperature as 400 ± 10K and suggested a new γ phase when β-$Cu_{2-x}Se$ was quenched to liquid nitrogen temperature.

The remaining solid phases are considered as line compounds. Singh and Bhan [30] studied the structure and stability of several compounds by XRD and SEM. Shafizade *et al.* [32] studied the phase transformation of CuSe by heat treatment, while Stevels and Jellinek [25] studied the thermal behavior of copper selenides to 673K and confirmed literature data on transitions involving Cu_3Se_2 and $CuSe_2$. In addition, several crystalline structures [33] were reported for the stoichiometric cuprous selenide at room temperature. Two peritectic reactions are reported in the range $0.5 < x_{Se} < 0.7$. In addition, the system exhibits two liquid

miscibility gaps. The one for Cu-rich compositions exists above 1370K in the range $0.028 < x_{Se} < 0.328$, while the Se-rich gap exists in the range $0.525 < x_{Se} < 0.985$ above 790K.

The thermodynamic data $\Delta H^o_{f,298}$ and S^o_{298} of Cu_2Se, $CuSe$ and $CuSe_2$ were studied by Rau and Rabenau [34] using vapor pressure mea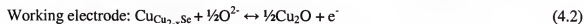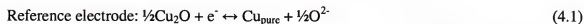surements. Also, there were a number of reports available on the enthalpy and entropy of formation of Cu-Se compounds mainly based on calorimetric [35],[36], thermal analysis [13], EMF methods [37] and the one assessment by K.C. Mills [38]. The most exhaustive list of thermodynamic and phase diagram data is summarized in the recent assessment by Chang [1]. These results, however, show that there is a considerable discrepancy in the enthalpy and entropy of formation data for the binary compound Cu_2Se. Moreover, not much data is available on the thermodynamic stability of this compound. Hence the present investigation was undertaken to determine the thermodynamic stability by EMF and the homogeneity range including the composition of copper rich boundary of β-$Cu_{2-x}Se$.

Experimental

High temperature coulometric titration experiments with solid state electrochemical technique were performed. The electrochemical cells used can be schematically represented as

W, Cu, Cu_2O // YSZ // β-$Cu_{2-x}Se$, Cu_2O, W
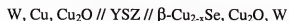
Yittria stabilized zirconia (YSZ) was used as the oxygen-ion conducting solid electrolyte. The half-cell reactions are given by

Reference electrode: $\frac{1}{2}Cu_2O + e^- \leftrightarrow Cu_{pure} + \frac{1}{2}O^{2-}$ (4.1)

Working electrode: $Cu_{Cu_{2-x}Se} + \frac{1}{2}O^{2-} \leftrightarrow \frac{1}{2}Cu_2O + e^-$ (4.2)

The passage of one Faraday of electricity transfers a mole of Cu from the solid solution to pure Cu according to:

Overall reaction: $Cu_{Cu_{2-x}Se} \leftrightarrow Cu_{pure}$ (4.3)

Thus the activity of copper, $a_{[Cu]}$, in the working electrode is related to the open circuit EMF of the cell by:

$$E = (RT \ln a_{[Cu]})/F$$ (4.4)

where F is Faraday's constant (96485.3415 C/mol). R is the gas constant (8.31451 J/K mol) and E is the open circuit potential (V). Operating the cell in the electrolytic mode allows for controlled titration of Cu into or out of the solid solution. The amount of Cu transferred, M in moles, can be calculated by integrating the current and time according to:

$$M = \int \frac{Idt}{nF}$$ (4.5)

where I is the current and n is the equivalent number of ionic charges transferred per mole of reaction. Thus, the knowledge of the initial number of moles or $Cu_{2-x}Se$ allows the change in the value of x to be determined after titration.

In this experiment the cell was initially allowed to reach equilibrium and the open circuit potential was recorded. A constant DC voltage was then applied to the electrochemical cell and the current measured as a function of time. After titration for a predetermined period of time, the electrochemical cell was again placed in open circuit and the EMF monitored until equilibrium was achieved as evidenced by a constant cell potential. If the open circuit EMF did not change after titration, the working electrode was considered to be 2-phase Cu and β-$Cu_{2-x}Se$ or liquid and β-$Cu_{2-x}Se$ (i.e., constant $a_{[Cu]}$). This process was repeated until the Cu content was fully titrated across the single-

phase region. Measured values of temperature and open circuit potential were acquired using LabView.

Reagent grade Cu and Cu_2Se (Alfa Aesar, 99.5 % purity) were used as test electrode materials, while Cu powder and Cu_2O (Johnson Matthey, 99.99% purity) were used as the reference electrode materials. Cylindrical disks of YSZ (Cherry-O), 15 mm in diameter and 3 mm in thickness, served as the O^{2-} conducting electrolyte for the galvanic cell. A thin $Cu_{2-x}Se$ film was deposited onto a disk of YSZ by modulated molecular beam deposition and served as the working electrode. A thin film was required to keep the titration times and thus experimental errors low. The change in Cu mole fraction was calculated from knowledge of the film thickness and deposition diameter. The reference electrode materials were compressed into cylindrical pellets, using a 4:1 weight ratio of Cu/Cu_2O. A spring loading system was employed to ensure mechanical contact between electrode and electrolyte materials and the conducting wire leads. A high density graphite cup enclosing the reference electrode pellet and the YSZ disk was sealed with Aremco 571 magnesia based ceramic adhesive to prevent selenium evaporation. Purified Argon was delivered at a low volumetric rate to provide an inert gas blanket for the cell. The electrode materials were analyzed by XRD before and after each EMF experiment to verify compound stabilities and phase transformations during the experiments.

Results and Discussion

Figure 4.1 shows the assessed Cu-Se phase diagram by Chang [1]. Figure 4.2 summarizes the forward titration (Cu removal) and reverse titration (Cu addition) results using the β-$Cu_{2-x}Se$ thin film, thin pellet and powder electrodes at 899.4K. One reverse titration experiment was also carried out on the β-$Cu_{2-x}Se$ pellet at 895.6K. The results of

forward and reverse titration are in good agreement. The only discrepancy between the three titrations is the Se-rich boundary location, manifested as 2 different plateaus (constant $a_{(Cu)}$) in the data on the right side of Figure 4.2. The difference in the solid solution range when using the different plateau locations, however, is small ($\Delta x=0.012$ vs. 0.011.) It is noted that this technique gives a very accurate value of the change in Cu composition, but does not yield the absolute composition. This is because the starting stoichiometry cannot be accurately determined. In addition, possible composition changes produced by Se loss (high equilibrium pressure of selenium species) were not entirely prevented. Se deposits were observed on the cold regions of the apparatus.
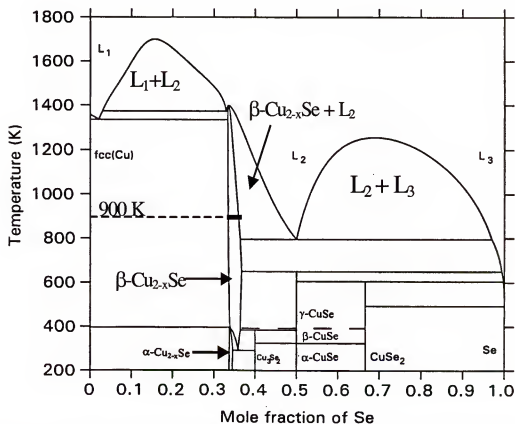
Figure 4.1 Assessed Cu-Se phase diagram by Chang [1] with the measurement range indicated.
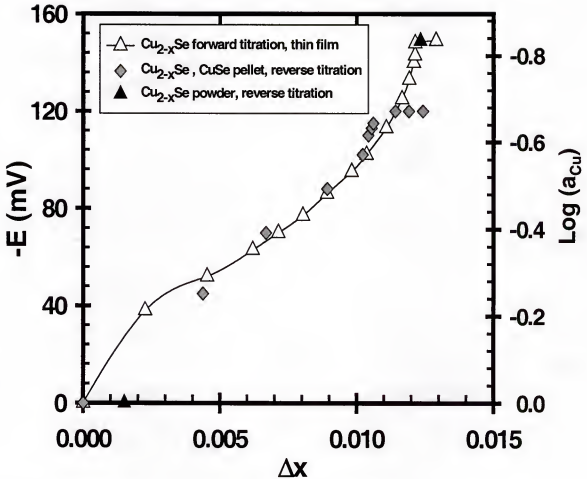
Figure 4.2 Titration curve for β-Cu$_{2-x}$Se at 899.6K.

The experimental measurement also yields the activity of Cu as a function of the alloy composition. In particular the two saturation values corresponding to β-Cu$_{2-x}$Se in equilibrium with pure Cu and β-Cu$_{2-x}$Se in equilibrium with liquid alloy can be related to thermodynamic properties of the other equilibrium phase. For example, the a$_{[Cu]}$ value for an approximately equimolar liquid alloy at 900K shows strong negative deviations from ideal solution behavior in the melt (a$_{[Cu]}$~0.15), consistent with the existence of

immiscibility. Bernardini *et al.* [15] reported an order of magnitude higher value for $\Delta x=0.106$ at 925K from measurements. Aside from that, assessment of selenium vapor pressure data above β-$Cu_{2-x}Se$ suggests that the homogeneity range might be narrower than previous reports [1]. It is noted that Se loss is equivalent to twice the Cu injection, presumably in the back side. Then, the true Cu charge is the sum of the titration and Se loss. Since the titration flux changes sign from forward (+) to reverse (-) titration, the fact that the Δx in both direction given are close suggests that Se loss was not a significant factor. Furthermore, Se loss would continue to occur regardless of the whether the cell was being titrated or not. The EMF of the cell was observed to be steady when in the single phase region for long periods.

Solid State Defect Structure

The high temperature modification of $Cu_{2-x}Se$, β-$Cu_{2-x}Se$, has been proposed to be related to either the B4 (ZnO) or the C1(CaF_2) fcc structure [39]-[45]. All investigators are in agreement that the Se atoms occupy the 4(a) sites and form an fcc sublattice. Except for the proposal of Oliveria *et al.* that all Cu atoms occupy the trigonal 32(f) sites [43], the other investigators are in agreement that Cu atoms reside on two different site types, and only disagree on the types. This structural work suggests that the ordered nonstoichiometric β-$Cu_{2-x}Se$ phase can be divided into three sublattices: one occupied by Se atoms, and the other two by Cu atoms. The structural studies further suggested that the solid solution is a result of formation of vacancies on one or more sublattice. Since the energetics of the two sublattices occupied by Cu atoms are anticipated to be very different, a vacancy is expected to form more easily on the sublattice with higher energy. It is further assumed that the lower energy Cu sublattice is fully occupied by Cu atoms.

As a result, the β-$Cu_{2-x}Se$ phase described in Chang [1]`s assessment by the sublattice model with three sublattices is represented as:

$$(Cu,Va)_1(Se,Va)_1(Cu)_1 \qquad\qquad (4.6)$$

where Va represents a vacancy on the Se or Cu sublattice. Although the concentration of vacancies on the Se sublattice is expected to be small, it was included in the model. The subsequent assessment results of Chang [1] indicate that the vacancy concentration on the Se sublattice is very small, which is in good agreement with the structural information.

An assessment of the vapor pressure data for pure Se species in equilibrium with solid and liquid Se performed by Chang [1] is presented in Figure 4.3. Eight molecular species (Se; n=1-8) were assumed to exist in the equilibrium mixture. Below the melting temperature of selenium (494K), Se_6 is the major species in the gas phase. Se_5 is the dominant species, however, between 600 and 1000K.
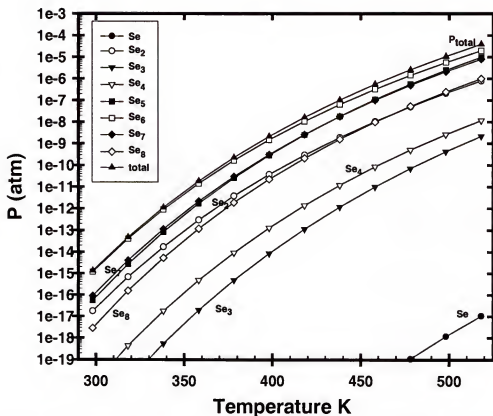
Figure 4.3 Assessed selenium vapor pressures over solid selenium between 298 and 494K by Chang [1].

Figure 4.4 summarizes the available vapor pressure data for the Cu-Se system, including data along the single-phase β-$Cu_{2-x}Se$ boundaries. In these calculations, the gas phase was assumed to be an ideal gas mixture of the 12 species: Se, Se_2, Se_3, Se_4, Se_5, Se_6, Se_7, Se_8, Cu, Cu_2, CuSe, and Cu_2Se. Analysis of the low temperature assessment indicates that Se_2 is not the most dominant species for all temperature ranges, especially in the gas-solid equilibrium temperature range of interest. Gas species compositional fractions are a strong function of temperature below 1000K. The calculated Se_2 partial pressures agree well with the measured data of [34] except those in the low pressure fcc(Cu)/β-$Cu_{2-x}Se$ region. An attempt to fit those data resulted in poor fits to other experimental data, including the experimental Se_2 partial pressures in other regions [34].

The low-pressure data were measured by reacting H_2 with a Cu-Cu$_{2-x}$Se mixture and analyzing the transported H_2Se. Incomplete reaction would lower the measured vapor pressure. The higher-pressure data were measured by either gas transpiration or total pressure measurements.
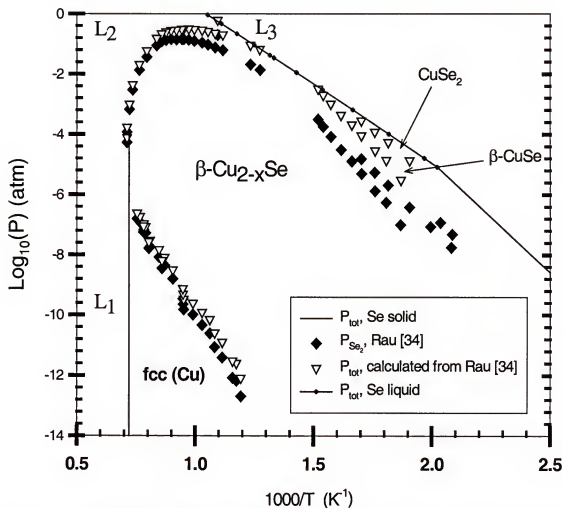
Figure 4.4 Experimental Se$_2$ partial pressures and calculated total pressures in the Cu-Se system.
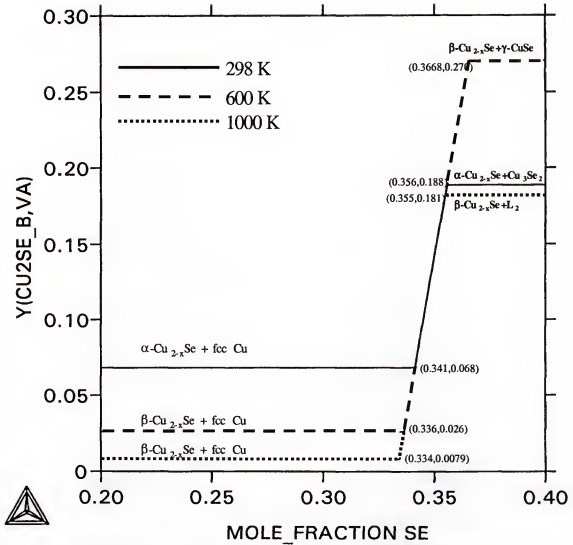
Figure 4.5 The calculated site fractions of Cu vacancy on the first sublattice for the β-Cu$_{2-x}$Se (600,1000K) and α-Cu$_{2-x}$Se (298K) phases.

The calculated [1] site fractions of Cu vacancies in the β-Cu$_{2-x}$Se phase are shown in Figure 4.5 at three temperatures. The calculated concentration of the Se vacancies was relatively small. In the β-Cu$_{2-x}$Se single-phase region, the Cu vacancy concentration on the first sublattice increases and the Se vacancy concentration decreases with increasing selenium concentration. It is observed that the calculated Cu vacancy concentration on the first sublattice (0.008 < $y_{[V_{Cu}]}$ < 0.27) is considerably larger than the Se vacancy

concentration ($10^{-17} < y_{[V_{Cu}]} < 2.23 \times 10^{-4}$) between 298 and 1000K. Although no experimental data are available for comparison, the very limited Se vacancy and large Cu vacancy concentrations are consistent with the results and density structural investigations [25], [41], [45], [46].

Defect Model Based on External Gas Phase Equilibrium

An assessment of gas-solid equilibrium is required to investigate the effects of gas phase species on equilibrium kinetics and defect mechanisms in the solid structure. Copper deficiency and other irregularities in the solid structure may be modeled by electronic and ionic defect mechanisms and the equilibrium between the solid and gas phase reactions can be associated with defect formation. The recent assessment of solid and liquid selenium equilibrium vapor pressures and measured $Cu_{2-x}Se$ vapor pressures along with calculated data from the assessed thermodynamic functions will be used to explore defect formation mechanisms.

Theory

According to the limits of wide homogeneity range of $Cu_{2-x}Se$ and experimental results previously mentioned, an overall effective deficiency on copper sites is assumed. The semiconductor type of properties of the $Cu_{2-x}Se$ can be described by the vacancy formation on the Cu lattice. However, atomic defects in solids, for example vacancies on copper lattice sites in cuprous selenide, can appear in many different forms and formation energy levels. Normally, it is not practical to identify and categorize all types of atomic defects in the crystal configuration; however, statistical analysis of defect equilibria provides useful information about defect types and predominance regions.

In this work , only thermodynamic and chemistry related irregularities in crystal structures will be referred to. Other structural defects such as cavity or dislocational defect formations or their thermodynamics are not discussed. Generally, sources of electronic defects in a crystal are described by either extra valence electrons or missing valence electrons. In addition, atomic types of defects can occur in the form of vacancies, interstitials, misplaced atoms or foreign atoms or combinations of different defect types. Understanding of defect types in a crystal can be very complicated because of difficulty in defining the equilibrium thermodynamic variables of the defect equilibria.

Any defect formation in a crystalline phase results in an increase in the configurational entropy. Due to replacement of particles or electronic effects including the band movement of electrons and holes, atomic structure may contain holes, vacancies or defect pairs at variety of different energy levels. The introduction of vacancy or any other interstitialcy in the crystal structure produces vibrational frequency differences in periodic structure. As a result, the free vibration distance between specific atoms can be altered. In general, vacancy formations dampen vibration of atoms around vacancies, which can cause the modification of configurational ordering and structural changes. Vibrational entropy can also change by vacancy or electron-hole pair formation. Total entropy change for a defect formation in a crystalline state is due to both vibrational and configurational entropy production since the coordination numbers of vacancies or atom sites are altered by configurational displacements. The vibrational entropy change equation by the formation of a vacancy was introduced by Mott and Guerney(1940),

$$\Delta S_v^{vib} = x \, k \, \ln(\nu^{pc}/\nu') \tag{4.7}$$

where x is the coordination number for the vacancy and v^{pc} and v' are the vibrational frequencies of the perfect lattice atom and of the surrounding atoms respectively. For a vacancy formation, it is expected that surrounding atoms will have lower vibrational frequencies (faster movements), which results in positive values in ΔS_v^{vib}. In other words, any formation that causes deviations in perfect crystal structure increases the total entropy of the system.

Free Energy Curves

Free energy change for formation of vacancies or defects is associated with vibrational and configurational entropy functions. Formation of defects in a crystal structure can be best described by a statistical approach. For an elementary crystal with N lattice sites and n defects (holes, vacancies, interstitials, etc.,) the number of possible configurations of these defect sites is related to the production of the configurational entropy of the crystal. The configurational entropy output, ΔS_c, is proportional to the divergence from perfect structure and can be represented as

$$\Delta S_c = k \ln [\Omega], \tag{4.8}$$

where Ω is the number of possible configurations for the defect structure, which can be represented as

$$\Omega = N! / [(N - n)! n!] \tag{4.9}$$

where N and n represent the total number of lattice sites in perfect lattice and the number of point defects respectively The total free energy change to introduce n defects in a crystal is given by the following relation,

$$\Delta G = G - G^{pc} = n\Delta H_d - (T\Delta S_c + nT\Delta S_d^{vib}) \tag{4.10}$$

where G^{pc} is the free energy of the perfect crystal, ΔH_d is the enthalpy of formation of a defect, ΔS_c and ΔS_d^{vib} are configurational entropy and vibrational entropy change by defect formation.

Thermodynamically speaking, there are many different paths and energy levels that can be considered in explaining overall copper deficiency of $Cu_{2-x}Se$. Overall, the atomic depletion from copper sites or the penetration of Se into the crystal structure may produce the same overall deficiency. The further investigation of the causes of wide homogeneity range of $Cu_{2-x}Se$ is not the objective of this work. However, it is noted that defects are strongly related with crystal structure changes depending upon strength and type of chemical bonding between molecules. Dimensional and molecular configurations of atoms and molecules also take part in deciding the stability of any configurational changes.

Defect Model

In general for a defect semiconductor, equilibrium for electronic defects is represented as

$$\phi \leftrightarrow [e'] + [h^\bullet] \tag{4.11}$$

where $[e']$ and $[h^\bullet]$ represent the electron and hole concentration respectively. The equilibrium reaction constant is represented as

$$K_i = n \cdot p \tag{4.12}$$

where

$\quad K_i \qquad$: intrinsic electron-hole pair constant

$\quad n \qquad$: electron concentration

$\quad p \qquad$: hole concentration

Quasi-chemical reaction for copper in equilibrium with gas phase can be written as

$$Cu(in\ Cu_2Se) \leftrightarrow Cu_g \qquad (4.13)$$

Similarly ionic defect equilibrium reaction can be represented as

$$Cu_2Se \leftrightarrow [V_{Cu}'] + [Cu_i^{\bullet}] \qquad (4.14)$$

$$K_d = [V_{Cu}'] \cdot [Cu_i^{\bullet}] \qquad (4.15)$$

where

K_d : defect equilibrium reaction constant

$[V_{Cu}']$: vacancy concentration on copper sites,

$[Cu_i^{\bullet}]$: copper concentration on interstitial sites.

A composition relation and law of mass action for equilibrium with the adjacent phase requiring the point defect equilibrium with the gas phase can be represented as

$$\tfrac{1}{2}Se_2 \leftrightarrow [V_{Cu}'] + Se_{Se}^x + h^{\bullet} \qquad (4.16)$$

$$\tfrac{1}{2}Se_2 \leftrightarrow Se_i' + h^{\bullet} \qquad (4.17)$$

Although the equilibrium reactions given by (4.16) and (4.17) can basically represent the same overall deficiency, selenium interstitialcy given in the Equation (4.17) is not considered as the main defect mechanism in the model. There is not much experimental data on defect density or defect mechanisms Although the model deals with overall defect concentrations rather than all individual defect mechanisms, the calculation results will provide means to make useful comparisons or estimations about defect mechanisms and the overall deficiency assumption.

The equilibrium relation for electrochemical reaction in (4.16) can be represented as

$$K_x = \left([V_{Cu}'] \cdot p \right) / P_{Se_2}^{1/2} \tag{4.18}$$

where K_x is defined as the external equilibrium constant.

External equilibrium reaction has a controlling role in defect formation. To obtain overall solution of the equilibrium equations the charge neutrality relation must also be included, which can be represented as:

$$[V_{Cu}'] + n = p + [Cu_i^{\cdot}], \tag{4.19}$$

Assuming that for each vacancy formation an intrinsic hole defect is produced ($[V_{Cu}']$=p), and combining the Equations (4.18) and (4.19),

$$K_x = [V_{Cu}']^2 / P_{Se_2}^{1/2} \tag{4.20}$$

$$[V_{Cu}'] = (K_x)^{1/2} P_{Se_2}^{1/4} \tag{4.21}$$

In general, *defect concentration* $\sim (P_{Se_m})^{1/n}$ is obtained. The symbol n stands for the number of type of defects that may occur in the solid structure for each m species in the gas phase. Copper vacancy concentration is directly related to the fraction of unoccupied sites or homogeneity range by the following expression,

$$[V_{Cu}'] \sim x \tag{4.22}$$

where x represents the fraction of deficiency given in the molecular formula of $Cu_{2-x}Se$. The Equation (4.20) can be written in terms of defect composition [x] and partial pressure as

$$K_x = \left([x]^2 / P_{Se_2}^{1/2} \right) \tag{4.23}$$

Since K_x is the defect equilibrium constant, the Gibbs energy change (ΔG) of this reaction is equivalent to the Gibbs energy of formation of an ionized vacancy on copper sites.

$$\Delta G_v = \Delta G_{ext} = -RT \ln K \qquad (4.24)$$

$$K_x = \left([x]^2 / P_{Se_2}^{1/2} \right) = exp \left(- \Delta G_v / RT \right) \qquad (4.25)$$

Copper vacancy concentration is found to be proportional to (1/4) power of the partial pressure of Se_2 species. Since the power term is determined by the stoichiometry of the external equilibrium reaction, the Equation (4.23) can be adapted for all species by changing the power term based on the stoichiometry. Selenium vapor pressures from the unary assessment and overall vapor pressure data with temperature are presented in Figures 4.3 and 4.4. Individual defect reactions corresponding to different stoichiometric representations of gas phase selenium species in the temperature range can be calculated from the data given in these figures.
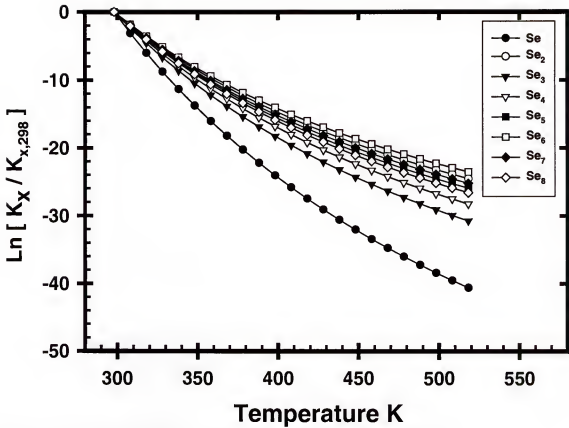
Figure 4.6 Defect equilibrium constants for x=0.188 with temperature.

Figure 4.6 illustrates the calculated defect equilibrium constants with temperature at a constant defect concentration ($x_{[Cu_{2-x}Se]}$=0.188). A general comparison of influences of individual species and their relative contribution with temperature to overall defect composition can be obtained from this figure. In short, all defect reactions show a decreasing trend in the temperature range; however, the individual contributions to overall equilibrium at each temperature region must be investigated to make better judgment.
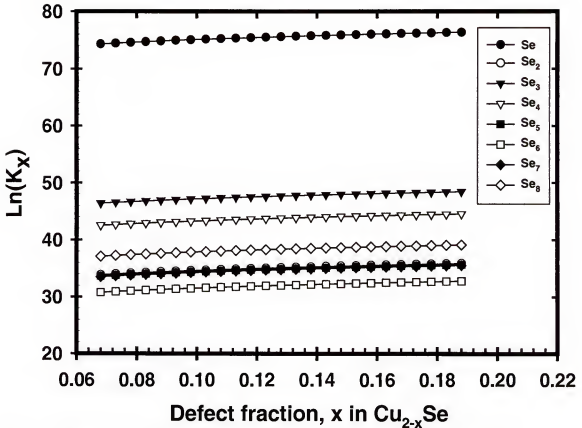
Figure 4.7 Defect equilibrium along the homogeneity range calculated for 298 K.

Since we have equilibrium between defective solid and gas, the gas species are also in equilibrium. Thus, one can use any species, Se_n to interact with the solid. All other P_{Se_n} are easily calculated since equilibrium exists.

Generally, the defect characteristics and electronic properties of Cu_2Se can be managed entirely by referring Figures 4.6 and 4.7. In addition, a defect equilibrium diagram (DED) can be constructed, which is an indication of semiconducting properties. The DED provides useful information by combining vapor pressure and defect concentrations. Figure 4.8 displays the calculated defect concentrations in multiple dominance regions for $Cu_{2-x}Se$ at 298K. It is characteristically very similar to the conductivity curve and it can provide useful information in deposition studies to

predetermine the ionic or electronic conductivity characteristics. Although Figure 4.8 is plotted for only one temperature, the same calculating principles can be applied to map out the whole defect predominance diagrams for different temperatures.

The defect equilibrium diagram is calculated by common solution of Equations (4.12), (4.15), (4.18) and (4.19). Equations (4.12) and (4.18) are combined for the expression for vacancy concentration, which is represented as

$$[V_{Cu}'] = \frac{K_x [P_{Se_2}^{1/4}] n}{K_i} \tag{4.26}$$

Similarly, the common solution of Equations (4.12), (4.15), and (4.18) for the interstitial defect concentration succeeds the following expression,

$$[Cu_i^{\bullet}] = \frac{K_d K_i}{K_x [P_{Se_2}^{1/2}] n} \tag{4.27}$$

By eliminating the repeated independent variables in each equation, defect concentration equations can be represented as a function of single variable as follows

$$n = K_i \left[\frac{K_d + F}{F(K_i + F)} \right]^{1/2} \tag{4.28}$$

$$p = K_i \left[\frac{F(K_i + F)}{K_d + F} \right]^{1/2} \tag{4.29}$$

$$[Cu_i^{\bullet}] = K_d \left[\frac{(K_i + F)}{F(K_d + F)} \right]^{1/2} \tag{4.30}$$

$$[V_{Cu}'] = \left[\frac{F(K_d + F)}{(K_i + F)} \right]^{1/2} \tag{4.31}$$

where $F = K_x [P_{Se_2}^{1/2}]$ \tag{4.32}

K_i is calculated as $3.22*10^{18}$ (charge/cm^3)^2 from the following equation,

$$K_i = p \cdot n = N_c N_v \exp\left[\frac{-(E_c - E_v)}{kT} \right] \qquad (4.33)$$

where N_c is defined as the effective density of states. It is calculated to be $2.5*10^{19}$ cm^{-3} at 298K with assuming equal electron mass and electron effective mass($m_e^* = m_e$). Intrinsic conditions and the band gap value of 1.2 eV for Cu$_{2-x}$Se at 298K are assumed. K_d is directly calculated from the values of defect concentrations presented in the latest assessment performed by Chang [1]. To be consistent with the defect mechanism proposed first, the concentration of interstitial defects are assumed to be negligible compared to the vacancy concentration. Consequently, the maximum value of K_d is estimated to be $3.6759 \ 10^{21}$ (charge/cm^3)^2 [(0.188*6.02*10^{23}charge/mol)*(6.69g/cm^3) *((1/206.05)mol/gr)] The expressions for the "effective" density of conduction band states N_c and the "effective" density of valence band N_v and effective mass and Fermi level assumptions during the calculation of carrier concentration expressions are obtained from [47].
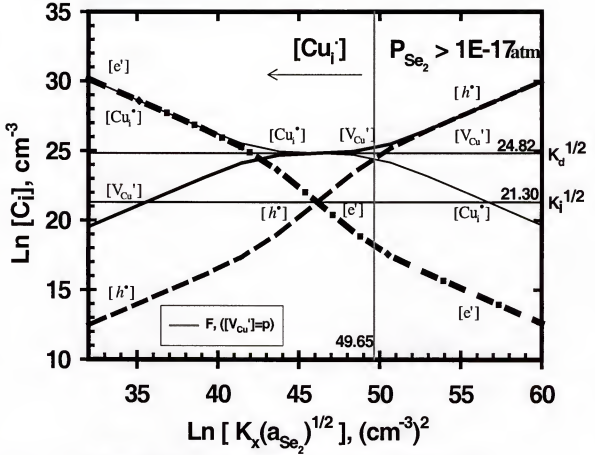
Figure 4.8 The defect equilibrium diagram of α-Cu$_{2-x}$Se calculated for 298 K.

Gibbs Energy Calculations

In general, a defect equilibrium relation can be written for each stable species of selenium as

$$K_x = \left(x^2 / P_{Se_m}^{1/n} \right) \tag{4.34}$$

where m is attributed to the stoichiometry of selenium species in the gas phase.

$$K_x = K_{[V_{Cu}']} \tag{4.35}$$

$$\Delta G_v = G - G^{pc} = n\left[\Delta H_v - T\,\Delta S_v^{vib}\right] - T\,k\,\Delta S_c \tag{4.36}$$

$$\Delta G_v = n\left[\Delta H_v - T\,\Delta S_v^{vib}\right] - T\,k\,\ln\left[\frac{N!}{(N-n)!\,n!}\right] \qquad (4.37)$$

The equilibrium condition asserts that the derivative of the Gibbs energy change (ΔG) expression associated with the formation of vacancy be zero at equilibrium. It is noted that the derivative of ΔG_v with respect to defect concentration can be solved for the maximum, which leads to the equilibrium concentration by assuming random and non-interacting defects.

$$\left(\frac{\partial \Delta G_v}{\partial n_i}\right)_{T,P,n_i \neq j} = 0 \qquad (4.38)$$

$$\frac{\partial}{\partial n}\left\{n\left[\Delta H_v - T\,\Delta S_v^{vib}\right] - T\,k\,\ln\left[\frac{N!}{(N-n)!\,n!}\right]\right\} = 0 \qquad (4.39)$$

$$k\,T\,\ln\left[\frac{(N-n)}{n}\right] = \Delta H_v - T\,\Delta S_v^{vib} \qquad \text{,or} \qquad (4.40)$$

$$-k\,T\,\ln\left[\frac{n}{(N-n)}\right] = \Delta H_v - T\,\Delta S_v^{vib} \qquad (4.41)$$

$$k\,T\,\ln\left[\frac{n}{(N-n)}\right] = T\,\Delta S_v^{vib} - \Delta H_v \qquad (4.42)$$

for $n \ll N$, $[x] \equiv \dfrac{n}{(N-n)} = \dfrac{n}{N}$ is true $\qquad (4.43)$

where [x] is the defect concentration. Deriving for [x], the equation (4.43) leads the following relation,

$$\frac{n}{(N-n)} = [x] = e^{\left(\frac{\Delta S_v^{vib}}{k}\right)}\,e^{\left(\frac{-\Delta H_v^0}{kT}\right)} \qquad (4.44)$$

The right hand side of the equation (4.44) involves only vibrational terms. The configurational entropy term vanishes and equilibrium defect concentration x is dependent upon only vibrational terms. Similarly, the external equilibrium coefficient does not contain any configurational entropy, ΔS_c.

$$K_x = \left([x]^2 / P_{Se_m}^{1/n}\right) = \exp(-\Delta G_v / RT) \tag{4.45}$$

and according to equation (4.25),

$$K_x = \left([x]^2 / P_{Se_m}^{1/n}\right) = \exp\left(\frac{\Delta S_{V_{Cu}}^{vib}{}'}{R}\right) \exp\left(\frac{-\Delta H_{V_{Cu}}^0{}'}{RT}\right) \tag{4.46}$$

Equations (4.44) and (4.46) lead

$$[x_v] \cong K_x \text{ where R=kN}_A \tag{4.47}$$

$$\Delta \overline{G}_{Se_m} = \overline{G}_{Se_m} - G_{Se_m}^0 = \mu_{Se_m} - \mu_{Se_m}^0 = RT \ln P_{Se_m} \tag{4.48}$$

The relative partial molar Gibbs energy of a gas phase species can be obtained from the assessed data given in Figures 4.4 and 4.5. Equations (4.48) and (4.50) allow to associate the defect concentration relations with structural changes by using equilibrium pressures. Figures 4.9-4.16 illustrate $ln[x]$ vs. ΔG curves for different temperatures. Slopes of each curve n are attributed to individual defect reactions corresponding to specific defect types. The different slopes of different curves means different defect energy levels along with different defect mechanism. Analysis of experimental data is vital for better understanding of these defect formations and their effects on the crystal structure. Figures 4.9-4.16 exhibit that defect reactions generally become complicated when temperature is increased. However, between 358 and 458K there is a distinctive deviation on temperature dependence. Figures 4.17-4.21 depict the partial free energies of

selenium compounds as a function of composition and temperature. Rearranging the Equation (4.46) leads the following expression,

$$P_{Se_m}^{1/n} = [x]^2 \exp\left(\frac{-\Delta S_{V_{Cu}^{'}}^{vib}}{R}\right) \exp\left(\frac{\Delta H_{V_{Cu}^{'}}^{0}}{RT}\right) \tag{4.49}$$

By combining equations (4.48) and (4.49), the following expressions can be obtained,

$$\Delta \overline{G}_{Se_m} = \Delta \overline{H}_{Se_2} - T\Delta \overline{S}_{Se_m} = RT \ln\left([x]^2 \exp\left(\frac{-\Delta S_{V_{Cu}}^{vib}}{R}\right) \exp\left(\frac{\Delta H_{V_{Cu}^{'}}^{0}}{RT}\right)\right)^n \tag{4.50}$$

$$\Delta \overline{S}_{Se_m} = n\Delta S_{V_{Cu}^{'}}^{vib} - 2nR \ln[x] \tag{4.51}$$

$$\Delta \overline{H}_{Se_m} = n\Delta H_{V_{Cu}^{'}}^{0} \tag{4.52}$$

The main assumption in these derivations is that defects are spread randomly without interaction. As a result, the relative enthalpy and entropy term contributions can be accepted as independent of composition. As a result, the derivative of relative entropy term is a constant value. According to the assumption that vibrational entropy is independent of composition, the equation (4.51) can be rearranged as

$$\frac{\partial \Delta \overline{S}_{Se_m}}{\partial \ln[x]} = -2nR \tag{4.53}$$

For different n values or different selenium content, the slopes of $ln[x]$ vs. $\Delta \overline{S}_{Se_m}$ curves will be different. Any slope change on straight lines may represent different lattice structure or ionization states of defects. It is not necessary at this point to analyze details of these ionization steps. However, it is intended to present the idea that these relations can be easily applied when necessary. However, it is noted that for higher temperatures

there is not sufficient and reliable experimental study available for a vigorous comparison.

Conclusions

The homogeneity range of $Cu_{2-x}Se$ was investigated by electrochemical titration using solid state galvanic cells. A novel defect model was proposed to explain the observed homogeneity range in terms of defect chemistry and the equilibrium relationship between solid and gas phase species.

Measurement of the range of solid solution in $\beta-Cu_{2-x}Se$ was performed at 900K. Both forward and reverse titration suggested that the composition difference between the selenium-rich and the copper-rich boundaries was $\Delta x=0.012$ at 900K. This value is less than a previous measurement, and somewhat smaller than estimates obtained from the assessment results. The Cu activity at the Cu-rich boundary of $\beta-Cu_{2-x}Se$ was unity, consistent with no solubility of Se in fcc-Cu. At the Se-rich boundary of $\beta-Cu_{2-x}Se$ the Cu activity was ~0.15. Since the liquidus composition at 900K is nearly equimolar, strong negative deviations in the solution behavior are evident.

A point defect model was developed to account for the extended range of solid solution that has Cu vacancies as the main defect. The model interconnected the defect formation enthalpy and vibrational entropy changes to partial free energy relations. A complete defect equilibrium diagram was presented for 298 K by the assistance of gas-solid equilibrium assessment. The number of theoretical defect mechanisms and the Gibbs energy of formation of defects can be estimated from the developed model. The effects of temperature and gas phase stoichiometry on the defect formation mechanisms were examined. The defect formation reactions showed complex dependency on

temperature, pressure and the selenium content of the gas phase. The defect model presented provides a better understanding of the relationship between gas and solid phase interaction in terms of point defect formation mechanisms. Higher temperature defect chemistry can be explored by following the same strategy.

Table 4.1 Defect formation enthalpy and vibrational entropy changes for Se_1.

x=0.15	Temperature K				
	298.15	358.15	408.15	458.15	508.15
$\Delta \bar{S}_{Se}$ kcal/mol K	0.264914	-0.01388	0.044666	0.003019	0.105164
$\Delta \bar{H}_{Se}$ kcal/mol	31.77071	-50.8383	-26.3923	-41.9401	11.4456
$\Delta \bar{G}_{Se}$ kcal /mol	-47.2133	-45.8689	-44.6229	-43.3234	-41.9935
$\Delta S^{vib}_{v_{Cu}}$ kcal/mol K	0.25462	-0.02417	0.034373	-0.00727	0.09487
$\Delta H^0_{v_{Cu}}$ kcal/mol	31.77071	-50.8383	-26.3923	-41.9401	11.4456
x=0.2					
$\Delta \bar{S}_{Se}$ kcal/mol K	0.266057	-0.01273	0.04581	0.004163	0.106307
$\Delta \bar{H}_{Se}$ kcal/mol	32.45239	-50.0194	-25.4591	-40.8925	12.60746
$\Delta \bar{G}_{Se}$ kcal /mol	-46.8724	-45.4595	-44.1562	-42.7996	-41.4126
$\Delta S^{vib}_{v_{Cu}}$ kcal/mol K	0.256906	-0.02188	0.036659	-0.00499	0.097157
$\Delta H^0_{v_{Cu}}$ kcal/mol	32.45239	-50.0194	-25.4591	-40.8925	12.60746
x=0.25					
$\Delta \bar{S}_{Se}$ kcal/mol K	0.266944	-0.01185	0.046696	0.005049	0.107194
$\Delta \bar{H}_{Se}$ kcal/mol	32.98125	-49.3842	-24.7352	-40.08	13.50874
$\Delta \bar{G}_{Se}$ kcal /mol	-46.6081	-45.1419	-43.7943	-42.3933	-40.962
$\Delta S^{vib}_{v_{Cu}}$ kcal/mol K	0.25868	-0.02011	0.038433	-0.00321	0.09893
$\Delta H^0_{v_{Cu}}$ kcal/mol	32.98125	-49.3842	-24.7352	-40.08	13.50874
x=0.3					
$\Delta \bar{S}_{Se}$ kcal/mol K	0.267668	-0.01112	0.047421	0.005774	0.107919
$\Delta \bar{H}_{Se}$ kcal/mol	33.41331	-48.8652	-24.1438	-39.4161	14.2451
$\Delta \bar{G}_{Se}$ kcal /mol	-46.392	-44.8824	-43.4986	-42.0614	-40.5938
$\Delta S^{vib}_{v_{Cu}}$ kcal/mol K	0.260129	-0.01866	0.039882	-0.00177	0.10038
$\Delta H^0_{v_{Cu}}$ kcal/mol	33.41331	-48.8652	-24.1438	-39.4161	14.2451

Table 4.2 Defect formation enthalpy and vibrational entropy changes for Se_2.

	Temperature K				
x=0.15	**298.15**	**358.15**	**408.15**	**458.15**	**508.15**
$\Delta\overline{S}_{Se_2}$ kcal/mol K	1.007798	-0.14399	0.002518	0.089537	0.021623
$\Delta\overline{H}_{Se_2}$ kcal/mol	253.9495	-87.5325	-39.1681	3.918583	-22.9803
$\Delta\overline{G}_{Se_2}$ kcal/mol	-46.5254	-35.9628	-40.1959	-37.1029	-33.9681
$\Delta S^{vib}_{V_{Cu}}$ kcal/mol K	0.98721	-0.16458	-0.01807	0.06895	0.001036
$\Delta H^0_{V_{Cu}}$ kcal/mol	126.9747	-43.7662	-19.5841	1.959292	-11.4902
x=0.2					
$\Delta\overline{S}_{Se_2}$ kcal/mol K	0.996589	-0.13858	0.006279	0.090867	0.026179
$\Delta\overline{H}_{Se_2}$ kcal/mol	251.2893	-84.9142	-36.6998	5.5752	-19.5036
$\Delta\overline{G}_{Se_2}$ kcal /mol	-45.8437	-35.2811	-39.2626	-36.0554	-32.8062
$\Delta S^{vib}_{V_{Cu}}$ kcal/mol K	0.978288	-0.15688	-0.01202	0.072566	0.007878
$\Delta H^0_{V_{Cu}}$ kcal/mol	125.6446	-42.4571	-18.3499	2.7876	-9.75179
x=0.25					
$\Delta\overline{S}_{Se_2}$ kcal/mol K	0.987894	-0.13439	0.009196	0.091898	0.029712
$\Delta\overline{H}_{Se_2}$ kcal/mol	249.2258	-82.8833	-34.7853	6.860187	-16.8069
$\Delta\overline{G}_{Se_2}$ kcal /mol	-45.3149	-34.7523	-38.5388	-35.2428	-31.905
$\Delta S^{vib}_{V_{Cu}}$ kcal/mol K	0.971367	-0.15092	-0.00733	0.07537	0.013185
$\Delta H^0_{V_{Cu}}$ kcal/mol	124.6129	-41.4416	-17.3926	3.430093	-8.40343
x=0.3					
$\Delta\overline{S}_{Se_2}$ kcal/mol K	0.980791	-0.13096	0.01158	0.09274	0.032599
$\Delta\overline{H}_{Se_2}$ kcal/mol	247.5398	-81.2239	-33.221	7.910092	-14.6035
$\Delta\overline{G}_{Se_2}$ kcal /mol	-44.8829	-34.3202	-37.9473	-34.5789	-31.1686
$\Delta S^{vib}_{V_{Cu}}$ kcal/mol K	0.965712	-0.14604	-0.0035	0.077662	0.017521
$\Delta H^0_{V_{Cu}}$ kcal/mol	123.7699	-40.6119	-16.6105	3.955046	-7.30173

Table 4.3 Defect formation enthalpy and vibrational entropy changes for Se$_3$.

x=0.15	Temperature K				
	298.15	358.15	408.15	458.15	508.15
$\Delta \overline{S}_{Se_3}$ kcal/mol K	1.757	-0.26493	-0.03172	0.182641	-0.05514
$\Delta \overline{H}_{Se_3}$ kcal/mol	431.8052	-166.643	-93.9848	7.88457	-98.5459
$\Delta \overline{G}_{Se_3}$ kcal /mol	-92.0442	-71.757	-81.0374	-75.7924	-70.527
$\Delta S_{V_{Cu}}^{vib}$ kcal/mol K	1.726118	-0.29581	-0.0626	0.15176	-0.08602
$\Delta H_{V_{Cu}}^{0}$ kcal/mol	143.9351	-55.5475	-31.3283	2.62819	-32.8486
x=0.2					
$\Delta \overline{S}_{Se_3}$ kcal/mol K	1.740186	-0.25682	-0.02608	0.184635	-0.04831
$\Delta \overline{H}_{Se_3}$ kcal/mol	427.8149	-162.715	-90.2824	10.3695	-93.3308
$\Delta \overline{G}_{Se_3}$ kcal /mol	-91.0216	-70.7344	-79.6376	-74.2211	-68.7842
$\Delta S_{V_{Cu}}^{vib}$ kcal/mol K	1.712735	-0.28427	-0.05353	0.157184	-0.07576
$\Delta H_{V_{Cu}}^{0}$ kcal/mol	142.605	-54.2384	-30.0941	3.4565	-31.1103
x=0.25					
$\Delta \overline{S}_{Se_3}$ kcal/mol K	1.727145	-0.25053	-0.0217	0.186182	-0.04301
$\Delta \overline{H}_{Se_3}$ kcal/mol	424.7197	-159.669	-87.4106	12.29697	-89.2857
$\Delta \overline{G}_{Se_3}$ kcal /mol	-90.2284	-69.9413	-78.5518	-73.0022	-67.4324
$\Delta S_{V_{Cu}}^{vib}$ kcal/mol K	1.702353	-0.27532	-0.0465	0.161391	-0.0678
$\Delta H_{V_{Cu}}^{0}$ kcal/mol	141.5732	-53.2229	-29.1369	4.09899	-29.7619
x=0.3					
$\Delta \overline{S}_{Se_3}$ kcal/mol K	1.716489	-0.24539	-0.01813	0.187446	-0.03868
$\Delta \overline{H}_{Se_3}$ kcal/mol	422.1908	-157.18	-85.0641	13.87182	-85.9806
$\Delta \overline{G}_{Se_3}$ kcal /mol	-89.5804	-69.2932	-77.6646	-72.0064	-66.3278
$\Delta S_{V_{Cu}}^{vib}$ kcal/mol K	1.693871	-0.26801	-0.04075	0.164828	-0.06129
$\Delta H_{V_{Cu}}^{0}$ kcal/mol	140.7303	-52.3933	-28.3547	4.62394	-28.6602

Table 4.4 Defect formation enthalpy and vibrational entropy changes for Se_4.

x=0.15	Temperature K				
	298.15	**358.15**	**408.15**	**458.15**	**508.15**
$\Delta \bar{S}_{Se_4}$ kcal/mol K	2.109617	-0.3242	-0.04945	0.225415	-0.09318
$\Delta \bar{H}_{Se_4}$ kcal/mol	515.4589	-204.874	-120.702	8.949933	-135.47
$\Delta \bar{G}_{Se_4}$ kcal /mol	-113.523	-88.7614	-100.519	-94.324	-88.122
$\Delta S^{vib}_{V_{Cu}}$ kcal/mol K	2.068442	-0.36538	-0.09062	0.18424	-0.13435
$\Delta H^0_{V_{Cu}}$ kcal/mol	128.8647	-51.2184	-30.1755	2.237483	-33.8676
x=0.2					
$\Delta \bar{S}_{Se_4}$ kcal/mol K	2.087199	-0.31339	-0.04193	0.228074	-0.08407
$\Delta \bar{H}_{Se_4}$ kcal/mol	510.1384	-199.637	-115.766	12.26319	-128.517
$\Delta \bar{G}_{Se_4}$ kcal /mol	-112.16	-87.398	-98.6529	-92.2289	-85.7982
$\Delta S^{vib}_{V_{Cu}}$ kcal/mol K	2.050597	-0.34999	-0.07853	0.191472	-0.12067
$\Delta H^0_{V_{Cu}}$ kcal/mol	127.5346	-49.9093	-28.9414	3.065796	-32.1293
x=0.25					
$\Delta \bar{S}_{Se_4}$ kcal/mol K	2.06981	-0.305	-0.03609	0.230136	-0.077
$\Delta \bar{H}_{Se_4}$ kcal/mol	506.0115	-195.575	-111.937	14.83314	-123.123
$\Delta \bar{G}_{Se_4}$ kcal /mol	-111.102	-86.3404	-97.2051	-90.6038	-83.9958
$\Delta S^{vib}_{V_{Cu}}$ kcal/mol K	2.036755	-0.33805	-0.06915	0.197081	-0.11006
$\Delta H^0_{V_{Cu}}$ kcal/mol	126.5029	-48.8938	-27.9841	3.708285	-30.7809
x=0.3					
$\Delta \bar{S}_{Se_4}$ kcal/mol K	2.055602	-0.29814	-0.03133	0.231821	-0.07123
$\Delta \bar{H}_{Se_4}$ kcal/mol	502.6395	-192.257	-108.808	16.93295	-118.717
$\Delta \bar{G}_{Se_4}$ kcal /mol	-110.238	-85.4763	-96.0222	-89.276	-82.5231
$\Delta S^{vib}_{V_{Cu}}$ kcal/mol K	2.025445	-0.3283	-0.06148	0.201665	-0.10138
$\Delta H^0_{V_{Cu}}$ kcal/mol	125.6599	-48.0642	-27.202	4.233238	-29.6792

Table 4.5 Defect formation enthalpy and vibrational entropy changes for Se$_5$.

x=0.15	Temperature K				
	298.15	**358.15**	**408.15**	**458.15**	**508.15**
$\Delta \overline{S}_{Se_5}$ kcal/mol K	2.143415	-0.25447	0.017744	0.28778	-0.02474
$\Delta \overline{H}_{Se_5}$ kcal/mol	523.4149	-178.554	-88.4594	45.55541	-89.4541
$\Delta \overline{G}_{Se_5}$ kcal /mol	-115.644	-87.4153	-95.7016	-86.291	-76.8832
$\Delta S_{V_{Cu}}^{vib}$ kcal/mol K	2.091947	-0.30594	-0.03372	0.236311	-0.07621
$\Delta H_{V_{Cu}}^{0}$ kcal/mol	104.683	-35.7108	-17.6919	9.111083	-17.8908
x=0.2					
$\Delta \overline{S}_{Se_5}$ kcal/mol K	2.115393	-0.24095	0.027146	0.291103	-0.01335
$\Delta \overline{H}_{Se_5}$ kcal/mol	516.7643	-172.008	-82.2887	49.69697	-80.7622
$\Delta \overline{G}_{Se_5}$ kcal /mol	-113.94	-85.711	-93.3685	-83.6721	-73.9785
$\Delta S_{V_{Cu}}^{vib}$ kcal/mol K	2.06964	-0.28671	-0.01861	0.245351	-0.0591
$\Delta H_{V_{Cu}}^{0}$ kcal/mol	103.3529	-34.4017	-16.4577	9.939394	-16.1524
x=0.25					
$\Delta \overline{S}_{Se_5}$ kcal/mol K	2.093657	-0.23047	0.03444	0.293681	-0.00452
$\Delta \overline{H}_{Se_5}$ kcal/mol	511.6057	-166.931	-77.5024	52.90941	-74.0203
$\Delta \overline{G}_{Se_5}$ kcal /mol	-112.618	-84.3891	-91.5589	-81.6407	-71.7254
$\Delta S_{V_{Cu}}^{vib}$ kcal/mol K	2.052338	-0.27179	-0.00688	0.252363	-0.04583
$\Delta H_{V_{Cu}}^{0}$ kcal/mol	102.3211	-33.3862	-15.5005	10.58188	-14.8041
x=0.3					
$\Delta \overline{S}_{Se_5}$ kcal/mol K	2.075897	-0.2219	0.040398	0.295788	0.002701
$\Delta \overline{H}_{Se_5}$ kcal/mol	507.3907	-162.783	-73.5916	55.53417	-68.5118
$\Delta \overline{G}_{Se_5}$ kcal /mol	-111.538	-83.309	-90.0802	-79.9809	-69.8845
$\Delta S_{V_{Cu}}^{vib}$ kcal/mol K	2.038201	-0.2596	0.002703	0.258092	-0.03499
$\Delta H_{V_{Cu}}^{0}$ kcal/mol	101.4781	-32.5565	-14.7183	11.10683	-13.7024

Table 4.6 Defect formation enthalpy and vibrational entropy changes for Se_6.

x=0.15	Temperature K				
	298.15	358.15	408.15	458.15	508.15
$\Delta \overline{S}_{Se_6}$ kcal/mol K	2.353528	-0.29912	-0.00013	0.307989	-0.05494
$\Delta \overline{H}_{Se_6}$ kcal/mol	573.1685	-205.161	-108.278	42.55382	-116.801
$\Delta \overline{G}_{Se_6}$ kcal /mol	-128.536	-98.0331	-108.224	-98.5515	-88.882
$\Delta S^{vib}_{v_{Cu}}$ kcal/mol K	2.291766	-0.36088	-0.06189	0.246227	-0.1167
$\Delta H^0_{v_{Cu}}$ kcal/mol	95.52808	-34.1936	-18.0463	7.092303	-19.4668
x=0.2					
$\Delta \overline{S}_{Se_6}$ kcal/mol K	2.319901	-0.28289	0.011153	0.311978	-0.04128
$\Delta \overline{H}_{Se_6}$ kcal/mol	565.1877	-197.307	-100.873	47.52369	-106.371
$\Delta \overline{G}_{Se_6}$ kcal /mol	-126.491	-95.988	-105.425	-95.4089	-85.3963
$\Delta S^{vib}_{v_{Cu}}$ kcal/mol K	2.264999	-0.3378	-0.04375	0.257075	-0.09618
$\Delta H^0_{v_{Cu}}$ kcal/mol	94.19796	-32.8844	-16.8121	7.920615	-17.7285
x=0.25					
$\Delta \overline{S}_{Se_6}$ kcal/mol K	2.293818	-0.27031	0.019904	0.315071	-0.03068
$\Delta \overline{H}_{Se_6}$ kcal/mol	558.9974	-191.214	-95.1293	51.37862	-98.2806
$\Delta \overline{G}_{Se_6}$ kcal /mol	-124.905	-94.4016	-103.253	-92.9712	-82.6927
$\Delta S^{vib}_{v_{Cu}}$ kcal/mol K	2.244236	-0.31989	-0.02968	0.265489	-0.08026
$\Delta H^0_{v_{Cu}}$ kcal/mol	93.16623	-31.869	-15.8549	8.563104	-16.3801
x=0.3					
$\Delta \overline{S}_{Se_6}$ kcal/mol K	2.272507	-0.26003	0.027055	0.317599	-0.02201
$\Delta \overline{H}_{Se_6}$ kcal/mol	553.9395	-186.236	-90.4364	54.52833	-91.6703
$\Delta \overline{G}_{Se_6}$ kcal /mol	-123.608	-93.1055	-101.479	-90.9795	-80.4836
$\Delta S^{vib}_{v_{Cu}}$ kcal/mol K	2.227272	-0.30527	-0.01818	0.272364	-0.06725
$\Delta H^0_{v_{Cu}}$ kcal/mol	92.32325	-31.0393	-15.0727	9.088055	-15.2784

Table 4.7 Defect formation enthalpy and vibrational entropy changes for Se_7.

x=0.15	Temperature K				
	298.15	358.15	408.15	458.15	508.15
$\Delta \bar{S}_{Se_7}$ kcal/mol K	2.892156	-0.36319	-0.00476	0.390852	-0.09032
$\Delta \bar{H}_{Se_7}$ kcal/mol	701.0593	-252.887	-137.47	55.64201	-157.277
$\Delta \bar{G}_{Se_7}$ kcal /mol	-161.237	-122.81	-135.527	-123.427	-111.379
$\Delta S^{vib}_{V_{Cu}}$ kcal/mol K	2.8201	-0.43525	-0.07682	0.318796	-0.16238
$\Delta H^0_{V_{Cu}}$ kcal/mol	100.1513	-36.1266	-19.6386	7.948858	-22.4681
x=0.2					
$\Delta \bar{S}_{Se_7}$ kcal/mol K	2.852925	-0.34426	0.008403	0.395505	-0.07438
$\Delta \bar{H}_{Se_7}$ kcal/mol	691.7485	-243.723	-128.831	61.44018	-145.108
$\Delta \bar{G}_{Se_7}$ kcal /mol	-158.851	-120.424	-132.261	-119.761	-107.312
$\Delta S^{vib}_{V_{Cu}}$ kcal/mol K	2.788872	-0.40832	-0.05565	0.331452	-0.13843
$\Delta H^0_{V_{Cu}}$ kcal/mol	98.82122	-34.8175	-18.4044	8.777168	-20.7298
x=0.25					
$\Delta \bar{S}_{Se_7}$ kcal/mol K	2.822495	-0.32958	0.018613	0.399114	-0.06201
$\Delta \bar{H}_{Se_7}$ kcal/mol	684.5265	-236.614	-122.13	65.93759	-135.67
$\Delta \bar{G}_{Se_7}$ kcal /mol	-157	-118.574	-129.727	-116.917	-104.158
$\Delta S^{vib}_{V_{Cu}}$ kcal/mol K	2.764649	-0.38743	-0.03923	0.341268	-0.11986
$\Delta H^0_{V_{Cu}}$ kcal/mol	97.7895	-33.8021	-17.4472	9.419656	-19.3814
x=0.3					
$\Delta \bar{S}_{Se_7}$ kcal/mol K	2.797631	-0.31759	0.026956	0.402063	-0.05191
$\Delta \bar{H}_{Se_7}$ kcal/mol	678.6256	-230.807	-116.655	69.61226	-127.958
$\Delta \bar{G}_{Se_7}$ kcal /mol	-155.488	-117.061	-127.657	-114.593	-101.58
$\Delta S^{vib}_{V_{Cu}}$ kcal/mol K	2.744857	-0.37037	-0.02582	0.349289	-0.10468
$\Delta H^0_{V_{Cu}}$ kcal/mol	96.94651	-32.9724	-16.665	9.944609	-18.2797

Table 4.8 Defect formation enthalpy and vibrational entropy changes for Se_8.

| x=0.15	Temperature K				
	298.15	**358.15**	**408.15**	**458.15**	**508.15**
$\Delta \overline{S}_{Se_8}$ kcal/mol K	3.551617	-0.48099	-0.04507	0.464158	-0.16918
$\Delta \overline{H}_{Se_8}$ kcal/mol	857.5857	-327.069	-190.909	53.67292	-231.5
$\Delta \overline{G}_{Se_8}$ kcal /mol	-201.329	-154.803	-172.515	-158.981	-145.532
$\Delta S_{V_{Cu}}^{vib}$ kcal/mol K	3.469267	-0.56334	-0.12742	0.381808	-0.25153
$\Delta H_{V_{Cu}}^{0}$ kcal/mol	107.1982	-40.8836	-23.8636	6.709116	-28.9376
x=0.2					
$\Delta \overline{S}_{Se_8}$ kcal/mol K	3.506781	-0.45936	-0.03002	0.469476	-0.15096
$\Delta \overline{H}_{Se_8}$ kcal/mol	846.9448	-316.596	-181.036	60.29941	-217.593
$\Delta \overline{G}_{Se_8}$ kcal /mol	-198.602	-152.076	-168.782	-154.791	-140.884
$\Delta S_{V_{Cu}}^{vib}$ kcal/mol K	3.433577	-0.53256	-0.10323	0.396272	-0.22416
$\Delta H_{V_{Cu}}^{0}$ kcal/mol	105.8681	-39.5745	-22.6295	7.537426	-27.1992
x=0.25					
$\Delta \overline{S}_{Se_8}$ kcal/mol K	3.472003	-0.44258	-0.01835	0.4736	-0.13682
$\Delta \overline{H}_{Se_8}$ kcal/mol	838.6909	-308.472	-173.378	65.43932	-206.806
$\Delta \overline{G}_{Se_8}$ kcal /mol	-196.487	-149.961	-165.887	-151.541	-137.279
$\Delta S_{V_{Cu}}^{vib}$ kcal/mol K	3.405894	-0.50869	-0.08446	0.407491	-0.20293
$\Delta H_{V_{Cu}}^{0}$ kcal/mol	104.8364	-38.559	-21.6722	8.179916	-25.8508
x=0.3					
$\Delta \overline{S}_{Se_8}$ kcal/mol K	3.443588	-0.42888	-0.00882	0.47697	-0.12528
$\Delta \overline{H}_{Se_8}$ kcal/mol	831.9472	-301.835	-167.121	69.63893	-197.993
$\Delta \overline{G}_{Se_8}$ kcal /mol	-194.759	-148.233	-163.521	-148.885	-134.334
$\Delta S_{V_{Cu}}^{vib}$ kcal/mol K	3.383275	-0.48919	-0.06913	0.416657	-0.18559
$\Delta H_{V_{Cu}}^{0}$ kcal/mol	103.9934	-37.7293	-20.8901	8.704866	-24.7491
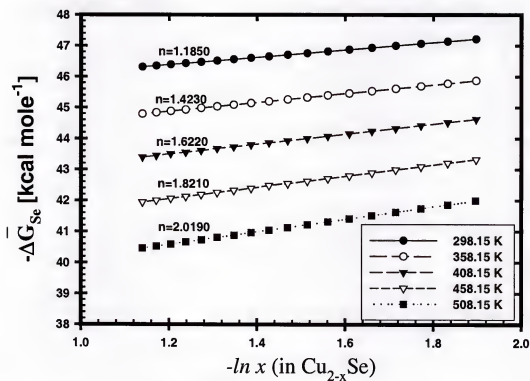
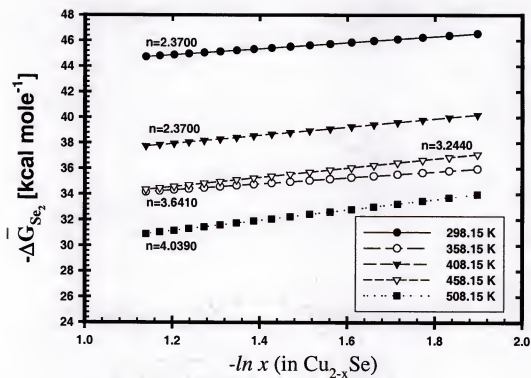Figure 4.9 Relative partial Gibbs energy of Se_1 as a function of defect composition.

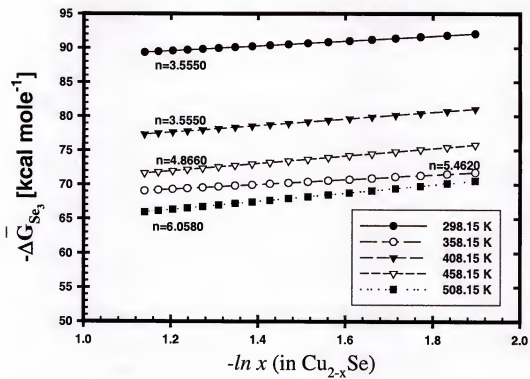Figure 4.10 Relative partial Gibbs energy of Se$_2$ as a function of defect composition.

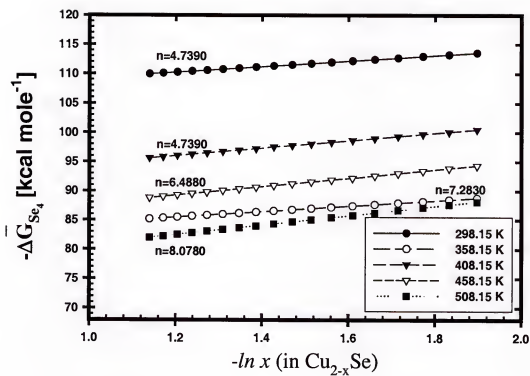Figure 4.11 Relative partial Gibbs energy of Se$_3$ as a function of defect composition.

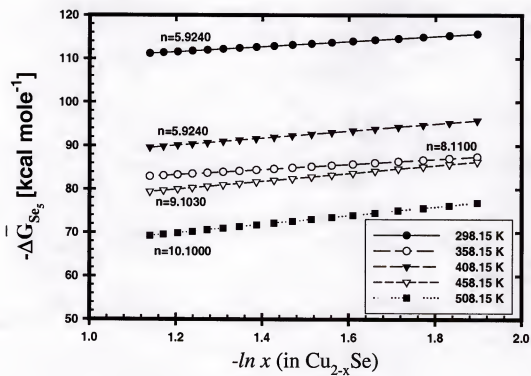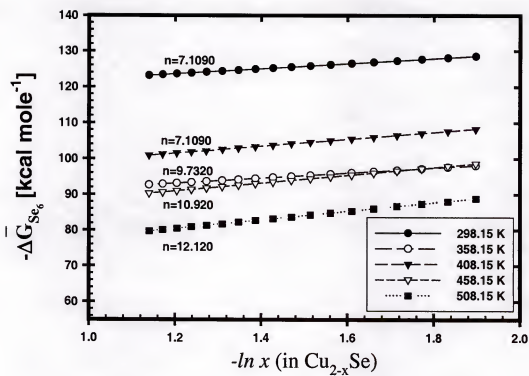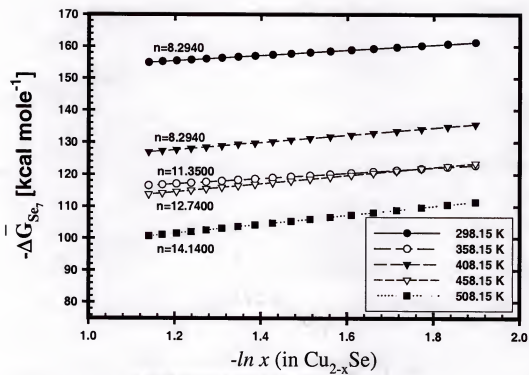Figure 4.12 Relative partial Gibbs energy of Se$_4$ as a function of defect composition.

Figure 4.13 Relative partial Gibbs energy of Se$_5$ as a function of defect composition.

Figure 4.14 Relative partial Gibbs energy of Se₆ as a function of defect composition.

Figure 4.15 Relative partial Gibbs energy of Se₇ as a function of defect composition.
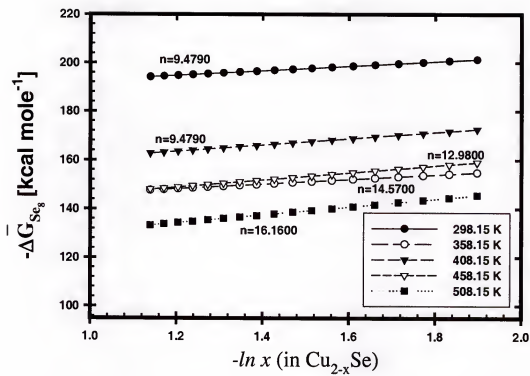
Figure 4.16 Relative partial Gibbs energy of Se_8 as a function of defect composition.
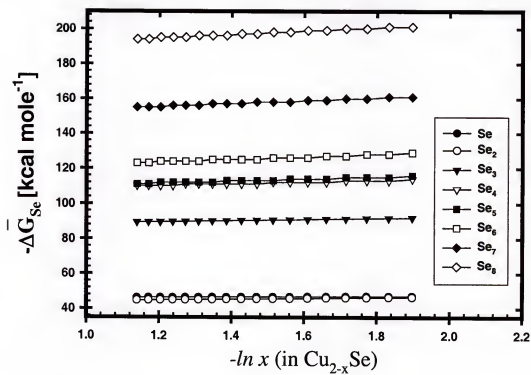
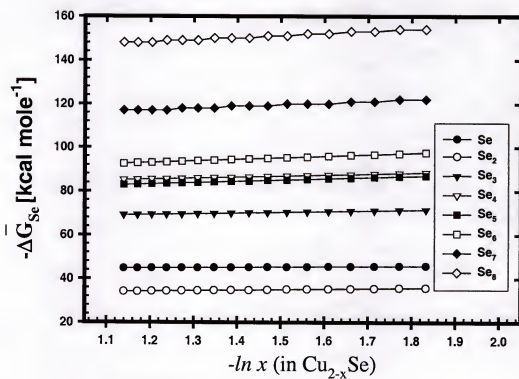Figure 4.17 Relative partial Gibbs energy of selenium species as a function of defect composition at 298K.

Figure 4.18 Relative partial Gibbs energy of selenium species as a function of defect composition at 358K.
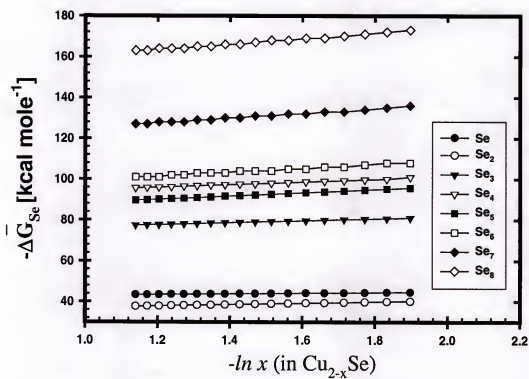
Figure 4.19 Relative partial Gibbs energy of selenium species as a function of defect composition at 408K.
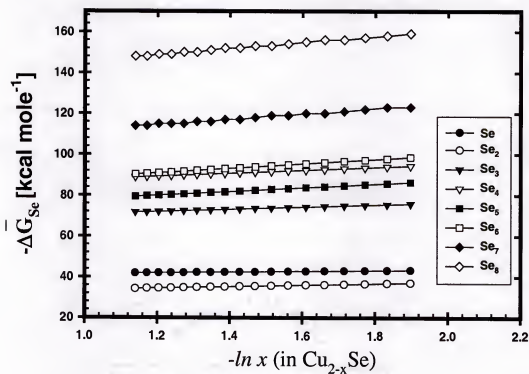
Figure 4.20 Relative partial Gibbs energy of selenium species as a function of defect composition at 458 K.
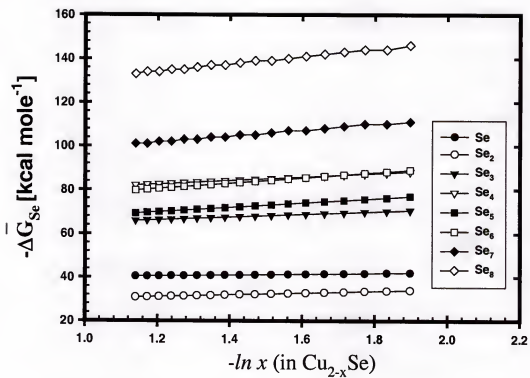
Figure 4.21 Relative partial Gibbs energy of selenium species as a function of defect composition at 508K.

THERMOCHEMISTRY OF THE Cu_2Se-In_2Se_3 SYSTEM BY SOLID ELECTROLYTE
EMF MEASUREMENTS AND PHASE DIAGRAM ASSESSMENT

Introduction

$CuInSe_2$ (CIS) is becoming one of the most promising materials for solar cell
applications. Its band gap (1.04 eV) and good absorption coefficient (10^5 cm^{-1}) for solar
spectrum make this material an excellent candidate for a solar cell absorber layer.
Although the electrical properties of CIS are relatively well-known, a consistent phase
diagram and thermodynamic data assessment is lacking. The knowledge of phase
diagram and thermochemistry of CIS along with its constituent binaries will provide
helpful information on the processing conditions and development of new thin film and
bulk production methods. For the thermodynamic assessment of phase diagram, the phase
stability and Gibbs energy of compounds are essential. According to the recent pseudo-
binary diagram reported by Chang [1], four ternary compounds $CuInSe_2$, $Cu_2In_4Se_7$,
$CuIn_3Se_5$ and $CuIn_5Se_8$ exist in the Cu_2Se-In_2Se_3 section. However; critically assessed G-
H^{SER1} expressions are missing and the stability of the compounds are not experimentally
established. For this reason, the thermochemical data for Cu_2Se-In_2Se_3 pseudo-binary
region was assessed. Solid state galvanic cell experiments were performed to measure
Gibbs energy data of selected ternary compounds and the pseudo-binary phase diagram
was calculated by optimizing the experimental data.

---

[1] SER: Standard Elements Reference State

Literature Review

CuInSe$_2$ has two solid modifications separated by a first order transition between chalcopyrite and sphalerite structures. The δ-CuInSe$_2$ sphalerite phase is stable with a wide homogeneity range between the temperatures of 1090 and 1280K. The low temperature α-CuInSe$_2$ phase crystallizes in the chalcopyrite form with a contracting homogeneity range at low temperature. The melting point $T_m(CuInSe_2)=1254 \pm 5K$ and lattice constants (a=0.577 nm c=1.156 nm) of CuInSe$_2$ were reported by Rigan [48]. Mechkovski [49] also studied the melting and phase transition temperatures. He determined the heats melting of CuInSe$_2$ by DTA experiments as ΔH_{melt}= 83.6 kJ/mol.

Wei [50] stated a first order transition for CuInSe$_2$ and reported the order-disorder transition temperature as T_{tr}= 1125 ± 20 K, which is similar to the experimental value of 1083 K reported by Shay [51] and 1153 K by Fearheiley [52]. He also calculated a ΔH_{tr}(@1125K)=0.10032 kJ/mol for CIS from the difference between ΔH = -1.045 kJ/mol value of the high temperature δ phase and ΔH=-1.1482 kJ/mol value of the low temperature α phase.

Bachmann et al. [53] measured the low temperature CuInSe$_2$ heat capacity by pulsed calorimetry and semi-adiabatic techniques. He derived the entropy value at 298 K as S^0_{298}= 1.5773 kJ/mol K and reported the Debye temperature for CuInSe$_2$. However, his heat capacity data is limited to only low temperature (<300K)

Khriplovich [54] measured the heat capacity of CuIn$_2$Se$_{3.5}$ at low temperatures with a vacuum adiabatic calorimeter. On the other hand, these results were not supported by structural analysis to check whether it was a single phase or two-phase sample.

A number of papers were also published stating the lattice parameters and stability of intermediate phases; however, some results are inconsistent. Range [55] reported the formation of a cubic high-pressure zincblende structure for CuInSe$_2$. Kotkata [56] reported lattice parameters of CuInSe$_2$. The lattice parameters of Cu$_1$In$_3$Se$_5$ were measured by Palatnik [57]. Neuman [58] also reported the lattice parameters for CuInSe$_2$ and CuGaSe$_2$. Fearheiley [59] reported the lattice parameters of CuInSe$_2$ (a=5.814±0.003 ´ and c=11.63±0.04 ´) and compared his results with Hahn`s [60] results which were close (a=5.782 ´ c=11.621 ´). He concluded that the lattice constant of CuInSe$_2$ and non-stoichiometric defect structures vary within its homogeneity range. This suggestion is supported by the fact that a few other authors also observed slightly different lattice parameters within homogeneous single-phase CIS.

Matsuhita [61] determined the melting and transition points of I-III-VI compounds by DTA, including those for CIS. He stated that enthalpies of fusion and transition depend on mean atomic weight and ionicity, that the melting point was influenced by the lattice strain. It was found that fusion and transition enthalpies of their solid solutions are much lower than the end members of their compounds. The reported enthalpy of transformation values are summarized in Table 5.6.

Zargarova [62] constructed the CuInSe$_2$-InSe phase diagram section and reported a transition temperature between α-CuInSe$_2$ and δ-CuInSe$_2$ at 1103 K. Two phase coexistence between CuInSe$_2$ and InSe was observed by micro-structural examination at low temperatures. An event at 1083 K that was attributed to cation ordering was reported. Above 868 K only liquid, L+α-CuInSe$_2$ and L+InSe stability were reported. No other experimental information is available for α,δ-CuInSe$_2$-In$_2$Se$_3$,and α,δ-CuInSe$_2$-In$_4$Se$_3$,

α,δ-CuInSe$_2$-In$_6$Se$_7$. Consequently, the precision of our EMF experiments with cell II and cell III are constrained below 868K on account of these two-phase stability boundaries. Aside from Zargarova`s results, there is not much stability information about Cu$_1$In$_3$Se$_5$-In$_x$Se$_y$ and Cu$_1$In$_5$Se$_8$-In$_x$Se$_y$ (x=1,2,4,6; y=1,3,7) systems.

In general, there is a lack of experimental data on the thermochemistry of CIS and related ternaries except a few estimation calculations. Mooney [63] reported the enthalpy of formation of CuInSe$_2$ and presented enthalpy data of binary associates. The Gibbs energy of formation data was also calculated using approximate equality equation by Lamoreaux et al. [64]. Neumann [65] also reported the heats of atomization for CIS and Nomura [66] analyzed the mechanism of the phase change from Cu$_{2-x}$Se to CuInSe$_2$ by the absorption of indium selenide. A summary of enthalpy and transformation data is given in Tables 5.6 and 5.7.

Seven studies on phase equilibrium in the Cu$_2$Se-In$_2$Se$_3$ pseudo-binary system have been reported. Cu$_5$InSe$_4$, CuInSe$_2$, Cu$_2$In$_4$Se$_7$, CuIn$_3$Se$_5$ and CuIn$_5$Se$_8$ are the most widely referred intermediate compounds. Many other compounds were also stated to exist between chalcopyrite and In$_2$Se$_3$ compositions in the pseudo-binary section. However, X-Ray and structural data are not in good agreement and this region requires further structure studies and justification. There is not much thermodynamic data available on the stability of these ternary phases except the standard enthalpy and absolute entropy of formation, $\Delta H^0_{f,298}$ and S^0_{298} of CuInSe$_2$.

A general review paper was published on production methods of CIS films by Rockett [67]. Production analysis and performance of photovoltaic devices based on CIS materials were discussed. Cahen [68] summarized thermodynamic data available on CIS

related compounds. Gibbs energies of compounds and species that are involved in preparation of CIS films were calculated. A number of possible formation reaction Gibbs energy and free energy function data, as well as formation enthalpy data are available in this paper.

Bachmann [69] published a Cu_2Se-In_2Se_3 pseudo-binary phase diagram. He reported the congruent melting point for Cu_5InSe_4 as T=943 °C with two eutectics at $x_{In_2Se_3}$ =0.11 and $x_{In_2Se_3}$ =0.17. Folmer et al. [70] studied the composition range greater than 50 mol % In_2Se_3 and suggested three new hexagonal phases in high In_2Se_3 region of Cu_2Se-In_2Se_3 pseudobinary.

Fearheiley [71] reviewed the phase relations in the Cu-In-Se system and the crystal growth of single crystals. Cu-In, In-Se and Cu-Se phase diagrams were reported. He also reported the pseudo-binary section of Cu_2Se-In_2Se_3 containing the intermediate compounds $Cu_2In_4Se_7$ [72] $Cu_1In_3Se_5$ [73], $Cu_3In_5Se_9$ [74], Cu_5InSe_4 [69] and $CuIn_5Se_8$ [75]. The pseudo-binary section of Cu-$CuInSe_2$ was reported with a wide range of coexistence up to 900 K. The accuracy limits of Cell I of our EMF experiments was constrained to temperatures below 900 K because the electrochemical cell was made by using excess copper in the test electrode to ensure two phase coexistence.

Fearheiley [71] reported $Cu_2In_4Se_7$ as incongruently melting and $Cu_1In_3Se_5$ as congruent melting compounds. However, Schock [76] did not report a $Cu_2In_4Se_7$ phase despite he reported an incongruent $CuIn_3Se_5$ intermediate. Schock [76] also stated that the solubility of excess Cu in $CuInSe_2$ is very small. He collected phase diagram data from several references and presented the latest data. He reported the existence of incongruently melting $Cu_1In_3Se_5$ phase on the indium rich side, which is also assumed in

this work with slight differences of the stability limits at low temperature. Schock [76] did not make direct suggestion on stability of a $Cu_1In_5Se_8$ compound in the selenium rich side of the pseudo-binary phase section of Cu_2Se-In_2Se_3.

Hanada [77] studied the crystal structure of $CuIn_3Se_5$ by combination of electron and X-Ray diffractions. He determined that $CuIn_3Se_5$ is a stable compound semiconductor, which is different from CIS and not a vacancy ordered compound or a defect chalcopyrite. He measured lattice parameters by XRD at 700 °C as a=0.574 nm and c=1.1518 nm.

Schumann [78] measured diffraction patterns of $CuIn_2Se_{3.5}$ compound. He claimed that $CuIn_2Se_{3.5}$ has a structure type with defects that is a derivative of chalcopyrite. However, the lattice parameters reported by Schumann [78] for $CuIn_2Se_{3.5}$ do not agree with two earlier reports. The fact that the diffraction patterns of 2-4-7 are very similar to CIS with the chalcopyrite structure suggest a possibility that 2-4-7 composition range may lie in a homogeneity range or in a two phase region of 112-135 or 112 and some other composition.

Koneshova [79] constructed a Cu_2Se-In_2Se_3 phase diagram from previously published results and suggested the co-existence of $CuInSe_2$ and $Cu_1In_3Se_5$ phases in the phase diagram. Koneshova [79] also claimed that some of the ternary phases, which were previously assumed to be stable, in fact were two phase regions. Instead of the $Cu_2In_4Se_7$ modification, a stable phase corresponding to the $Cu_1In_3Se_5$ composition was outlined in the phase diagram. Two phase coexistence between the $CuInSe_2$ and $Cu_1In_3Se_5$ modifications was also assumed. On the other hand the limits of high temperature stable modification were greater than other reports and $Cu_1In_3Se_5$ phase was reported to be

stable only below 900 °C. Additionally, a thin range of coexistence between $Cu_1In_3Se_5$ and possibly a compound, which lies in the composition range of CuIn5Se8 compositions, was depicted. However, the limits seem too narrow.

Boehnke [80] emphasized that numerous compounds were stated in the literature to exist along $Cu_2Se-In_2Se_3$ line and the reported data showed evident differences in structure and homogeneity ranges and thermal behavior. Boehnke [80] concluded from X-Ray, EPMA (electron microprobe analysis), optical microscopy and DTA measurements that only 4 ternary phases with extended homogeneity range were stable. He verified δ (sphalerite) phase first time by high temperature X-Ray diffraction. It was asserted that a beta phase extending between $x_{In_2Se_3}$ =0.67 and $x_{In_2Se_3}$ =0.80 crystallizes in an ordered chalcopyrite-like defect structure. From a comparison of X-Ray data with those of literature data for $Cu_2In_4Se_7$, $Cu_1In_3Se_5$, $Cu_8In_{18}Se_{32}$, and $Cu_7In_{19}Se_{32}$, he concluded that all belong to a β ($Cu_1In_3Se_5$) phase. He also reports that the γ ($Cu_1In_5Se_8$) phase has a typical layered structure with hexagonal and trigonal modifications along with strong lattice parameter dependence on compositions. This approach with respect to limits of stabilities of ternary compounds seems reasonable.

Godecke [2] published the most detailed and recent paper about phase diagram of CIS and related binaries. His results are consistent with Boehnke`s [80] results, except the limits of two phase region of high temperature sphalerite phase and β ($Cu_1In_3Se_5$) phase. There is not much known in the high temperature regions of this section. Godecke [2] emphasized that this rather complicated system required a thorough investigation. Godecke`s results were based on experimental studies by differential thermal analysis, light optical microscopy, scanning electron microscopy, transmission electron

microscopy, and X-Ray diffraction. In short, Godecke [2] identified four different ternary phases: α-CuInSe$_2$, γ-CuIn$_5$Se$_8$, δ-CuIn$_3$Se$_5$ and high temperature phase of Cu$_{13}$In$_3$Se$_{11}$. This approach is the same as our conclusion with the exception of the limits of stability of CuIn$_3$Se$_5$ phase and the similar notation will be followed throughout this paper. However, the high temperature phase of Cu$_{13}$In$_3$se$_{11}$ was not considered in our optimization due to lack of Gibbs energy data.

Experimental Procedure

The EMF of 3 different galvanic cells with test electrodes of different composition was measured as a function of temperature. The Gibbs energy of the cell reaction and phase transformation temperature was obtained from the measured open circuit potential of the cells over a temperature range. Based on the coexistence information available in the Cu-In-Se system, the test electrode materials were prepared from the following three samples:

1-- Cu$_2$Se(s) + CuInSe$_2$(α or δ) two phase mixture was prepared by mixing Cu$_2$Se (Johnson Matthey) and In$_2$Se$_3$ (Johnson Matthey) compounds with the mole ratio of

$$\frac{n_{In_2Se_3}}{n_{In_2Se_3} + n_{Cu_2Se}} = 0.3 \qquad \text{Cell I}$$

2-- β-Cu$_1$In$_3$Se$_5$ + CuInSe$_2$(α or δ) two phase mixture was prepared by mixing Cu$_2$Se (Johnson Matthey) and In$_2$Se$_3$ (Johnson Matthey) compounds with the mole ratio of

$$\frac{n_{In_2Se_3}}{n_{In_2Se_3} + n_{Cu_2Se}} = 0.64 \qquad \text{Cell II}$$

3-- β-CuIn₅Se₈(s) + γ-Cu₁In₃Se₅(s) two phase mixture was prepared by mixing Cu₂Se (Johnson Matthey) and In₂Se₃ (Johnson Matthey) compounds with the mole ratio of

$$\frac{n_{In_2Se_3}}{n_{In_2Se_3} + n_{Cu_2Se}} = 0.8 \qquad \text{Cell III}$$

The EMF data for cells I, II, and III were measured over the ranges 949 to1150, 868 to 1179 and 977 to 1145K, respectively. A 15 mass % yittria stabilized zirconia was employed as the solid electrolyte against an In(l)-In₂O₃(s) two phase mixture as the reference electrode. Using literature data for the standard Gibbs energy functions of Cu, In, Cu₂Se, and InSe along with standard Gibbs energy change of appropriate cell reactions, the standard Gibbs energy of reaction for three intermediate compounds in the Cu₂Se-In₂Se₃ section was obtained. An optimized version of the pseudo-binary phase diagram in accordance with measured EMF data is presented.

Cell Materials

Reagent grade Cu₂Se (Johnson Matthey) and In₂Se₃ (Johnson Matthey), Cu powder (Alfa Aesar), In shots (Aldrich) and Se pellets (Atomergic Chemicals) all of which were of 99.99% purity or better were used as the starting materials. Solid mixtures of Cu₂Se and In₂Se₃ in the mole ratios 70:30 for Cell I, 36:64 for Cell II and 20:80 for Cell III were powdered and individually encapsulated in silica ampoules under vacuum of less than 10 Pa. In this procedure, the first silica ampoule was heated in stages at 1333K for 40 hours, 1148K for 70 hours followed by cooling to room temperature. The second and the third ampoules were heated to 1273K for 3 hours and the temperature was then reduced to 923K and annealed for 75 hours, and finally cooled slowly to room temperature. The three ampoules were broken and the solid mixtures were ground in an

agate mortar. All the samples were characterized by X-Ray Diffraction (XRD) method to ensure the desired phases were obtained. The XRD spectra are given in Figures 5.1 to 5.6, while Table 5.1 lists the phases present in the mixture before and after EMF experiments. In powder (Strem Chemicals, mass fraction of In, 0.9999) and In_2O_3 (Johnson Matthey, mass fraction of In_2O_3, 0.9999) were used as received to fabricate reference electrodes.

EMF Measurements

The test electrodes were made by intimately mixing the co-existing phases with one third of their mass of In_2O_3 powder. These mixtures were then allowed to equilibrate within the cell at the lowest temperature of measurement. Before cell I EMF experiments, excess Cu(1Cu + 1cell I sample w/w) was added to test electrode sample to ensure the co-existence stoichiometry of Cu_2Se, Cu and $CuInSe_2$. The reference electrode was made from a mixture of 0.88 In + 0.12 In_2O_3 w/w. The pellet samples were prepared by using a macro/micro 13mm KBr die set (International Crystal Labs). A maximum force of 10 tons was applied on each sample by a hydraulic press.

The EMF measurements were made on the following galvanic cells:

W, In(l), In_2O_3(s) // YSZ // In_2O_3(s), Cu_2Se(s), Cu(s), $CuInSe_2$(α or δ), C, W   Cell I

W, In(l), In_2O_3(s) // YSZ // In_2O_3(s), $Cu_1In_3Se_5$(s), $CuInSe_2$(α or δ), C, W   Cell II

W, In(l), In_2O_3(s) // YSZ // In_2O_3(s), $Cu_1In_5Se_8$(s), $Cu_1In_3Se_5$(s), C, W   Cell III

where YSZ denotes 15 mass percent Y_2O_3 stabilized ZrO_2 (Zirconia) solid electrolyte and W denotes the tungsten wire used as the electrical contact. High density, nuclear grade graphite cups were used to contain the test electrode material. The absence of asymmetric potentials due to the graphite cup was tested by measuring the symmetrical galvanic cell

with identical (In/In_2O_3) electrodes. Nearly null (1mV) EMF was measured in the above symmetric cell over the experimental range 900 to 1200 K. The absence of asymmetric potentials and the location of the electrodes in the isothermal zone of the furnace were carefully verified. A nearly static atmosphere of purified Argon was provided for the electrodes of the cell compartment. The temperature of the cell was measured using a Pt-10%Rh/Pt thermocouple whose junction was located near the electrodes of the cell in the isothermal zone of the furnace. The reversibility of the EMF readings was ascertained by their reproducibility in thermal cycling as well as by micro-polarization. The equilibrium nature of the EMF was verified by a 5 to 10% variation in the composition of the co-existing phases of the test electrodes from one experimental run to another. The test electrodes were examined by XRD at the end of each experiment to confirm the absence of changes in phase composition. Other experimental details such as temperature control, Argon purification system, and voltage measurement are given elsewhere [81]-[83].

Results

Measured open circuit potentials at each measurement temperature for each cell are summarized in Tables 5.3, 5.4 and 5.4 and plotted in Figures 5.7, 5.8 and 5.9. The data were fitted using linear regression analysis and the following expressions resulted:

$$E_{I,a} \pm 1.47 \text{ (mV)} = 343.81 - 0.18828 \text{ T(K)} \quad (949 \text{ to } 1044K) \tag{5.1}$$

$$E_{I,b} \pm 0.45 \text{ (mV)} = 309.26 - 0.15580 \text{ T(K)} \quad (1055 \text{ to } 1150K) \tag{5.2}$$

$$E_{II(a)} \pm 2.14 \text{ (mV)} = -311.49 + 0.38268 \text{ T(K)} \quad (868 \text{ to } 923K) \tag{5.3}$$

$$E_{II(b)} \pm 1.70 \text{ (mV)} = -227.07 + 0.29204 \text{ T(K)} \quad (935 \text{ to } 1045K) \tag{5.4}$$

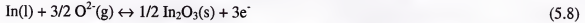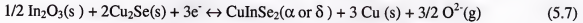$$E_{II(c)} \pm 3.01 \text{ (mV)} = -377.20 + 0.43496 \text{ T(K)} \quad (1054 \text{ to } 1179K) \tag{5.5}$$

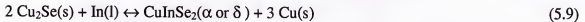$$E_{III} \pm 2.60 \text{ (mV)} = -519.57 + 0.54917 \text{ T(K)} \quad (977 \text{ to } 1145K) \tag{5.6}$$

Discussion

Gibbs Energy of α-CuInSe$_2$ and δ-CuInSe$_2$

The half cell reaction of the cell I can be written as

$$1/2 \ In_2O_3(s) + 2Cu_2Se(s) + 3e^- \leftrightarrow CuInSe_2(\alpha \ or \ \delta) + 3 \ Cu(s) + 3/2 \ O^{2-}(g) \qquad (5.7)$$

$$In(l) + 3/2 \ O^{2-}(g) \leftrightarrow 1/2 \ In_2O_3(s) + 3e^- \qquad (5.8)$$

For the passage of 3 equivalent of electrons, the over-all cell reaction per mole of CIS can be represented as

$$2 \ Cu_2Se(s) + In(l) \leftrightarrow CuInSe_2(\alpha \ or \ \delta) + 3 \ Cu(s) \qquad (5.9)$$

The Gibbs energy change of the overall cell reaction is directly related to the measured EMF by the Nernst equation,

$$\Delta G_R = -nFE \qquad (5.10)$$

where E is the measured open circuit value between test and reference electrodes, n is the number of equivalent charges transferred per mole of reaction and Faraday's constant, F is equal to 96485.3415 C/mol.

Gibbs Energy of Cu$_2$Se, Cu and In

Cu$_{2-x}$Se is a defect compound with a fair homogeneity range. Although the phase diagram and thermochemistry of Cu-Se system were studied before, the literature data is subject to controversy. There is some inconsistency and uncertainty in published data for the Gibbs energy function and enthalpy of formation.

The Cu-Se system was recently assessed by Chang [1]. The α and β Cu$_{2-x}$Se defect phases were described by a 3 sublattice model using the formula(Cu,Va)$_1$ (Se, Va)$_1$ (Cu)$_1$. The other intermediate phases were treated as line compounds. Liquid phase model was taken from Chang [1], which described the liquid phase by the associated model

developed by Sommer [84]. However, the optimized Gibbs energy function of $Cu_{2-x}Se$ is not in good agreement with Barin`s [85] assessment. Although Barin`s [85] recommendation assumes only one solid transformation at 395.4K, the Gibbs energy data display a parabolic character at higher temperature. The reason why there is a distinct bend in the Gibbs energy functions is not clear since Chang`s [1] assessment does not suggest any phase transformation or multi-phase equilibrium between 395.4 and 1300K. However, it may be related to defect formation reactions and the large difference in the entropy function may be responsible for the large deviation in the Gibbs energy function.

Cahen [68] reported a slightly different Gibbs energy of formation data although his Gibbs energy functions are similar to Barin`s [85]. The difference comes from Cahen`s [68] $\Delta H^0_{f,298} = -60.00$ kJ/mol and Barin`s [85] $\Delta H^0_{f,298} = -65.27$ kJ/mol assumptions. Shen [86] recently re-optimized the Cu-Se system. The α-$Cu_{2-x}Se$ and β-$Cu_{2-x}Se$ phases were described by the sublattice model with two Cu sublattices and one Se sublattice represented by the formula $(Cu,Va)_1(Se,Va)_1(Cu)_1$. The liquid phase was described by an ionic sublattice model with two sublattices schematically described as $(Cu^{+1},Cu^{+2})p(Se^{-2},Va^{-1},Se)q$. Shen`s [86] and Cahen`s [68] results in general are consistent, although Shen`s [86] $\Delta H^0_{f,298}$ (-52.46 kJ/mol) slightly differ from Cahen`s [68] (-60.00 kJ/mol). When direct values of Gibbs energies used in calculation, third law analysis showed that Barin`s [85] data introduced a trend of slight temperature dependency. After analyzing all the available data, Shen`s [86] latest assessment results were accepted as a reference since the calculated values are consistent with the other binaries, which are optimized concurrently as a part of ternary Cu-In-Se phase diagram assessment. Interpolated values of Barin`s [85] data were also used when especially

critical data was missing. The Gibbs energy changes for cell reactions were calculated by using both Gibbs energy of formation of compounds and Gibbs energy functions to check the consistency of reference data. The data for elements Cu(s) and In(l) were obtained from Barin [85], Cahen [68] and Shen`s [86] ThermoCalc files and the results from direct Gibbs energy calculations were compared for consistency.

First order transition between α-CuInSe$_2$ and δ-CuInSe$_2$

The Gibbs energy of the CuInSe$_2$ compound can be easily calculated from the following relations,

$$\Delta G_{R\,(\alpha\,or\,\delta)} = G_{CuInSe_2} + 3G_{Cu} - 2G_{Cu_2Se} - G_{In} \tag{5.11}$$

$$\Delta G_{R\,(\alpha\,or\,\delta)} = \Delta G°_f\, CuInSe_2\,(\alpha\,or\,\delta) - 2\,\Delta G°_f\, Cu_2Se\,(s) \tag{5.12}$$

Expressions for the standard Gibbs energy changes $\Delta G_{R(\alpha)}$ and $\Delta G_{R(\delta)}$ for the reaction were calculated using Equations 5.1, 5.2 and 5 10.

$$\Delta G_{R,\alpha} = 0.0545\,T(K) - 99.52 \qquad kJ/mol \tag{5.13}$$

$$\Delta G_{R,\delta} = 0.0451\,T(K) - 89.52 \qquad kJ/mol \tag{5.14}$$

Equations (5.13) and (5.14) are valid for the α (Chalcopyrite) and δ (Sphalerite) phases of CuInSe$_2$ in the temperature ranges indicated in equations (5.1) and (5.2). Since there is no phase transition in Cu$_2$Se, In and Cu in the temperature range 949-1150 K, the difference in ΔG_R calculated from equations (5.13) and (5.14) must correspond to the standard Gibbs energy change $\Delta G_{R\,(\alpha-\delta)}$ for the α- to δ- transition in CuInSe$_2$. Thus, by solving Equations (5.13) and (5.14), one obtains

$$\Delta G_{R(\alpha-\delta)}(kJ/mol) = 10.0 - 0.0094\,T(K) \tag{5.15}$$

Since the Gibbs energy change is zero for the equilibrium, α-δ transformation temperature of $1064(\pm20)$K is obtained by solving Equation 5.15. This value is shown in Figure 5.11. Correspondingly, the standard enthalpy of transition, ΔH°_{trans} is found as 10.0 kJ/mol and the standard entropy of transformation, ΔS°_{trans}, is found as 9.4 J/mol K.

Similarly the Gibbs energy functions of α and δ CuInSe$_2$ are found as:

$$G_{\alpha-CuInSe_2} = -0.2813 \, T(K) - 142.32 \text{ kJ/mol} \tag{5.16}$$

$$G_{\delta-CuInSe_2} = -0.2899 \, T(K) - 133.23 \text{ kJ/mol} \tag{5.17}$$

The following Gibbs energy expressions for Cu(s), In(l) and Cu$_2$Se(s) are used:

$$G_{Cu} = -0.06195T + 15.747 \qquad \text{kJ/mol (fit 800-1100K)} \tag{5.18}$$

$$G_{In} = -0.09719T + 20.546 \qquad \text{kJ/mol (fit 800-1100K)} \tag{5.19}$$

$$G_{\beta-Cu_2Se} = -0.212215T - 8.050 \qquad \text{kJ/mol (fit 800-1100K)} \tag{5.20}$$

All the Gibbs energy expressions are given relative to reference state of 298 K at which the Gibbs formation energies of pure elements were taken as zero. The expressions for pure elements were interpolated from the curve fit expressions of tabulated values of Barin [36] in the temperature range of experimental measurements (800-1100K) The Gibbs energy function of Cu$_2$Se(solid) was taken from the latest assessment results by Shen [86]. The Gibbs energy formation of Cu$_2$Se(solid) was obtained from formation reaction from elements. From this value, the Gibbs energy of formation of CuInSe$_2$ compound was calculated by using Equation (5.12) The calculated Gibbs energy of formation functions can be represented as:

$$\Delta G^\circ_f \text{ Cu}_2\text{Se (s)} = -0.0053T(K) - 59.265 \qquad \text{kJ/mol} \tag{5.21}$$

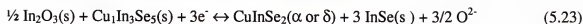$$\Delta G^\circ_f \text{ CuInSe}_2 \ (\alpha) = 0.0439T(K) - 218.05 \qquad \text{kJ/mol} \tag{5.22}$$

The Gibbs energy of α-CuInSe₂, δ-CuInSe₂, enthalpy of transformation and $\Delta H^0_{f,298}$ data are compared in Tables 5.6 and 5.7.

Gibbs energy change for the reaction of cell II

According to the phase equilibrium information available prior to designing Cell II, the test electrode mixture of $Cu_1In_5Se_8(s)/CuInSe_2(s)/In_2O_3(s)$ should correspond to a two-phase mixture between α or δ CIS and a phase labeled β in Figure 5.11. From a recent phase diagram assessment and the analysis of the before and after EMF experiment XRD spectra, it was concluded that there is no stable compound corresponding to $Cu_2In_4Se_7$ composition at low temperature. It is suggested that % 64 mole In_2Se_3 composition correspond to the two phase region between α-$CuInSe_2$ and β-$Cu_1In_3Se_5$ compounds. Hence, β-$Cu_1In_3Se_5$ compound is a solid solution with a wide homogeneity range between % 67 and % 79 mole In_2Se_3 compositions in the pseudo-binary section of the Cu_2Se-In_2Se_3 system. There is no experimental information in the literature involving equilibrium between $Cu_1In_3Se_5$-In_xSe_y and $Cu_1In_5Se_8$-In_xSe_y compounds. However, Zargarova [62] reported the phase diagram of $CuInSe_2$-$InSe$ system based on micro-structural examination. Since there is no other information Zargarova`s [62] results are the best approximations for $Cu_1In_3Se_5$-In_xSe_y and $Cu_1In_5Se_8$-In_xSe_y compounds as well. Due to this assumption, the two phase equilibrium for cell II is limited below 868 K and The EMF results of Cell II may not be directly related to Gibbs energy of $Cu_1In_3Se_5$ compound above 868 K. This fact permits only a small working temperature window for cell II in terms of electrochemical reactions.

The half cell reaction of the cell II could be written as

$$\frac{1}{2} In_2O_3(s) + Cu_1In_3Se_5(s) + 3e^- \leftrightarrow CuInSe_2(\alpha \text{ or } \delta) + 3 InSe(s) + \frac{3}{2} O^{2-} \qquad (5.23)$$

$$In(l) + \frac{3}{2} O^{2-}(g) \leftrightarrow \frac{1}{2} In_2O_3(s) + 3e^- \qquad (5.24)$$

For one mole of $CuInSe_2$, the overall cell reaction can be represented as

$$In(l) + Cu_1In_3Se_5 (s) \leftrightarrow CuInSe_2(\alpha \text{ or } \delta) + 3 InSe \qquad (5.25)$$
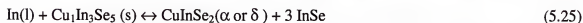
As in the case of cell I, by solving the EMF expressions (5.4) and (5.5) for the passage of 3 faraday of electricity, one obtains the free energy change, $\Delta G_{R(\alpha-\delta)}$ of $CuInSe_2$.

$$(\Delta G_{R(\alpha-\delta)} \text{ (kJ/mol)} = 21.73 - 0.02069 \text{ T(K)} \qquad (5.26)$$

The expression (5.26) yields a value of $1050\pm20K$ and 21.7 $kJ.mol^{-1}$ for T_{trans} and ΔH°_{trans} for $CuInSe_2$, which are in good agreement with the data obtained from the cell I and the literature phase diagram data. The T_{trans} of 1064 and 1050K obtained from cells II and I are in good agreement with 1083K reported by Palatnik and Rogacheva [87], Mechkovski et al. [49] and by Shay et al [51]. Bodnar and Korzun [88] carried out DTA experiments and found that the phase transition occurs in a certain temperature range instead of at constant temperature, which usually occurs in first order transitions. Wei et al [50] calculated this phase transition temperature by Monte Carlo Simulation method to be 1125K with a uncertainty of $\pm20K$ and enthalpy of transition, ΔH°_{trans} to be 10.0 kJ/mol. This enthalpy of transformation value is smaller than the measured Differential Thermal Analysis value of 15.88 [89] although it is in excellent agreement with 10.00 $kJ.mol^{-1}$ by the present EMF results. These values are compared in Table 5.6.
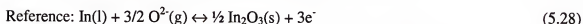
Standard Gibbs energy data on Cu₁In₃Se₅(s)

The EMF expression (5.3) corresponding to the over-all galvanic cell reaction (5.25) can be represented for the passage of 3 faraday of electricity as

$$\Delta G_R \text{ (kJ/mol)} = 90.16 - 0.11077 \text{ T(K)} \tag{5.27}$$

The above equation can be combined with expressions for ΔG°_f of InSe and CuInSe₂ to yield the ΔG°_f of Cu₁In₃Se₅. However, the EMF of cell II is applicable only below 868K. In addition, a significant instability in open circuit voltages was observed at higher temperature, which selenium loss due to high vapor pressure appeared during the experiments at higher temperatures. In addition, the uncertainty of the phase equilibrium between Cu₁In₃Se₅ and In$_x$Se$_y$ compounds does not allow to make a firm judgment on the accuracy of measured EMF data. However, the transformation temperatures from the slope change of open circuit data can still be a used as an indication of possible phase transformations. These data are depicted in Figure 5.11.

Stability of Cu₁In₅Se₈

The half cell reactions of the cell III can be written as

$$\text{Reference: In(l)} + 3/2 \text{ O}^{2-}\text{(g)} \leftrightarrow \frac{1}{2} \text{ In}_2\text{O}_3\text{(s)} + 3\text{e}^- \tag{5.28}$$

$$\text{Test: 3e}^- + \text{CuIn}_5\text{Se}_8\text{(s)} + \frac{1}{2} \text{ In}_2\text{O}_3\text{(s)} \leftrightarrow \text{Cu}_1\text{In}_3\text{Se}_5\text{(s)} + 3/2 \text{ O}^{2-}\text{(g)} + 3 \text{ InSe(s)} \tag{5.29}$$

The EMF results in Equation (5.6) (cell III) for the passage of 3 faraday of electricity can be written for the following overall cell reaction,

$$\text{In(l)} + \text{CuIn}_5\text{Se}_8\text{(s)} \leftrightarrow \text{Cu}_1\text{In}_3\text{Se}_5\text{(s)} + 3 \text{ InSe(s)} \tag{5.30}$$

$$\Delta G_R \text{ (kJ.mol}^{-1}) = 150.40 - 0.15896 \text{ T(K)} \tag{5.31}$$

Hypothetically, the Gibbs energy data calculated from cell II results for Cu₁In₃Se₅ compound can be used to obtain Gibbs energy expression of Cu₁In₅Se₈ compound.

However, experimental problems such as high selenium vapor loss during the experiments and uncertainty of Gibbs energy and stability data of $Cu_1In_3Se_5$ compound suggest that a meaningful analysis is not likely.

The following data for $\Delta G°_f$ of $CuIn_3Se_5$ (β phase) was estimated using the calculated values of $\Delta H°_{f,298}$ of Wei et al [90] and $S°_{298}$ by Chang et al. [91] neglecting the ΔC_P terms.

$$\Delta G°_f \; CuIn_3Se_5(s) \; (kJ/mol) = -472.90 - 0.06220 \; T(K) \qquad (5.32)$$

By combining Equations. (5.31), (5.32) and $\Delta G°_f$ (InSe, l) from the literature from Mallika et al. [92] ($\Delta G°_f$ (InSe,s) $\pm$ 1.24) (kJ/mol)=-144.82 + 0.06045 T(K), the standard Gibbs energy of formation of $CuIn_5Se_8$ was derived and is given as follows:

$$\Delta G°_f \; CuIn_5Se_8(s) \; (kJ/mol) = -1086.56 + 0.31051 \; T(K) \qquad (5.33)$$

Computation of $\Delta H°_{f,298}$ of $CuInSe_2(\alpha)$, $Cu_1In_3Se_5(s)$, $Cu_1In_5Se_8(s)$

To assess the temperature dependent errors in the EMF measurements on cell I and their consistency with the calorimetric data, a the third-law analysis was conducted. For this purpose, Gibbs energy expressions for Cu, In, Cu_2Se and $CuInSe_2$ from Cahen [93] and Shen [86] were combined with the ΔG_R values calculated from each EMF value along with $\Delta G°_f$ of Cu_2Se at each experimental temperature in order to derive those for $\Delta H°_{f,298}$ at different temperatures. A third-law plot of $\Delta H°_{f,298}$ $CuInSe_2$ is shown in Figure 5.10. The mean value of $\Delta H°_{f,298}$ $CuInSe_2$ was found to be -202.92 kJ/mol. This value is compared with those of other literature values along with $S°_{298}$ in Table 5.7.

Due to the lack of reliable data for the free energy functions for the $Cu_1In_3Se_5$ and $Cu_1In_5Se_8$ phases, no third-law analysis was performed. However, the pseudo-binary phase diagram of Cu_2Se and In_2Se_3 system was critically optimized and all compound

Gibbs energy data were calculated in accordance with published phase diagram data. The CALPHAD method of phase diagram calculation was used in the optimization with the help of ThermoCalc computer program. The estimated and calculated data are compared in Tables 5.6, 5.7, and 5.8.

Pseudo-binary Phase Diagram Assessment of the Cu_2Se-In_2Se_3 System

Summary

The Cu_2Se-In_2Se_3 pseudo-binary diagram is one of the most studied sections of the Cu-In-Se system. Although this pseudo-binary was evaluated a number of times and many provisional phase diagrams were suggested, there is still some inconsistency especially in the $CuInSe_2$-In_2Se_3 section of the phase diagram. The difficulty in interpreting the crystal structure data, which displays compositional dependency in non-homogeneous structure regions, is responsible for most of the confusion. The performance of a critical assessment should be helpful in interpreting the phase diagram data.

The ternary compounds in the Cu-In-Se system are of great importance especially for the photovoltaic applications. In this assessment, the Cu_2Se-In_2Se_3 system is characterized by the occurrence of three stable ternary compounds with wide homogeneity ranges: $CuInSe_2$, $Cu_1In_3Se_5$ and $Cu_1In_3Se_5$. $CuInSe_2$ can be described with two polymorphs: the chalcopyrite α-$CuInSe_2$ and the high temperature modification of δ-$CuInSe_2$ with the sphalerite structure, while the β-phase can be represented with the numerical formula $Cu_1In_3Se_5$, which can be described as an ordered defect structure. The γ phase, represented by the numerical formula $Cu_1In_5Se_8$, can be described by a non-homogenous layered structure. The liquid phase does not exhibit miscibility gaps;

however; there are 2 eutectic (17 mol% In_2Se_3, 95 mol% In_2Se_3) and 2 peritectic reactions (73 and 84.5 mol% In_2Se_3) in the pseudo-binary section of Cu_2Se-In_2Se_3 system.

In the present investigation, the EMF experiments on 30 mol% for the cell I, 64 mol% for cell II and 80 mol% In_2Se_3 for the cell III were carried out and the temperature of phase transformation of $CuInSe_2$ from the ordered chalcopyrite to sphalerite structure was observed over the range 1000-1100 K. The measured temperatures are marked on the evaluated pseudo-binary section of Cu_2Se-In_2Se_3 diagram as shown in Figure 5.11. It was also observed that the EMF readings were sporadic beyond 1150 K (cell I), 1180 K (cell II) and 1145 K (cell III), which indicated some phase change or co-existence phases going to liquidus range. These temperatures are also marked on the same section of the phase diagram. By combining XRD measurements, phase transition temperature and standard enthalpy data from the literature along with the measured Gibbs energy functions measured in this work, the critical construction of partial isothermal section of the Cu-In-Se phase diagram was performed. Furthermore, a critical assessment of this pseudo-binary system and an optimization of selected data were performed based on the measured and evaluated phase diagram and the reported thermodynamic data. Various models, including the Redlich-Kister polynomial [94] with two coefficients, sub-regular model, and sub-lattice models [95],[96], were used to describe the solution phases in this system. A self-consistent set of phase diagram and thermodynamic data was obtained through this assessment.

Thermodynamic Models

Pure Elements and Stoichiometric Compound Phases

The Gibbs energy functions for Cu_2Se were taken from Shen [86], and the recent assessment of Chang [1] for In_2Se_3. The Cu_2Se compound was reported with two modifications, α-$Cu_{2-x}Se$ and β-$Cu_{2-x}Se$ in Shen`s [86] recent re-optimization study. The α-$Cu_{2-x}Se$ and β-$Cu_{2-x}Se$ phases were described by the sublattice model with two Cu sublattices and one Se sublattice represented by the formula $(Cu,Va)_1(Se,Va)_1(Cu)_1$. These optimized functions were adopted and the values for the stoichiometric compositions were directly used in this assessment.

The In-Se system was recently assessed by Chang [1] with nine intermediate phases including four stable phases corresponding to In_2Se_3 compositions. The α-In_2Se_3, β-In_2Se_3, γ-In_2Se_3, and δ-In_2Se_3 phases were modeled as line compounds; however; only the γ-In_2Se_3 and δ-In_2Se_3 phases were included in this assessment.

The three-term equation given below was used to represent the temperature dependence of the Gibbs energies of the end members,

$$°G = a+bT+cTlnT \tag{5.34}$$

where $°G$ is the standard Gibbs energy, T is the absolute temperature, and a, b and c are constants whose values are estimated from optimization of experimental data.

Liquid Phase

With a view towards predicting higher order systems, a simplified model for the liquid is preferred such as the Redlich-Kister [94] expansion. The general formula for the liquid solution can be represented as

$$G^l = {}^{ref}G^l + {}^{id}G^l + {}^EG^l \tag{5.35}$$

with

$$^{ref}G^l = y_{Cu_2Se}\,^{\circ}G^l_{Cu_2Se} + y_{In_2Se_3}\,^{\circ}G^l_{In_2Se_3} \tag{5.36}$$

$$^{id}G^l = RT(y_{Cu_2Se}\ln y_{Cu_2Se} + y_{In_2Se_3}\ln y_{In_2Se_3}) \tag{5.37}$$

where y_i refers to the fraction of species i in liquid phase. The terms $^{\circ}G^l_i$ represent the Gibbs energies of the pure liquid phase of species i.

$^EG^l$, the excess Gibbs energy, can be expressed by the following regular solution model,

$$^EG^l = x_{Cu_2Se}x_{In_2Se_3}\sum_{i=0}^{2}{}^{i}L^l_{Cu_2Se,In_2Se_3}\left(x_{Cu_2Se} - x_{In_2Se_3}\right)^i \tag{5.38}$$

where L is the binary interaction parameter to be optimized in the present work. The temperature dependence of L may be represented as

$$^{i}L^l_{Cu_2Se,In_2Se_3} = a_i + b_i T \tag{5.39}$$

Ordered Non-stoichiometric Compound Phases

β-$Cu_1In_3Se_5$ and γ-$Cu_1In_5Se_8$ phases can be represented by the sub-regular model, which is a modified version of the general Redlich-Kister model [94] with 2 coefficients. The general representation of the Gibbs energy of β and γ phases is the same as equation (5.35), where l is replaced with β or γ

For β and γ phases, the reference terms can be represented as

$$^{ref}G^\beta = x_{Cu_2Se}\,^{\circ}G^\beta_{Cu_2Se} + x_{In_2Se_3}\,^{\circ}G^\beta_{In_2Se_3} \tag{5.40}$$

$$^{ref}G^\gamma = x_{Cu_2Se}\,^{\circ}G^\gamma_{Cu_2Se} + x_{In_2Se_3}\,^{\circ}G^\gamma_{In_2Se_3} \tag{5.41}$$

and the ideal terms can be expressed with the following expressions,

$$^{id}G^\beta = RT(x_{Cu_2Se} \ln x_{Cu_2Se} + x_{In_2Se_3} \ln x_{In_2Se_3}) \tag{5.42}$$

$$^{id}G^\gamma = RT(x_{Cu_2Se} \ln x_{Cu_2Se} + x_{In_2Se_3} \ln x_{In_2Se_3}) \tag{5.43}$$

Similarly the excess terms are given by the following relation,

$$^{E}G^\beta = x_{Cu_2Se} x_{In_2Se_3} \sum_{i=0}^{1} {}^{i}L^{I}_{Cu_2Se,In_2Se_3} \left(x_{Cu_2Se} - x_{In_2Se_3} \right)^i \tag{5.44}$$

$$^{E}G^\gamma = x_{Cu_2Se} x_{In_2Se_3} \sum_{i=0}^{1} {}^{i}L^{I}_{Cu_2Se,In_2Se_3} \left(x_{Cu_2Se} - x_{In_2Se_3} \right)^i \tag{5.45}$$

where x_i refers to the fraction of species i in β or γ phase. The terms $^{\circ}G_i^l$ represent the Gibbs energies of the pure solid phase of species i, and L is the binary interaction parameter to be optimized in the present work. The temperature dependence of L may be represented as

$$^{i}L^{\beta}_{Cu_2Se,In_2Se_3} = a_i + b_i T \tag{5.46}$$

$$^{i}L^{\gamma}_{Cu_2Se,In_2Se_3} = a_i + b_i T \tag{5.47}$$

The high temperature modification δ-CuInSe$_2$ sphalerite and α-CuInSe$_2$ chalcopyrite phase can be described using the sublattice model developed by [97], [98] with the following formula:

$$(Cu_2Se, In_2Se_3)_1(In_2Se_3, Cu_2Se)_1 \tag{5.48}$$

To model the homogeneity range, the ordered non-stoichiometric α-CuInSe$_2$ and δ-CuInSe$_2$ phases are described using a three-sublattice formalism. The Gibbs energy of such a phase ϕ(ϕ=α-CuInSe$_2$ or δ-CuInSe$_2$) can be represented by Equation (5.35), where l is replaced by ϕ, as:

$$^{ref}G^{\phi} = y'_{Cu_2Se}\, y''_{In_2Se_3}\, {}^{\circ}G^{\phi}_{Cu_2Se:In_2Se_3} + y'_{Cu_2Se}\, y''_{Cu_2Se}\, {}^{\circ}G^{\phi}_{Cu_2Se:Cu_2Se}$$

$$+ y'_{In_2Se_3}\, y''_{In_2Se_3}\, {}^{\circ}G^{\phi}_{In_2Se_3:In_2Se_3} + y'_{In_2Se_3}\, y''_{Cu_2Se}\, {}^{\circ}G^{\phi}_{In_2Se_3:Cu_2Se} \tag{5.49}$$

$$^{id}G^{\phi} = RT\, [\, p(y'_{Cu_2Se} \ln y'_{Cu_2Se} + y'_{In_2Se_3} \ln y'_{In_2Se_3})$$

$$+ q(y''_{In_2Se_3} \ln y''_{In_2Se_3} + y''_{Cu_2Se} \ln y''_{Cu_2Se})\,] \tag{5.50}$$

and the excess function is given by

$$^{E}G^{\phi} = y'_{Cu_2Se} y'_{In_2Se_3} (y''_{Cu_2Se} L_{Cu_2Se,In_2Se_3:Cu_2Se} + y''_{In_2Se_3} L_{Cu_2Se,In_2Se_3:In_2Se_3})$$

$$+ y''_{In_2Se_3} y''_{Cu_2Se} (y'_{In_2Se_3} L_{In_2Se_3:In_2Se_3,Cu_2Se} + y'_{Cu_2Se} L_{Cu_2Se:In_2Se_3,Cu_2Se}) \tag{5.51}$$

In these expressions y'_i and y''_i refer to the site fractions of the species i on the first and second sublattices, respectively. The standard Gibbs energy of stoichiometric α-CuInSe$_2$ terms ${}^{\circ}G^{\phi}_{Cu_2Se:In_2Se_3}$ and ${}^{\circ}G^{\phi}_{In_2Se_3:Cu_2Se}$ with the parameters estimated in this study are modeled according to following relations,

$$^{\circ}G^{\phi}_{Cu_2Se:In_2Se_3} = 0.5\,{}^{\circ}G_{\beta - Cu_2Se} + 0.5\,{}^{\circ}G_{\delta - In_2Se_3} + a_1 + b_1 T \tag{5.52}$$

$$^{\circ}G^{\phi}_{In_2Se_3:Cu_2Se} = 0.5\,{}^{\circ}G_{\delta - In_2Se_3} + 0.5\,{}^{\circ}G_{\beta - Cu_2Se} + a_1 + b_1 T \tag{5.53}$$

The Gibbs energies for the other two terms in the equation (5.49) are expressed as

$$^{\circ}G^{\phi}_{Cu_2Se:Cu_2Se} = {}^{\circ}G_{\beta - Cu_2Se} + a_1 + b_1 T \tag{5.54}$$

$$^{\circ}G^{\phi}_{In_2Se_3:In_2Se_3} = {}^{\circ}G_{\delta - In_2Se_3} + a_1 + b_1 T \tag{5.55}$$

where, ${}^{\circ}G_{\beta - Cu_2Se}$ and ${}^{\circ}G_{\delta - In_2Se_3}$ are the standard Gibbs energy of stoichiometric β-Cu$_2$Se and δ-In$_2$Se$_3$ phases. The a_i and b_i are model parameters to be optimized.

Optimization Procedure

A selected set of thermodynamic and phase diagram data and our EMF experimental data were used for the optimization of thermodynamic model parameters of the Cu_2Se-In_2Se_3 system. The optimization was performed by using the PARROT module of the Thermo-Calc program package. First, the calculated and estimated values of Gibbs energy of known compounds were entered. Then by reviewing the latest phase diagram data, single phase and two phase boundary limits are outlined and unknown Gibbs energy functions were estimated from enthalpy of formation, standard entropy, heat capacity, transition enthalpy and temperature, and melting information. Third, fixing the calculated Gibbs energy data of α-$CuInSe_2$ from EMF experiments, the coefficients of ordered non-stoichiometric phases were roughly estimated. Fourth, after obtaining estimated parameters α-$CuInSe_2$, δ-$CuInSe_2$, β-$Cu_1In_3Se_5$ and γ-$Cu_1In_5Se_8$ phase solution parameters were also calculated. Finally all the calculated and optimized parameters were optimized based on the available thermodynamic and phase diagram data.

Results and Discussion

The optimized parameters of the stable phases in the Cu_2Se-In_2Se_3 system are listed in Table 5.8. The phase diagram and thermodynamic properties of this system were calculated with the Poly-3 module of the ThermoCalc program package. The calculated phase diagram is given in Figure 5.13. Table 5.9 displays the experimental and calculated temperatures and compositions of the invariant reactions in the system. The calculated values are well within the uncertainty of experimental data. The high temperature phase of δ-$CuInSe_2$ phase limits are well defined and the stability ranges of β-$Cu_1In_3Se_5$ and γ-$Cu_1In_5Se_8$ phases seem to be consistent with the experimental data published in this

region. Figure 5.15 reveals the more complicated region of the phase diagram where there were no consistent explanation of numerous and conflicting data. This region appears with two peritectic reactions involving δ-liquid, β-liquid and γ-liquid coexistence regions at high temperature. The eutectic at around 1150 K is also clearly represented.

The assessed and calculated standard enthalpies of formation of the intermediate compounds at 298K are presented in Table 5.7. Although there is broad inconsistency in the literature, these optimization results are within the reported limits.

Conclusion

A thermodynamic description of the Cu_2Se-In_2Se_3 was obtained by optimization of the available phase equilibrium and thermodynamic information along with the direct results of EMF experiments. The Redlich-Kister model with 3 coefficient expression was employed to define the Gibbs energy of the liquid phase. The intermediate phases of β-$Cu_1In_3Se_5$ and γ-$Cu_1In_5Se_8$ were modeled with 2 coefficient expansion of the Redlich-Kister model. The α and δ modification of $CuInSe_2$ phases were modeled with a specific sublattice model. A reasonable agreement between the model calculated values and the thermodynamic phase equilibrium data was achieved. Importantly, a conclusion for the conflicting phase stability regions of β-$Cu_1In_3Se_5$ and γ-$Cu_1In_5Se_8$ phases along with the high temperature homogeneity limits of δ-$CuInSe_2$ sphalerite formation was described. The calculated phase diagram can further be improved with a study towards confirmation of beta and gamma phase Gibbs energy functions. Also, the less studied Cu_5InSe_4 high temperature stable compound can be included when necessary Gibbs energy data become available.

Table 5.1. Comparison of the structure analysis by X-Ray powder diffractograms taken from samples $(Cu_2Se)_{1-x}$ $(In_2Se_3)_x$ with x=0.3 (cell I), 0.64 (cell II), and 0.8 (cell III) (at.%) using Phillips 3720 X-Ray Diffractometer.

Composition mol % In_2Se_3	Phases	
	Before The Experiment	After the experiment
30	α-$CuInSe_2$-Cu_2Se	α-$CuInSe_2$-Cu_2Se + In_2O_3
64	$CuInSe_2$ – $Cu_2In_4Se_7$ [78], In_4Se_3, InSe	$CuInSe_2$ – $Cu_2In_4Se_7$ [78], In_2O_3, InSe
80	β-$Cu_1In_3Se_5$ -γ-$Cu_1In_5Se_8$ [70], In_4Se_3 or InSe, Cu_2Se trace or Se(s)	β-$Cu_1In_3Se_5$ -γ-$Cu_1In_5Se_8$ [70], In_4Se_3 or InSe, Cu_2Se trace, $In_2O_3(s)$

Table 5.2. Lattice structures of the compounds in the Cu-In-Se System.

Compound	Crystal System	Lattice Parameter	Reference
$CuInSe_2$ (α)	Tetragonal	$a_o = 0.5785$ nm $C_o = 1.157$ nm	[60]
		$a_o = 0.5782$ nm $C_o = 1.1621$ nm	[49]
		$a_o = 0.5780$ nm $C_o = 1.161$ nm	[56]
		$a_o = 0.577$ nm $C_o = 1.156$ nm	[48]
		$a_o = 0.5781$ nm $C_o = 0.1164$ nm	[58]
		$a_o = 0.5814$ nm $C_o = 0.1163$ nm	[59]
		$a_o = 0.5785$ nm $C_o = 1.1621$ nm $x_{Cu}=0.258$, $x_{In}=0.249$, $x_{Se}=0.493$	[80]

		$a_o = 0.5780$ nm $C_o = 1.161$ nm $x_{Cu}=0.221$, $x_{In}=0.27$, $x_{Se}=0.509$	[80]
CuInSe$_2$ (δ)	Cubic	$a_o = 0.586$ nm $C_o = 0.558$ nm	[55]
		$a_o = 0.584$ nm $x_{Cu}=0.244$, $x_{In}=0.256$, $x_{Se}=0.500$	[80]
		$a_o = 0.5755$ nm $x_{Cu}=0.14$, $x_{In}=0.323$, $x_{Se}=0.537$	[80]
Beta	-	$a_o = 0.5766$ nm $C_o = 1.1531$ nm $x_{Cu}=0.15$, $x_{In}=0.31$, $x_{Se}=53.8$	[80]
		$a_o = 0.5751$ nm $C_o = 1.1520$ nm $x_{Cu}=0.115$, $x_{In}=0.329$, $x_{Se}=55.6$	[80]
Cu$_2$In$_4$Se$_7$	Tetragonal	$a_o = 0.5762$ nm $C_o = 1.153$ nm	[78]
		$a_o = 0.5765$ nm $C_o = 1.153$ nm	[78]
CuIn$_3$Se$_5$	Tetragonal	$a_o =0.5754$ nm $C_o=1.1518$ nm	[77]
		$a_o =0.575$ nm $C_o=1.150$ nm	[57]
CuIn$_5$Se$_8$	Hexagonal	$a_o = 1.2147$ nm $C_o = 4.6010$ nm	[70]
		$a_o = 1.212$ nm $C_o = 4.604$ nm $x_{Cu}=0.073$, $x_{In}=0.35$, $x_{Se}=0.577$	[80]
		$a_o = 1.212$ nm $C_o = 4.604$ nm $x_{Cu}=0.07$, $x_{In}=0.356$, $x_{Se}=0.574$	[80]
		$A_o = 0.404$ nm $C_o = 0.404$ nm $x_{Cu}=0.043$, $x_{In}=0.372$, $x_{Se}=0.585$ (high T phase)	[80]

Table 5.3. EMF results for cell I

Run	T (K)	E (mV)	T (K)	E (mV)
1	974.35	160.93	970.15	158.86
	988.15	155.92	1006.85	154.034
	952.05	165.16	989.55	160.62
	1024.75	151.67	1020	150.35
2	951.35	163.52	968.05	160.67
	987.45	157.38	1005.45	153.30
	961.55	164.22	973.95	161.65
	989.15	159.21	1002.35	156.76
	1015.35	153.85	1025.45	149.47
	1028.95	150.75	1043.65	145.25
	1043.35	147.12	1121.15	134.14
	1140.55	131.90	1070.15	142.58
	1083.85	141.30	1097.75	138.67
	1111.35	135.61	1080.00	140.46
3	975.35	159.37	992.35	158.84
	965.95	164.40	949.15	162.86
	971.15	159.51	992.55	156.10
	1013.15	152.80	1063.15	143.16
	1101.15	137.48	1082.85	140.45

Table 5.4. EMF results for cell II

Run	T (K)	E (mV)	T (K)	E (mV)	T (K)	E (mV)
1	867.55	20.98	881.25	25.05	893.95	30.58
	910.05	37.16	925.45	41.94	917.35	38.83
	922.55	42.85	984.65	59.70	1006.35	66.58
	1031.55	74.10	936.55	45.35	960.45	52.09
	986.15	61.95	939.45	44.59	1025.95	73.02
	957.65	55.61	934.15	46.36	950.85	50.47
	963.75	54.40	979.35	58.74	991.15	62.11
	1006.25	65.86	1030.65	73.44	966.55	55.46
	1039.95	78.05	1044.85	76.78	1056.55	82.85
	1094.55	96.71	1149.65	122.06	1053.85	81.56
	1079.65	90.00	1053.85	84.02	1068.15	90.18
	1083.15	96.05	1097.05	101.25	1111.65	106.70
	1126.15	112.25	1140.55	118.95	1155.45	125.83
	1164.05	130.54	1178.75	136.10		
2	968.45	55.63	982.75	59.67	995.05	63.75
	1018.45	70.12	1037.15	76.48	972.65	57.10
	990.45	63.82	1011.15	67.69	995.25	63.26
	934.95	47.25	953.55	51.71	972.55	57.60
	991.45	61.68	1054.75	82.02	1071.45	88.13
	1055.85	82.00	1080.75	89.79	1083.55	90.79

Table 5.5. EMF results for cell III

Run	T (K)	E (mV)	T (K)	E (mV)
1	1090.65	78.65	1108.15	90.52
	1127.15	102.62	1145.15	108.89
	1062.35	68.85	1078.05	76.08
	1097.65	85.05	1112.75	90.86
	977.25	16.16		
2	991.35	26.01	1012.15	36.68
	1030.85	44.92	1050.25	55.82
	1069.75	66.41	1058.65	63.28
	1076.15	69.32	1089.05	74.15
	1101.65	80.37		

Table 5.6. Comparison of α-CuInSe$_2$ to δ-CuInSe$_2$ enthalpy of transformation data.

Solid Phase	T$_{trans}$ (K)	ΔH$^o_{trans}$ (kJ/mol)	Reference
CuInSe$_2$	1058-1083	-	[88]
	1083	-	[87],[49]
	1153	-	[52]
	1125	10.0	[50]
	-	15.9	[89]
	1095-1099	16.2	[61]
	1064	10.0	This work (Cell I)
	1050	21.7	This work (Cell II)

Solid Phase	Melting Temperature (K)	ΔH$_{melting}$ (kJ/mol)	Heat of Fusion (kJ/mol)	ΔS$_{melting}$ (kJ/mol)	Reference
CuInSe$_2$	1259	83.6	-	0.0664	[49]
	1269	-	88.62	-	[61]

Table 5.7. Comparison of the standard enthalpy of formation, $\Delta H^{o}_{f,298}$, and standard molar entropy, S^{o}_{298} of the ternary and some binary compounds in the Cu-In-Se system.

Solid Phase	$-\Delta H^{o}_{f,298}$ (kJ/mol)	Method	Reference	S^{o}_{298} (J/mol K)	Method	Reference
α-CuInSe$_2$	267.4	Mass Spectrometry	[99]	157.7	Pulsed Calorimetry	[53]
	260.2	Calculated	[100]	158.2	Calculated	[91]
	280.0	Calculated	[101]			
	204.0	Calculated	[92]			
	204.7	Optimized	This work			
	189.8	Calculated	[90]			
	202.9	EMF	This work			
	204.4	Calculated	[63]			
InSe	117.8	Calculated	[63]			
In$_2$Se$_3$	78.0	Calculated	[63]			
In$_5$Se$_6$	679.6	Calculated	[63]			
CuSe	41.8	Calculated	[63]			
Cu$_2$Se	65.2	Calculated	[63]			
δ-CuInSe$_2$	200.3	Optimized	This work	182.83	Optimized	This work
Cu$_2$In$_4$Se$_7$	754.2	Calculated	[90]	520.0	Adiabatic Calorimetry	[54]
				513.0	Calculated	[91]
β-CuIn$_3$Se$_5$	472.9	Calculated	[90]	354.8	Calculated	[91]
	266.9	Optimized	This work			
γ-CuIn$_5$Se$_8$	664.6	Calculated	[90]	551.5	Calculated	[91]
	285.7	Optimized	This work			

Table 5.8. Optimized parameters according to the analytical description of the phases[+]

Phase or Function	Parameters
Liquid	$^\circ G_{Cu_2Se}^l = G_{Cu_2Se\_l}$
	$^\circ G_{In_2Se_3}^l = G_{In_2Se_3\_l}$
	$^0 L_{Cu_2Se,In_2Se_3}^l = -25930$
	$^1 L_{Cu_2Se,In_2Se_3}^l = 18000$
	$^2 L_{Cu_2Se,In_2Se_3}^l = -14500$
δ-CuInSe$_2$	$^\circ G_{Cu_2Se:In_2Se_3}^\alpha = 0.5^\circ G_{Cu_2Se\_\beta} + 0.5^\circ G_{In_2Se_3\_\delta} - 17000 + T$
	$^\circ G_{In_2Se_3:Cu_2Se}^\alpha = 0.5^\circ G_{Cu_2Se\_\beta} + 0.5^\circ G_{In_2Se_3\_\delta} + 17000 - T$
	$^0 L_{Cu_2Se,Cu_2Se}^\alpha = G_{Cu_2Se\_\beta} + 2000$
	$^0 L_{In_2Se_3,In_2Se_3}^\alpha = G_{In_2Se_3\_\delta} + 4120$
	$^0 L_{*:Cu_2Se,In_2Se_3}^\alpha = 15000 - 3T$
	$^0 L_{Cu_2Se,In_2Se_3:*}^\alpha = 18050 - 30T$
α-CuInSe$_2$	$^\circ G_{Cu_2Se:In_2Se_3}^\alpha = 0.5^\circ G_{Cu_2Se\_\beta} + 0.5^\circ G_{In_2Se_3\_\delta} - 19350 + 3T$
	$^\circ G_{In_2Se_3:Cu_2Se}^\alpha = 0.5^\circ G_{Cu_2Se\_\beta} + 0.5^\circ G_{In_2Se_3\_\delta} + 19250 - 3T$
	$^0 L_{Cu_2Se,Cu_2Se}^\alpha = G_{Cu_2Se\_\beta} + 8000$
	$^0 L_{In_2Se_3,In_2Se_3}^\alpha = G_{In_2Se_3\_\delta} + 4000$
	$^0 L_{*:Cu_2Se,In_2Se_3}^\alpha = 15000$
	$^0 L_{Cu_2Se,In_2Se_3:*}^\alpha = -8000$
β-Cu$_1$In$_3$Se$_5$	$^\circ G_{Cu_2Se}^l = G_{Cu_2Se\_\beta} + 5000 + 7T$
	$^\circ G_{In_2Se_3}^l = G_{In_2Se_3\_\delta + 3500 + 4T}$
	$^0 L_{Cu_2Se,In_2Se_3}^l = -60000$
	$^1 L_{Cu_2Se,In_2Se_3}^l = 80000$
γ-Cu$_1$In$_5$Se$_8$	$^\circ G_{Cu_2Se}^l = G_{Cu_2Se\_\beta} + 7000 + 6T$
	$^\circ G_{In_2Se_3}^l = G_{In_2Se_3\_\delta + 4000 + 4T}$
	$^0 L_{Cu_2Se,In_2Se_3}^l = -1000 + T$
	$^1 L_{Cu_2Se,In_2Se_3}^l = 179000$
Function	$G_{Cu_2Se\_\alpha} = -80217.34 + 288.16728T - 59.0572T\ln T - 0.0375096T^2$
	(298≤T≤395)
	$= -98255.14 + 662.67401T - 120.090000T\ln T + 0.0400000T^2$

$$-0.6967\text{E-}05T^3+1020000T^{-1} \qquad (395\leq T\leq 800)$$

$$G_{Cu_2Se\_\beta} = G_{Cu_2Se\_\alpha} +6830-17.29114T$$

$$G_{Cu_2Se\_l} = G_{Cu_2Se\_\beta} + 16000 - 11.422T$$

$$G_{In_2Se_3\_l} = G_{In_2Se_3\_\delta} + 88763.31-75.84304T$$

$$G_{In_2Se_3\_\gamma} = -350296.2 + 559.60784T-113.41683T\ln T-0.0179945T^2$$

$$(298\leq T\leq 1018)$$

$$G_{In_2Se_3\_\delta} = -354076.2+554.14084T-113.41683T\ln T-0.0179945T^2$$

$$(298\leq T\leq 1018)$$

$$=-323687.73+770.53003T-151T\ln T$$

$$(1018\leq T\leq 6000)$$

+ Temperature (T) is in Kelvin. The Gibbs energies are in J/mole.

Table 5.9. Invariant equilibria in the Cu_2Se-In_2Se_3 system

Phases	Composition [at. % In_2Se_3]	Temperature [K]	Reaction Type	Reference
Liquid/δ-$CuInSe_2$	50	1263	Congruent Melting	[51]
	50	1254		[48]
	50	1259		[49]
	50	1275		[79]
	53	1280		[71]
	50	1259		[87]
	50	1280		[48]
	50	1258		[80]
	50-53	1275		[1]
	50	1259		[67]
	54	1265		This work
Liquid/Cu_5InSe_4	16-18	1223	Congruent Melting	[71]
	16.0	1216		[69]
Liquid/$Cu_{13}In_3Se_{11}$	21.56	1220	Congruent Melting	[1]
δ-$CuInSe_2$/Cu_2Se_β/ α-$CuInSe_2$	42	1053	Eutectoid	[79]
	43	1053		[71]
	43	1053		[87]
	45	1060		[48]
	46.6	1058		[1]
	43	1053		[67]
	47.0	1063		[69]
	47.3	1062.7		This work

δ-CuInSe₂/α-CuInSe₂	50	1103	Congruent Transformation	[62]
	50	1103		[79]
	50	1083		[87]
	50	1100		[48]
	50	1088		[80]
	50	1091		[1]
	50	1083		[67]
	50	1083		[69]
	50	1087		[102]
	50	1096		This work
ξ-CuInSe₂/δ-CuInSe₂	50	1123	Congruent Transformation	[102]
δ-CuInSe₂/α-CuInSe₂/ β-Cu₁In₃Se₅	68	833	Eutectoid	[79]
	67	868		[87]
	55	1075		[48]
	62	978		[80]
	61.8	793		[1]
	66-68	940-950		[67]
	56	998		This work
Liquid/Cu₅InSe₄/ δ-CuInSe₂	19-20	1168	Eutectic	[71]
	17.0	1163		[69]
Liquid/Cu2Se_β/ Cu₁₃In₃Se₁₁/	21	1208	Eutectic	[1]
Liquid/Cu₁₃In₃Se₁₁/ δ-CuInSe₂	22	1215	Eutectic	[1]
Liquid/Cu2Se_β/ δ-CuInSe₂	22	1055	Eutectic	[79]
	11	1053		[71]
	22	1188		[87]
	20-23	1188		[67]
	11.0	1216		[69]
	16.8	1188.2		This work
Liquid/γ-Cu₁In₅Se₈/ In₂Se₃_δ	96	1133	Eutectic	[80]
	95	1143		[1]
	95	1158		This work
Liquid/δ-CuInSe₂/ β-Cu₁In₃Se₅	67	1198	Peritectic	[80]
	75.2	1173		[1]
	73.5	1213		This work
Liquid/β-Cu₁In₃Se₅/ γ-Cu₁In₅Se₈	83	1153	Peritectic	[80]
	84.3	1183.5		This work
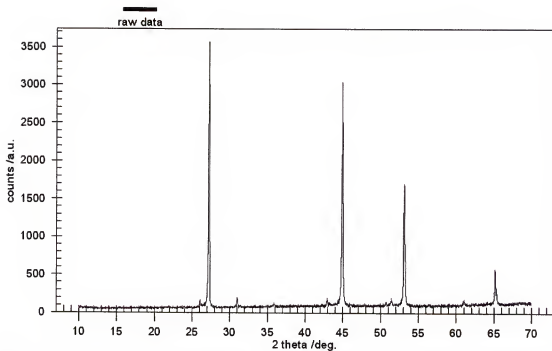
Figure 5.1 XRD spectrum of synthesized $In_2Se_3+Cu_2Se$ 30:70 mol % mixture before the experiment for cell I.
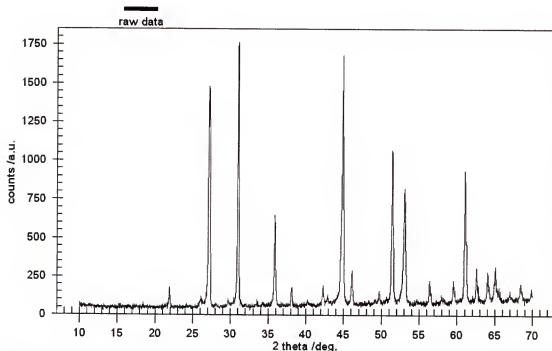

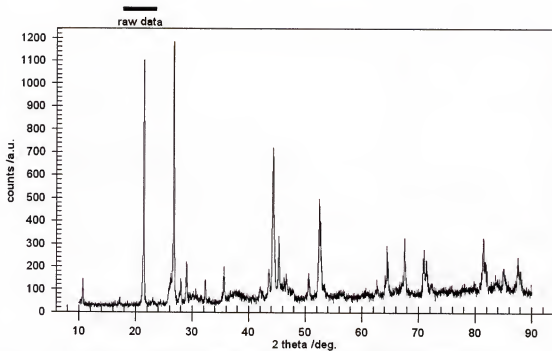Figure 5.2 XRD spectrum of a $In_2Se_3+Cu_2Se$ 30:70 mol % mixture after the experiment for cell I.

Figure 5.3 XRD spectrum of synthesized $Cu_1In_3Se_5$ + $CuInSe_2$ obtained from $x_{In_2Se_3}=64mol\%$ sample before the experiment for cell II.
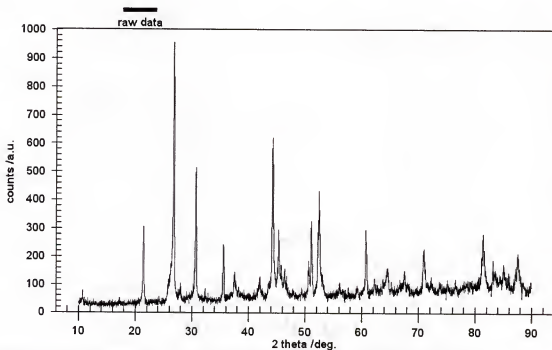
Figure 5.4 XRD spectrum of synthesized $Cu_1In_3Se_5$ + $CuInSe_2$ obtained from $x_{In_2Se_3}=64mol\%$ sample after the experiment for cell II.
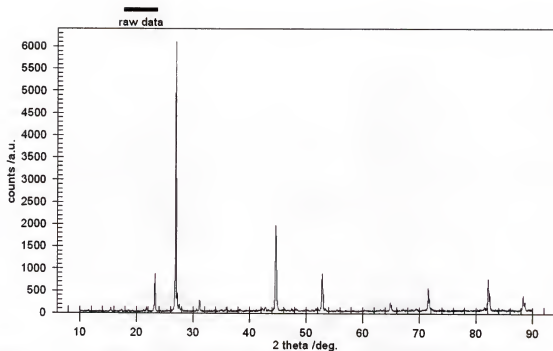
Figure 5.5 XRD spectrum of synthesized $CuIn_5Se_8(s)$ + $Cu_1In_3Se_5$ obtained from $x_{In_2Se_3=80mol\%}$ sample before the experiment for cell III.
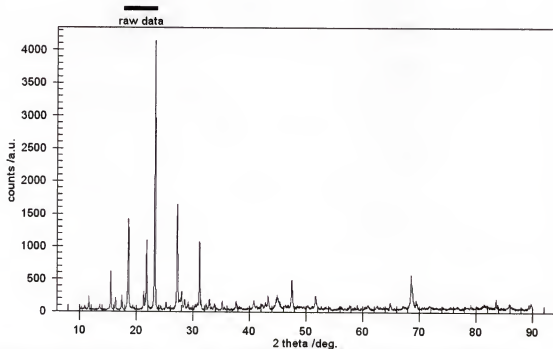
Figure 5.6 XRD spectrum of synthesized $CuIn_5Se_8(s)$ + $Cu_1In_3Se_5$ obtained from $x_{In_2Se_3=80mol\%}$ sample after the experiment for cell III.
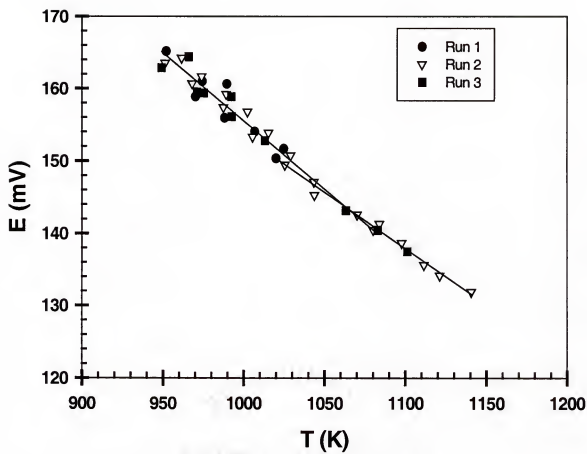
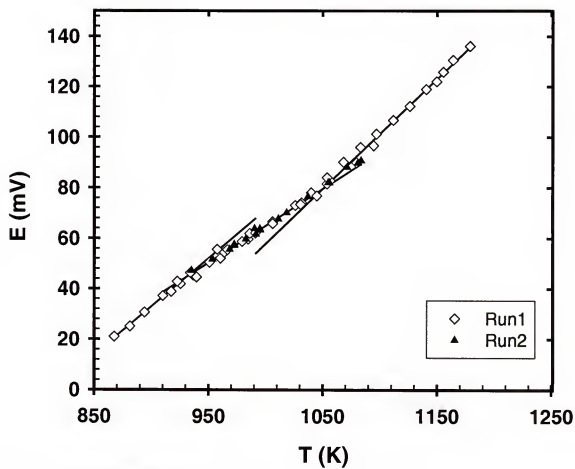Figure 5.7 Temperature dependence of the EMF of cell I.
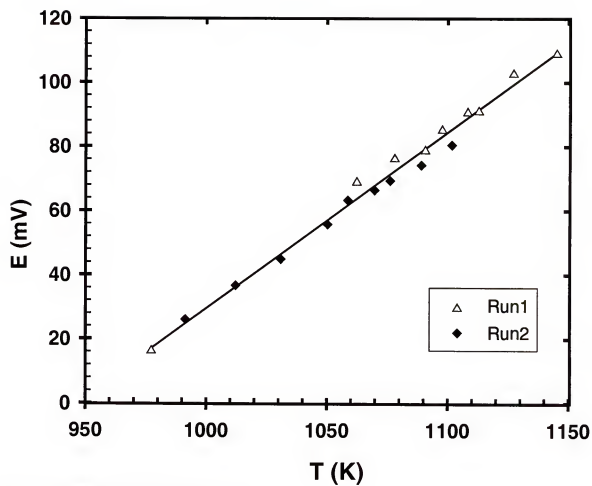
Figure 5.8 Experimental results of cell II.
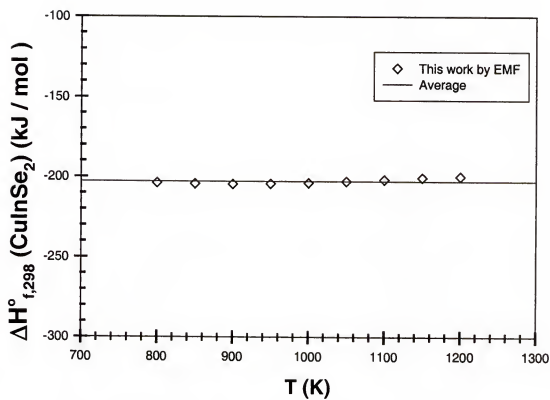
Figure 5.9 EMF results for the cell III.

Figure 5.10 Third-law determination of the standard enthalpy of formation of α-CuInSe₂.
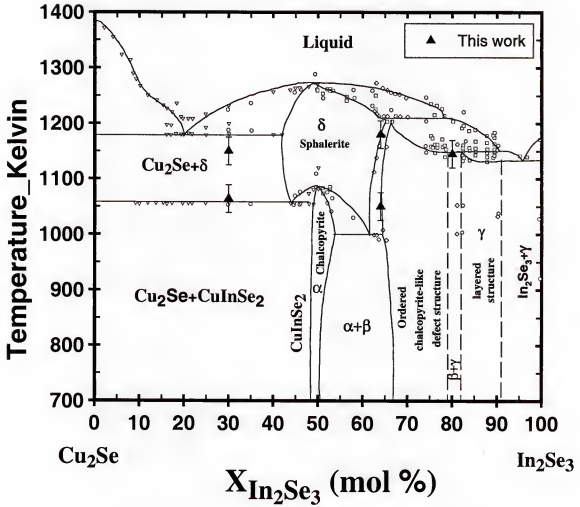
Figure 5.11 Evaluated phase diagram along with EMF results for Cu$_2$Se-In$_2$Se$_3$ system.
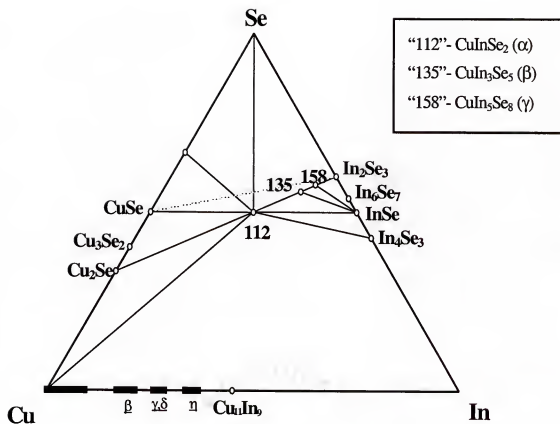
Figure 5.12 Isothermal section of the Cu-In-Se phase diagram at 1000 K.
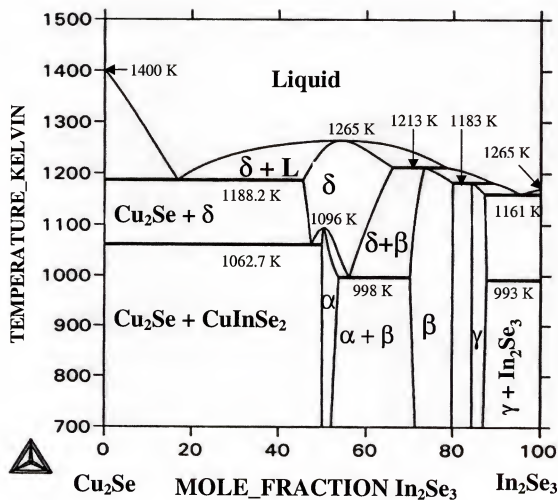
Figure 5.13 Calculated Cu$_2$Se-In$_2$Se$_3$ phase diagram based on the optimized parameters.
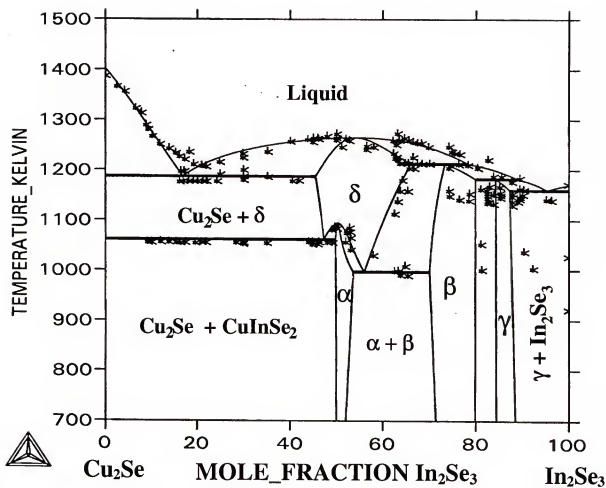
Figure 5.14 Comparison between the calculated Cu_2Se-In_2Se_3 phase diagram and various experimental data
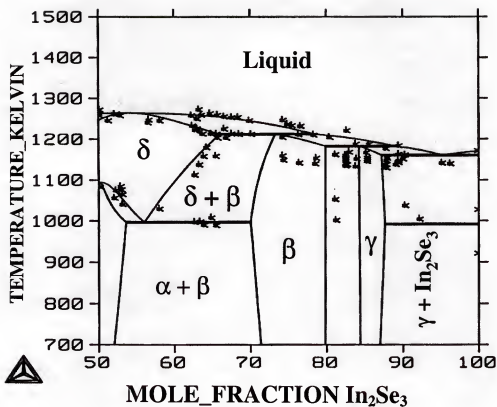
Figure 5.15 Comparison between the Cu₂Se-In₂Se₃ phase diagram and various experimental data in the vicinity of In₂Se₃ rich section.

Figure 5.16 Comparison between the calculated Cu₂Se-In₂Se₃ phase diagram and various experimental data from 0.35 to 0.65 mole fraction of In₂Se₃.

Figure 5.17 Phase Diagram of CuInSe$_2$-InSe system by Zargarova [62].

CHAPTER 6
THERMOCHEMISTRY AND PHASE DIAGRAM OPTIMIZATION OF GA-SE SYSTEM

Introduction

The Ga-Se system is of interest in developing CIS based solar cell technologies as a sub-system of $CuIn_xGa_{1-x}Se_2$ absorber material. The recent 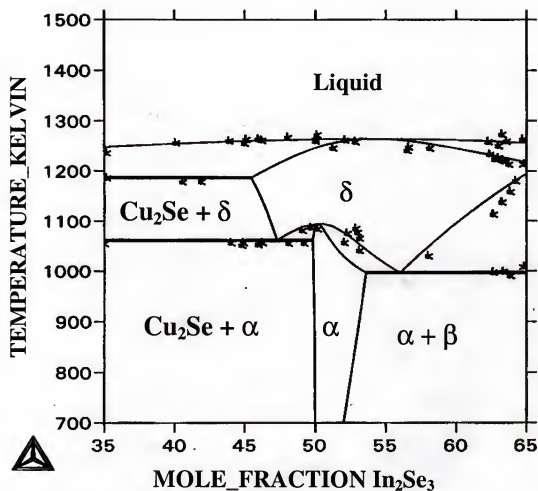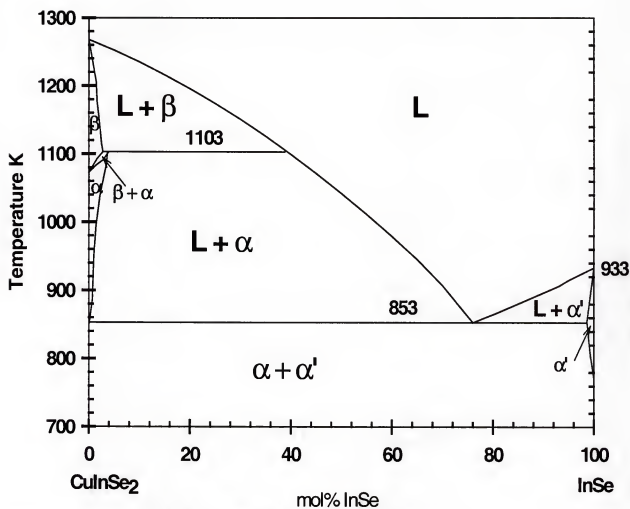studies show that Ga addition to $CuInSe_2$ improved solar power efficiencies to a 21 % in laboratory devices [103]. The development of low cost, low temperature reaction pathways for CIGS based solar cells require rudimentary thermodynamic and phase diagram data of related sub-systems. The thermochemistry and phase diagram of the Cu-Ga and Ga-Se binaries are comparatively less studied. Along with recent technological improvements, better understanding the role of Ga in photo-electronic properties and defect structure of CIGS should be useful.

A critical assessment of thermochemistry and phase diagram information has not been performed. According to reported phase diagrams [104]-[108] two well-defined compounds exist in the system. GaSe is characterized as a highly anisotropic compound with a layered crystal structure and Ga_2Se_3 is reported with a zincblende structure having α and β modifications with a first order transition temperature at around 967K. The presence of Ga_2Se phase was suggested by an earlier report [108]; however, the later investigators excluded the formation of this phase since it was unstable and could not be prepared by direct synthesis.

Thermodynamic data for compounds and some vapor pressure data are reported in the literature. However, some of the literature data on the selenium-rich side of the phase diagram displays an unusual flat Se-rich liquidus. Since there is limited data in this region an assessment would be useful to establish the measurability limits. A consistent thermodynamic description of the liquid phase and β-Ga_2Se_3 defect compound would be helpful in predicting unknown regions of phase diagram.

The purpose of this research is to measure selected thermochemistry and phase diagram data in the Ga-Se system. Solid state electrochemical cells were used to measure liquid phase Ga activity solution parameters (a_{Ga}, a_{Se}) in the composition range of 15 to 45 % at. Se, corresponding to the two-phase region between solid GaSe and liquid. The standard Gibbs energy of formation of Ga_2Se_3 as well as the temperature and enthalpy of the α to β-Ga_2Se_3 transformation were also obtained by analysis of the solid state EMF measurements.

The thermodynamic and phase diagram data in the Ga-Se system was critically optimized based on literature and measured data. A self consistent set of thermochemistry and phase diagram data were prepared. The liquid phase was described by the associated solution model with two associates GaSe and Ga_2Se_3. The α-Ga_2Se_3 phase was described by the sublattice model with two sublattices according to the formula $(Ga,Va)_2 (Se,Va)_3$. The other two intermediate phases, GaSe and β-Ga_2Se_3 were treated as line compounds. The calculated phase diagram and thermochemical data show reasonable agreement except in the limits of the selenium rich liquidus line.

Literature Review

The phase diagram of the Ga-Se system has been measured by several investigators [104]-[108] using differential thermal analysis (DTA), X-Ray diffraction (XRD), microscopy and vapor pressure methods. This system is characterized by the occurrence of two stable binary compounds: GaSe and Ga_2Se_3. Ga_2Se_3 has two stable polymorphisms: β-Ga_2Se_3 is the low temperature form and α-Ga_2Se_3 is the high temperature form, which exists with a relatively narrow homogeneity range. In the equilibrium diagram of the Ga-Se system, a monotectic is found between Ga and GaSe at 1190K and a miscibility gap with composition limits of 7.5 to 45.5 at % Se at this temperature. The eutectic is formed at 1157 K in the composition region between GaSe and Ga_2Se_3. Above 60 at % Se, Ga_2Se_3 and Se are co-existing. The thermodynamic data, $\Delta H^o_{f,298}$ of GaSe was studied by direct bomb calorimetry [109], whereas the existing data on Ga_2Se_3 [110]-[112] and comparative calculation by Burylev [113] show marked discrepancies. Moreover, not much data were available on the thermochemistry of the Ga-Se system.

Rustamov [108] presented the existence of the compound Ga_2Se, but the later investigators [105], [102], [106] excluded the formation of solid Ga_2Se in the equilibrium phase diagram. Ollitraut-Fichet [102] predicted a Se-rich liquid miscibility gap, whereas others [108], [105], [114], [106] did not observe a monotectic in this region. Mikkelsen [114] considered the unusual flat Se-rich liquidus may be due to an abrupt change in Ga solubility and probably a change in the liquid structure. Ga_2Se_3 shows other thermodynamically unstable polymorphisms, β'-Ga_2Se_3 and γ-Ga_2Se_3 [106]. In the

present optimization of the equilibrium phase diagram and thermodynamic properties, Ga_2Se, $\beta'-Ga_2Se_3$, $\gamma-Ga_2Se_3$ and the Se-rich miscibility gap are not considered.

Fernelius [115] reviewed the properties of GaSe single crystal and organized the published literature by growth, structural, mechanical, electrical, thermal and optical properties. GaSe was categorized as a possible candidate material for optical frequency conversion in the near to far infrared (1-18 μm) wavelength. The published data prior to 1994 were summarized. A summary of the positives and negatives for nonlinear optical properties was also given.

Mamedov [116] reported $C_v=0.329T^{1.00}$ (60 to 87K) J/mol K ,and $C_p=47.9$ (300K) J/mol K by the measurements of vacuum adiabatic calorimeter. Jandl [117] measured dispersion curves and calculated the C_v data from a phonon frequency distribution function. The agreement with the measured heat capacity is excellent.

Sharifov [118] measured $\Delta H^o_{298}[Ga_2Se_3(cubic)]= -88.1 \pm 3.1$ kcal/mol by bomb calorimetry. His results differed considerably from earlier results of -105.0 kcal/mol by Hahn [119] and -110.0 kcal/mol by Gadzhiev [120]. However, he claimed that the earlier results might have contained the same type errors related to measurement method. Burylev [113] investigated this discrepancy and estimated the standard enthalpy of formation by combining Kaputinskii thermochemical logarithmic curve rule and linear dependence of enthalpies of formation assumption between homotypic substances. Burylev [113] reported $\Delta H^o_{298}[Ga_2Se_3] = -85.0 \pm 3.0$ kcal/mole and $\Delta H^o_{298}[GaSe] = -34.29 \pm 1.21$ kcal/mole by comparative calculation including the experimental data of Naumov [111].

Mikkelsen [121] measured the Se vapor pressures in the temperature range 700 to 1050 °C by the dew point method. The Se vapor pressure was found to decrease rapidly near 60 % Se. The T-x and P-x liquidus curves were thermodynamically modeled by a regular associated solution model for the liquid phase, with a single associate, Ga_2Se_3.

The crystal structure of ordered Ga_2Se_3 was studied by Lubbers et al [122]. It was claimed that the homogeneity range of this phase resulted from ordering of randomly distributed Ga atoms and "structural vacancies" on the cation sites of the zincblende lattice. The results of Lubbers et al. [122] confirmed some general statements made by Newman [123],[124]. The arrangement of Se atoms according to Newman [123] in which one-third of the anion sites occupied by Se(X) and two-thirds by Se(Y) is adapted in our defect model to explain the existence of two different sublattices in ordered structure. Earlier, Tonejc [125] studied the lattice parameters of $(Ga_xIn_{1-x})_2Se_3$ compounds. The phases, lattice parameters and the linear coefficient of the lattice thermal expansion were determined by high-temperature X-Ray diffraction between room temperature and the melting temperature for the system $(Ga_xIn_{1-x})_2Se_3$ $(1 \geq x \geq 0)$. A wide homogeneity range for this zincblende structure was found in the Ga-rich region when a certain temperature was reached. The lattice parameter of Ga_2Se_3 was given as a function of temperature. The polymorphic transformations as reported by Goryunova [126] were not detected.

Suzuki [105] determined the phase diagram of Ga-Se system by differential thermal analysis. The peritectic single phase Ga_2Se observed by Rustamov et al.[108] did not appear in DTA analysis. A liquid miscibility was presented. The Ga_2Se_3 phase was given as a line compound and single phase with no polymorphism; however, the selenium rich liquidus line showed large discrepancy with the published data of Rustamov [108].

Dieleman [106] most recently has evaluated the phase diagram in detail and confirmed the stability of GaSe and Ga_2Se_3 phases. The stability of α-Ga_2Se_3 and β-Ga_2Se_3 phases and the transformation temperature were reported. XRD analysis performed in the composition region less than 50 % at. Se indicated that GaSe and Ga were coexisting phases. Between 50 % at. Se and 60 % at. Se, GaSe and Ga_2Se_3 were observed. Samples at compositions higher than 60 % at. Se consisted of only Ga_2Se_3 and selenium. The liquid miscibility gap was also reported between 7.5 % at. Se and 45.5 % at. Se closing at 994 °C.

The compound GaSe is well studied due to its interesting structural and optical and photo-electronic properties for prospective semiconductor applications. The GaSe structure was found to be highly anisotropic and chemical bonding in GaSe layered structure showed strong structural anisotropy. Every layer consists of strongly covalent bonded four atoms, which is hexagonal along the layered axis. Layered atoms are stacked on top of each other with a relatively weaker Van der Waals type bonds, which allows them to glide over each other [127].

Anis [128] studied the space-charge-limited current behavior for undoped p-GaSe for the temperature range 200K to 350K. It was concluded that the frequently observed hole energy level of 0.195 eV was a single discrete trapping level with a density about $4*10^{22}$ m^{-3}. The conduction was found to be extrinsic (N_A- N_D =$3*10^{16}$ cm^{-3}). The energy of the shallow acceptor was decided to be structural defects rather than chemical impurities.

Minder [129] measured the electron and hole drift velocity in the direction parallel to c axis between 80 and 400K. A three dimensional character of carrier transport

properties was found. There was no evidence of large anisotropy of charge-carrier transport properties. The mobility values for electrons and holes at 300K parallel to the c axis were reported to be 80 cm^2/Vs, and 210 cm^2/Vs, correspondingly. The perpendicular mobility values are given as 300 cm^2/Vs for electrons, and 60 cm^2/Vs for holes.

Dobynde [130] investigated the photoluminescence and absorption in GaSe at 77K. The ε-GaSe ingots were used in the experiments. The spontaneous photoluminescence (PL) spectra at different excitation and different excitation levels were investigated. Experiments supported the assumption of the presence of two minimum in the conduction band.

Ludviksson [131] studied the vacuum sublimation of GaSe. Single crystal GaSe was grown on GaAs(111)A by vacuum sublimation from a single GaSe source without terminating the dangling bonds at the surface prior to deposition. Mass spectroscopy was used to determine the composition of the molecular source. It was found that the gaseous species are predominantly Ga$_2$Se and Se$_2$.

A few epitaxial growth studies were published. Erkoc [132] studied the electronic states of InSe/GaSe superlattice. He calculated the potential and the charge density distribution for three different types of doping. Lang [133] studied the band lineup of mismatched InSe/GaSe quantum well structures prepared by van der Waals epitaxy. Palmer [134] investigated the growth and characterization of GaSe on As–passivated Si(111) substrates. The epitaxial grown GaSe layered structure was examined as a lattice mismatch/thermal expansion mismatch buffer layer in the GaAs on Si system. The van der Waals epitaxial growth of GaSe on Si(111) surface was also studied by Vinh [135]. It

was suggested according to the channeling measurements that a thin GaSe film grown on silicon can be obtained with the same crystalline quality as the bulk form of GaSe.

Shigetomi [137] studied impurity levels in p-GaSe doped with Mn [136] and with Cu. Photoluminescence (PL), Hall effect (HE), and deep-level transient spectroscopy (DLTS) measurements were performed. Hernandez [138] studied temperature dependence of refractive index and absorption coefficient of GaSe at 633 nm.

Sanchez-Royo [127] studied single crystal GaSe crystals doped with tin by resistivity and Hall effect measurements. The transport properties of doped GaSe single crystal were reported. The chemical bonding for GaSe was characterized by strong anisotropy. Optical properties were also reported as anisotropic and the band gap value of 2.02 eV was reported.

Micocci [139] studied the photo-electronic properties as a function of temperature and light intensity. It was stated that GaSe single crystals can act as both p and n type semiconductors. GaSe single crystal were grown by Bridgman-Stockbarger method and thermally stimulated current (TSC) and photo-conductivity of n-GaSe doped with chlorine was studied. Micocci [140] also studied the electrical properties of n-GaSe chlorine doped single crystals. It was concluded that the electrical properties were dominated by a deep donor level at 0.57 eV below the conduction band.

Gurbulak [141] studied the temperature dependencies of the Hall mobility of holes and the carrier concentration. The magneto-resistance and Hall effect measurements were carried out in undoped and Gd doped p-GaSe samples. Magnetic field dependencies of electrical properties were also investigated.

In summary, some thermodynamic data for the compounds and the liquid phase have been measured by means of vapor pressure, calorimetric, DTA, and electromotive force (EMF) methods. However, there is a considerable discrepancy in the measured data, and some parts of the phase diagram are not well-studied. In this work, EMF measurements were performed and a critical assessment of Ga-Se system is performed based on the EMF results and literature data. A self-consistent phase diagram and set of thermodynamic data are obtained through this assessment.

Experimental

Materials

The solid alloys with compositions 15, 35, 45, 55 and 65 at. % Se were synthesized from pure Ga shots (Johnson Matthey) and Se pellets (Alpha Aesar). The samples were individually encapsulated in silica ampoules at a pressure less than 10 Pa and heated to 1273K and maintained at that temperature for 24 hours to ensure completion of the formation of the bi-phasic alloys. Then the silica ampoules were further heat treated in steps of 1173K for 64 hr and 1073K for 40 hr followed by annealing at 723K for 24 hr. All the samples were characterized by powder X-Ray Diffractometry (XRD) method within its 5 mass % limit of detection for impurity phases. Gallium shot (Johnson Matthey, purity 99.99%) and Ga_2O_3 powder (Johnson Matthey, purity 99.99%) were used as received for the EMF measurements.

EMF Measurements

The test electrodes were made by mixing the (gallium-selenium) alloys of compositions 15, 35, 45, 55 and 65 at. % Se individually with one third of their mass of gallium oxide (Ga_2O_3) powder. The mixtures were allowed to equilibrate within the cell. The reference electrode was prepared from a mixture of 4:1 weight ratios of Ga and

Ga_2O_3 powder. The cell configuration of the EMF experiments for each cell can be schematically represented as:

C,W, Ga (l), Ga_2O_3 (s) // YSZ // Ga_2O_3 (s), GaSe (s), Liquid1, C,W   cell I (0<x_{Se}<0.5)

C,W, Ga (l), Ga_2O_3 (s) // YSZ // Ga_2O_3 (s), GaSe (s), Ga_2Se_3 (s), C,W   cell II (x_{Se}=0.55)

C,W, Ga (l), Ga_2O_3 (s) // YSZ // Ga_2O_3 (s), Ga_2Se_3 (s), Liquid2, C,W   cell III (x_{Se}=0.65)

where YSZ denotes the 15 mass % yittria (Y_2O_3) stabilized zirconia (ZrO_2) solid electrolyte. The cylindrical crucibles of 15 mm in diameter and 3mm thickness YSZ were used. High density nuclear grade graphite cups were employed to contain the test electrodes or the reference electrodes depending on cell construction. The graphite and YSZ crucibles enclosing the test and reference electrodes were sealed with Aremco 571 magnesia based ceramic adhesive to avoid the vaporization of selenium from the test electrode sample as well as to enclose liquid Ga in the reference electrode. The absence of asymmetric potentials due to graphite cups were verified by the observation of null EMF ($\pm$ 1 mV) over the range 800 to 1200 K in a symmetric cell with identical Ga(l) + Ga_2O_3 electrodes. Purified Argon at a very low flow rate was fed in to the system to serve as the blanket gas for the galvanic cell. The temperature of the cell was measured by using a calibrated Platinum-10% Rhodium / Pure Platinum thermocouple. Thermal cycling and micro-polarization were used as a test for reversibility and equilibrium nature of the EMF measurements. Other experimental details such as temperature control, purification of Argon, and voltage measurement are given in references [81]-[83].
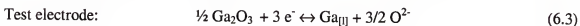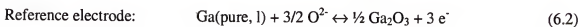
Results and Discussion

The EMF results on cell I, cell II and cell III for the composition of gallium-selenium alloys encompassing 15, 35, 45, 55 and 65 at. % Se are presented in Tables 6.1

to 6.5. The least squares expressions of the EMF values for the 5 compositions studied are listed in Table 6.6. The solution parameters and transformation enthalpies were calculated depending on the constitution of the electrochemical cell from the following general relation,

$$\Delta G_R = \Delta G^0_R + RT \ln K = -n F E \tag{6.1}$$

Liquid Phase Activity Measurements

The electrochemical half-cell reactions for the cell I, which was employed for the liquid phase activity measurements, can be represented schematically as:

Reference electrode: $Ga(pure, l) + 3/2\ O^{2-} \leftrightarrow \frac{1}{2}\ Ga_2O_3 + 3\ e^-$ \hfill (6.2)

Test electrode: $\frac{1}{2}\ Ga_2O_3 + 3\ e^- \leftrightarrow Ga_{[l]} + 3/2\ O^{2-}$ \hfill (6.3)

$Ga_{[l]} + Se_{[l]} \leftrightarrow GaSe(s)$ \hfill (6.4)

Overall: $Ga(pure, l) + Se_{[l]} \leftrightarrow GaSe(s)$ \hfill (6.5)

where $Se_{[l]}$ and $Ga_{[l]}$ represent the selenium and gallium in the gallium-rich liquid phase.

Applying the first and second laws of thermodynamics for a reversible electrochemical cell, it can be shown that Gibbs energy change of the system by passing one faraday of electrical charge must be equal to the reversible electrical work done on the system.

$$dG = -dW = -nFdE \tag{6.6}$$

$$\Delta G = -nFE \tag{6.7}$$

The Gibbs energy change for reaction (6.5) can be represented as:

$$\Delta G_R = -nFE$$
$$\Delta G^o_R = G^o_{GaSe(s)} - G^o_{Ga(pure,l)} - G^o_{Se[l]} \tag{6.8}$$

If pure liquid selenium is chosen as the reference state, then the activity and the chemical potential of selenium in gallium-rich liquid could be represented by the following equations:

$$a_{Se_{[l]}} = \exp[(3FE + G^o_{GaSe(s)} - G^o_{Ga(pure,l)} - G^o_{Se[l]})/RT] \qquad (6.9)$$

$$RT \ln(a_{Se}) = \mu_{Se} - \mu^0_{Se} = 3FE + \Delta G^0_R \qquad (6.10)$$

EMF and chemical potential curves are given in Figure 6.1 and Figure 6.2 for cell I with 15 at. % selenium sample. Figure 6.3, Figure 6.4, Figure 6.5, and Figure 6.6 show the experimental data and chemical potential for 35% and 45% selenium compositions correspondingly. Figures 6.2, 6.4 and 6.6 clearly indicate that the chemical potential data measured for 15 at. % Se sample is the most consistent with optimization results. The effect of high pressure of selenium on the stability of EMF cell can be clearly observed from the measured data. For high selenium compositions, the average error limit with respect to optimized results is an order magnitude higher in millivolts compared to low selenium content sample.

The α to β transition in Ga$_2$Se$_3$

The galvanic cell employed for cell II is represented by

C, W, Ga (l), Ga$_2$O$_3$ (s), Ga$_2$O$_3$ (s) // YSZ // Ga$_2$O$_3$ (s), GaSe (s), Ga$_2$Se$_3$ (s), C, W

The EMF expressions for the above cell are given as follows:

$$E_{II\,(a)} \pm 2.32 \ (mV) = 417.27 - 0.27477 \ T \ (K) \ (\ 823\text{-}962K) \qquad (6.11)$$

$$E_{II\,(b)} \pm 2.25 \ (mV) = 476.63 - 0.33454 \ T \ (K) \ (\ 986\text{-}1100K) \qquad (6.12)$$

The half cell reactions of the cell II could be written as:

Reference electrode: Ga(pure, l) + 3/2 O^{2-}(g) $\leftrightarrow$ ½ Ga$_2$O$_3$(α or β) + 3 e$^-$ \qquad (6.13)

Test electrode: $Ga_2Se_3(\alpha \text{ or } \beta) + \frac{1}{2} Ga_2O_3 + 3 e^- \leftrightarrow 3 GaSe(s) + 3/2 O^{2-}(g)$ (6.14)
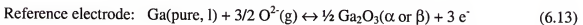
For the passage of 3 Faraday of electricity, the overall cell reaction can be represented by the following reaction:

Overall: $Ga(pure, l) + Ga_2Se_3(\alpha \text{ or } \beta) \leftrightarrow 3 GaSe(s)$

(6.15)
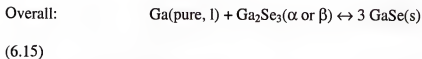
The Gibbs energy changes $\Delta G_{R(\alpha)}$ and $\Delta G_{R(\beta)}$ for the reaction were calculated using the Nernst equations and are given below.

$$\Delta G_{R(\alpha \text{ or} \beta)} = 3 \Delta G^o_f (GaSe(s)) - \Delta G^o_f (Ga_2Se_3(\alpha \text{ or } \beta)) \tag{6.16}$$

$$\Delta G_{R (\alpha)} \pm 0.67 \text{ (kJ mol}^{-1}) = -120.78 + 0.07954 \text{ T(K)} \tag{6.17}$$

$$\Delta G_{R(\beta)} \pm 0.65 \text{ (kJ mol}^{-1}) = -137.97 + 0.09684 \text{ T(K)} \tag{6.18}$$

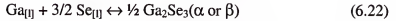Equations (6.17) and (6.18) are valid for the α and β forms of Ga_2Se_3, respectively, in the temperature ranges indicated in Equations (6.11) and (6.12). Since there is no phase transition for either GaSe or Ga in the temperature range 823 to 1100K, the difference in ΔG_R calculated from Equations (6.17) and (6.18) correspond to the standard Gibbs energy change, $\Delta G_{R (\alpha - \beta)}$ for the α to β transition in Ga_2Se_3. Thus, by solving the expressions (6.17) and (6.18), one obtains the following Gibbs energy expression for the transformation:

$$\Delta G_{R(\alpha-\beta)} (Ga_2Se_3) \pm 1.32 \text{ (kJ mol}^{-1}) = -17.19 - 0.01730 \text{ T (K)} \tag{6.19}$$

This leads to values of 993.6 K and 17.2 kJ mol^{-1} for T_{trans} and standard enthalpy of transition, ΔH^o_{trans} of Ga_2Se_3. This transformation enthalpy value was directly used in the optimization of the phase diagram, which is explored in the following sections.

The α to β transition in Ga_2Se_3 from Cell III

The electrochemical reactions for the cell III can be represented as:

Reference electrode:	$Ga(pure, l) + 3/2\ O^{2-} \leftrightarrow \frac{1}{2}\ Ga_2O_3 + 3\ e^-$	(6.20)
Test electrode:	$\frac{1}{2}\ Ga_2O_3 + 3\ e^- \leftrightarrow Ga_{[l]} + 3/2\ O^{2-}$	(6.21)
	$Ga_{[l]} + 3/2\ Se_{[l]} \leftrightarrow \frac{1}{2}\ Ga_2Se_3(\alpha\ or\ \beta)$	(6.22)
Overall:	$Ga(pure, l) + Se_{[l]} \leftrightarrow \frac{1}{2}\ Ga_2Se_3(\alpha\ or\ \beta)$	(6.23)
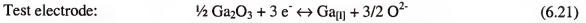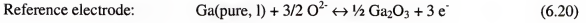
where $Se_{[l]}$ and $Ga_{[l]}$ represent the selenium and gallium in the selenium-rich liquid solution.

As in the case of cell II, by solving the EMF expressions for 65 at. % Se, which are given in Table 6.6, one obtains the temperature of transition, T_{trans} value of 1004K for Ga_2Se_3 is in good agreement with the data obtained from cell II (993.6K) and with that of 1003K reported by Barin and Knacke [142].

Standard Gibbs Energy of Formation of Ga_2Se_3

The suggested expression for ΔG^o_f of GaSe was obtained from Barin and Knacke [142] and is given by the following relation:

$$\Delta G^o_f\ (GaSe)\ (kJ/mol) = -187.81 - 0.06590\ T\ (K)\ (800-1100K) \qquad (6.24)$$

Substituting in equation (6.16), the numerical expressions of (6.17) and (6.18) as well as the Equation (6.24), the standard Gibbs energy of formation of Ga_2Se_3 (α) or (β) are:

$$\Delta G^o_f\ (Ga_2Se_3, \alpha)\ (kJ/mol) = -442.65 + 0.11816\ T(K) \qquad (6.25)$$

$$\Delta G^o_f\ (Ga_2Se_3, \beta)\ (kJ/mol) = -425.46 + 0.10086\ T(K) \qquad (6.26)$$

The ΔG^o_f value at 900 K and 1000 K were calculated as -336.306 and -324.49 kJ/mol for $Ga_2Se_3(\alpha)$ which are in excellent agreement with that of -337.71 and -324.839 kJ/mol cited by Barin and Knacke [142].

Computation of $\Delta H^o_{f,298}$ of Ga$_2$Se$_3$(α)

To assess the temperature dependent errors in the EMF measurements on cell II, a third law analysis was performed. For this purpose, the values of the free energy functions of Ga(l), Se(s) and Ga$_2$Se$_3$(s) from Barin [142] were combined with ΔG^o_R values calculated from each EMF value along with the ΔG^o_f of GaSe at each experimental temperature from Table 6.4 to derive those of $\Delta H^o_{f,298}$ at different temperatures. A third law plot of $\Delta H^o_{f,298}$ of Ga$_2$Se$_3$ (α) is shown in Figure 6.7 The mean value of $\Delta H^o_{f,298}$ of Ga$_2$Se$_3$ was found to be -405.6 kJ/mol. The almost random scatter of values of $\Delta H^o_{f,298}$ around its mean value in this plot indicates the absence of significant temperature dependent errors in the EMF measurements. This value is also found to be in excellent agreement with -408.8 kJ/mol reported by Barin [142]. These values are compared with those of other literature values along with S^o_{298} in Table 6.7.

Phase Diagram Assessment and Optimization

The assessed phase diagram of Ga-Se system is shown in Figure 6.8. The EMF results of the temperature of transition values obtained from 55 and 65 at. % Se samples for cells II and III experiments are marked on the given figure. The optimized parameters of the stable phases in the Ga-Se system are listed in Table 6.11. The phase diagram and thermodynamic properties of this system were calculated with the Poly-3 module of the Thermo-Calc program package. The calculated phase diagram is given in Figure 6.9.

Pure Elements and Stoichiometric Compound Phases

The Gibbs energy of Ga was obtained from [143], and that of Se from [1]. The Gibbs energies of GaSe and β-Ga$_2$Se$_3$ were obtained from [144] and [145], respectively.

The equation given below is used to represent the temperature dependence of the Gibbs energies of pure elements and stoichiometric compound phases (GaSe and β-Ga$_2$Se$_3$),

$$^{\circ}G = a + bT + cT\ln T + dT^2 + eT^3 + fT^{-1} \tag{6.27}$$

where $^{\circ}G$ is the standard Gibbs energy, T is the absolute temperature.

Liquid Phase

The associated solution model developed by Sommer [84] is used to describe the Gibbs energy of the liquid phase. Two associates, GaSe and Ga$_2$Se$_3$, are used in this modeling

$$(Ga, GaSe, Ga_2Se_3, Se)_l \tag{6.28}$$

The Gibbs energy of this phase (given for 1 mole of atoms) is expressed as

$$G^l = {}^{ref}G^l + {}^{id}G^l + {}^{E}G^l \tag{6.29}$$

where l represents liquid. The term $^{ref}G^l$ is equal to

$$^{ref}G^l = y_{Ga}\,{}^{\circ}G_{Ga}^l + y_{GaSe}\,{}^{\circ}G_{GaSe}^l + y_{Ga_2Se_3}\,{}^{\circ}G_{Ga_2Se_3}^l + y_{Se}\,{}^{\circ}G_{Se}^l \tag{6.30}$$

where y_i refers to the site fractions of species i, $y_{Ga} + y_{GaSe} + y_{Ga_2Se_3} + y_{Se} = 1$. The terms $^{\circ}G_i^l$ represent the standard Gibbs energies of the liquid phases of species i. The ideal mixing Gibbs energy $^{id}G^l$ is expressed as:

$$^{id}G^l = RT(y_{Ga}\ln y_{Ga} + y_{GaSe}\ln y_{GaSe} + y_{Ga_2Se_3}\ln y_{Ga_2Se_3} + y_{Se}\ln y_{Se}) \tag{6.31}$$

The excess Gibbs energy $^{E}G^l$ is represented by the following formula:

$$\begin{aligned}
^{E}G^l &= y_{Ga}y_{GaSe}({}^{0}L_{Ga,GaSe}^l + {}^{1}L_{Ga,GaSe}^l(y_{Ga} - y_{GaSe})) + y_{GaSe}y_{Ga_2Se_3}\,{}^{0}L_{GaSeGa_2Se_3}^l \\
&\quad + y_{Ga_2Se_3}y_{Se}({}^{0}L_{Ga_2Se_3,Se}^l + {}^{1}L_{Ga_2Se_3,Se}^l(y_{Ga_2Se_3} - y_{Se}))
\end{aligned} \tag{6.32}$$

where L is the interaction parameter between the species to be optimized in the present work. L is considered as the linear function of the absolute temperature T or temperature independent.

Ordered Nonstoichiometric Compound Phase

The high temperature modification of Ga_2Se_3, α-Ga_2Se_3, is related to the zincblende structure with the space group $F\bar{4}3m$. In this structure, Ga and Se atoms occupy different sites, and a third of the metal sites are unoccupied [105], [106]. Based on this structure, the α-Ga_2Se_3 phase is described by the sublattice model developed by Hillert [146], and Sundman [147] with two sublattices after the formula:

$$(Ga,Va)_2(Se,Va)_3 \tag{6.33}$$

where Va represents vacancy. Considering the formation of vacancy in the sublattice occupied by Se is just for the convenience of the modeling of the Gibbs energy, which does not mean that the Se sublattice should contain considerable vacancies. From the assessment results of this work, it will be found that the vacancy in the Se sublattice is very small, which is in good agreement with the structural information.

The Gibbs energy of α-Ga_2Se_3 can also be expressed by equation (6.29) (where l should be replaced by α-Ga_2Se_3, which is abbreviated as α hereafter) with,

$$^{ref}G^\alpha = y'_{Ga} y''_{Se} \, ^\circ G^\alpha_{Ga:Se} + y'_{Ga} y''_{Va} \, ^\circ G^\alpha_{Ga:Va} + y'_{Va} y''_{Se} \, ^\circ G^\alpha_{Va:Se} \tag{6.34}$$

$$^{id}G^\alpha = RT[2(y'_{Ga} \ln y'_{Ga} + y'_{Va} \ln y'_{Va}) + 3(y''_{Se} \ln y''_{Se} + y''_{Va} \ln y''_{Va})] \tag{6.35}$$

$$\begin{aligned}
^EG^\alpha = y'_{Ga} y'_{Va} \Big[y''_{Se} \left({^0L^\alpha_{Ga,Va:Se}} + {^1L^\alpha_{Ga,Va:Se}} (y'_{Ga} - y'_{Va}) \right) \\
+ y''_{Va} \left({^0L^\alpha_{Ga,Va:Va}} + {^1L^\alpha_{Ga,Va:Va}} (y'_{Ga} - y'_{Va}) \right) \Big] \\
+ y''_{Se} y'_{Va} \left(y'_{Cu} \, {^0L^\alpha_{Cu:Se,Va}} + y'_{Va} \, {^0L^\alpha_{Va:Se,Va}} \right)
\end{aligned} \tag{6.36}$$

where $y_i^{'}$ and $y_i^{''}$ refer to the site fractions of the component i in the first and second sublattice, respectively. $°G_{Ga:Se}^{\alpha}$ is the standard Gibbs energy of the stoichiometric α-Ga_2Se_3. $°G_{Ga:Va}^{\alpha}$ and $°G_{Va:Se}^{\alpha}$ are expressed as:

$$°G_{Ga:Va}^{\alpha} = 2°G_{Ga}^{ort} + a_1 + b_1T \tag{6.37}$$

$$°G_{Va:Se}^{\alpha} = 3°G_{Se}^{tri} + a_2 + b_2T \tag{6.38}$$

where, $°G_{Ga}^{ort}$ is the standard Gibbs energy of pure Ga in orthorhombic phase; $°G_{Se}^{tri}$ is the standard Gibbs energy of pure Se in trigonal phase. a_i and b_i are the parameters should be optimized. To reduce the parameters, the following relations are used in the optimization [148]:

$$
\begin{aligned}
{}^0L_{Ga,Va:Se}^{\alpha} &= {}^0L_{Ga,Va:Va}^{\alpha} = {}^0L_{Ga,Va:*}^{\alpha} \\
{}^0L_{Ga:Se,Va}^{\alpha} &= {}^0L_{Va:Se,Va}^{\alpha} = {}^0L_{*:Se,Va}^{\alpha} \\
{}^1L_{Ga,Va:Se}^{\alpha} &= {}^1L_{Ga,Va:Va}^{\alpha} = {}^1L_{Ga,Va:*}^{\alpha}
\end{aligned}
\tag{6.39}
$$

Optimization Procedure

A selected set of thermodynamic and phase diagram data (listed in Table 6.9) are used for the optimization of thermodynamic model parameters of all phases in this system. The optimization procedure is performed by using the PARROT module of the Thermo-Calc program package [149].

First, the Gibbs energy coefficients of the stoichiometric α-Ga_2Se_3, liquid Ga_2Se_3, and liquid GaSe are deduced based on enthalpy of transition, transition temperature, melting enthalpy, and melting point data. Then, assuming that α-Ga_2Se_3 is a stoichiometric phase and there is no interaction between the pure elements in the liquid phase, a rough optimization of the liquid coefficients is performed based on the activities

of selenium, miscibility gap, and three-phase equilibrium. Third, fixing the coefficients of the liquid phase, the coefficients of the ordered nonstoichiometric α-Ga_2Se_3 phase are roughly optimized. Finally, all parameters of the phases are optimized to fit the experimental data listed in Table 6.9 as close as possible.

Results and Discussion

The optimized parameters of the liquid and α-Ga_2Se_3 phases in the Ga-Se system are listed in Table 6.10. The parameters taken from [145], [143], [144], [1] are not reproduced in Table 6.10 to conserve space. The phase diagram and thermodynamic properties of this system have been calculated by using the optimized parameters, which were performed with the Poly-3 module of the Thermo-Calc program package.

The calculated phase diagram is shown in Figure 6.9. Figures 6.10 to 6.12 show the comparison between the calculated phase diagram and measured data. The calculated phase diagram agrees with most of the measured data, but the Se-rich liquidus data measured by [105] are much higher than the calculated and other measured ones. The thermal effects below the melting temperature of Se at the Se-rich side may correspond to the glass transition or crystallization of Se [105], [102]. These transitions have not been considered in this optimization. Table 6.11 presents the experimental and calculated temperatures and compositions of the invariant reactions in this system. The calculated values agree well with the measured data except the reactions related with the transition between α-Ga_2Se_3 and β-Ga_2Se_3. A considerable discrepancy exists among the measured temperatures of the polymorphic transition between α-Ga_2Se_3 and β-Ga_2Se_3. The value measured by [106] is 35 K lower than those measured by [102] and [114]. In the present work, Dieleman`s [106] value is adopted, as Dieleman [106] measured various reactions

related with the transitions among the polymorphisms of Ga_2Se_3 by several methods in details. Table 6.12 shows the experimental and calculated standard enthalpies of formation of the intermediate phases, GaSe and β-Ga_2Se_3. The values disagree with each other. In this work, the evaluated values from [145] and [144] are adopted.

Conclusion

The thermodynamic data and phase diagram of GaSe system were critically investigated. Solid oxide electrochemical cells were used to measure the liquid phase a_{Se} along Ga-rich liquidus line of the phase diagram. The chemical potential of selenium in liquid phase was calculated in the temperature range 800 to 1000K. Invariant phase transition temperatures were measured and transition enthalpies were calculated from the EMF measurements. From structural phase transition measurements and XRD results along with third law analysis, a self consistent thermodynamic data set was obtained. A thermodynamic description of the Ga-Se binary system was obtained by the optimization of the available phase equilibrium and thermodynamic data. The associated and sublattice models are used to represent the Gibbs energy of the liquid and α-Ga_2Se_3 phases, respectively. The phase diagram and thermodynamic properties of this system have been calculated based on the optimized model parameters. A reasonable agreement between the model-calculated values and the phase equilibrium and thermodynamic data available in the literature was achieved.
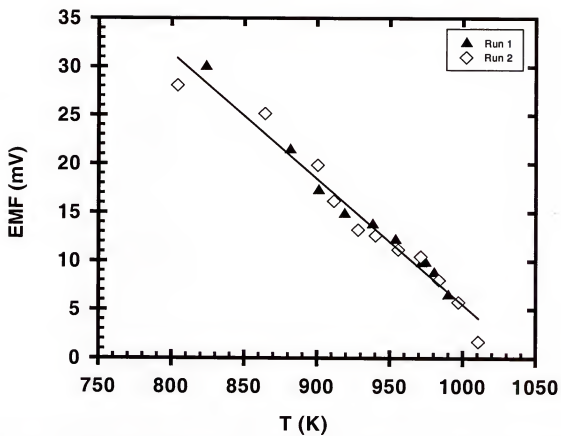
Figure 6.1 Temperature dependence of the EMF of cell I for the 15 at. % Se composition.
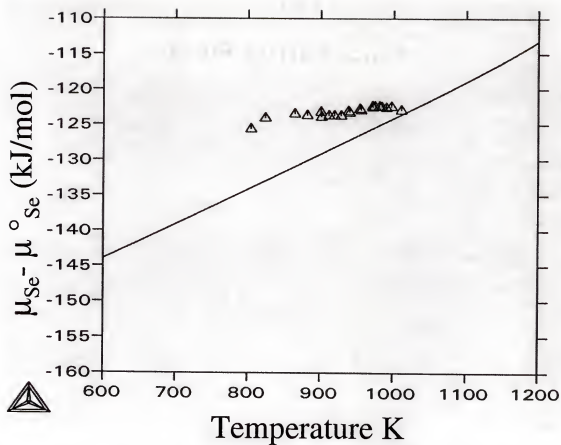
Figure 6.2 Comparison of the measured and optimized Se chemical potentials for 15 at. % Se sample.
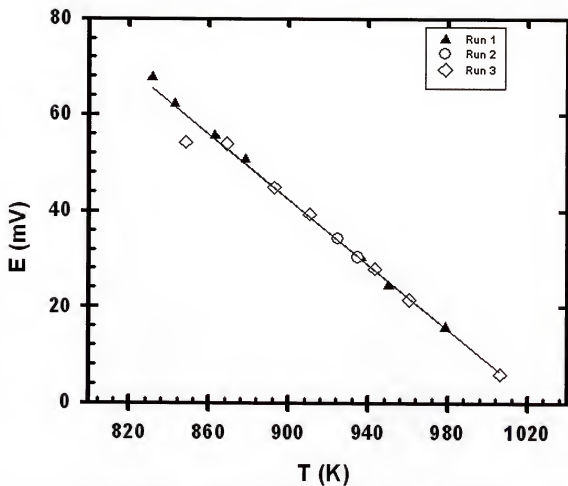
Figure 6.3 Temperature dependence of the EMF of cell I for 35 at.% Se composition.
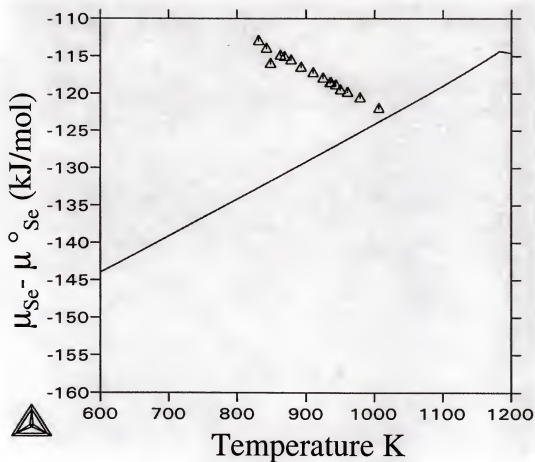
Figure 6.4 Comparison of the measured and optimized chemical potentials for 35 at. % Se sample
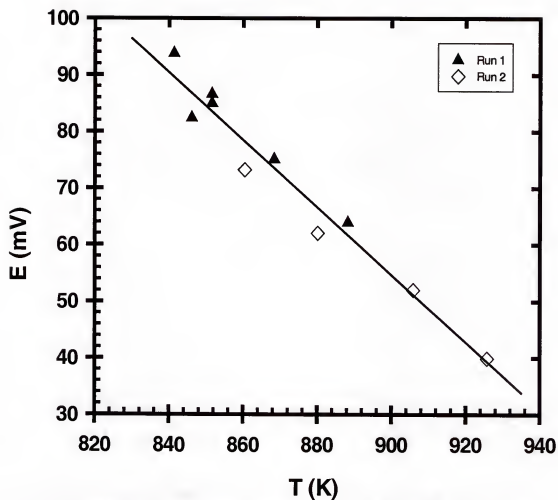
Figure 6.5. Temperature dependence of the EMF of cell I for 45 at. % Se composition.
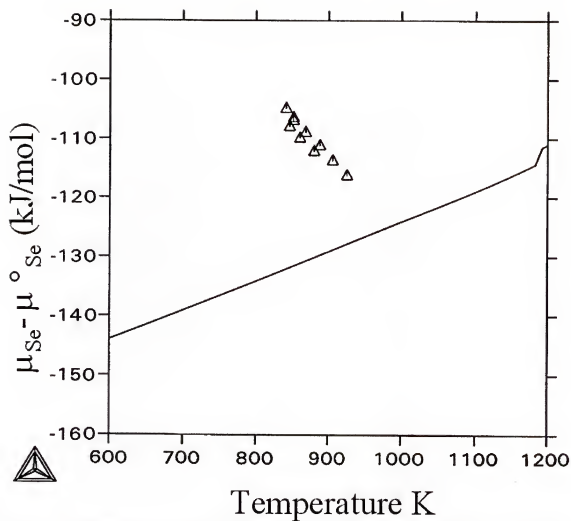
Figure 6.6 Comparison of the measured and optimized chemical potentials for 45 at. % Se sample.
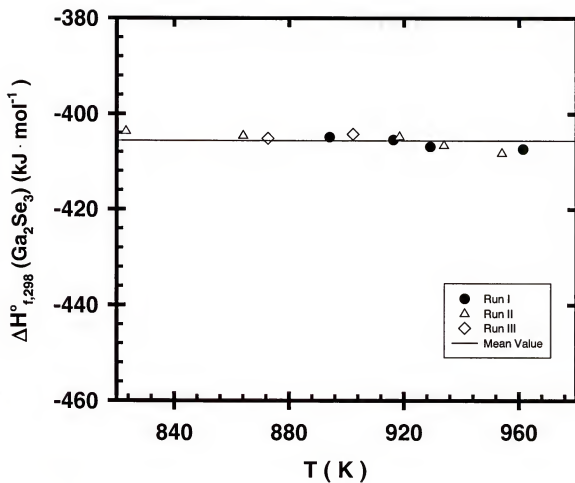
Figure 6.7 Third law treatment of standard enthalpy of formation of $Ga_2Se_3(\alpha)$.
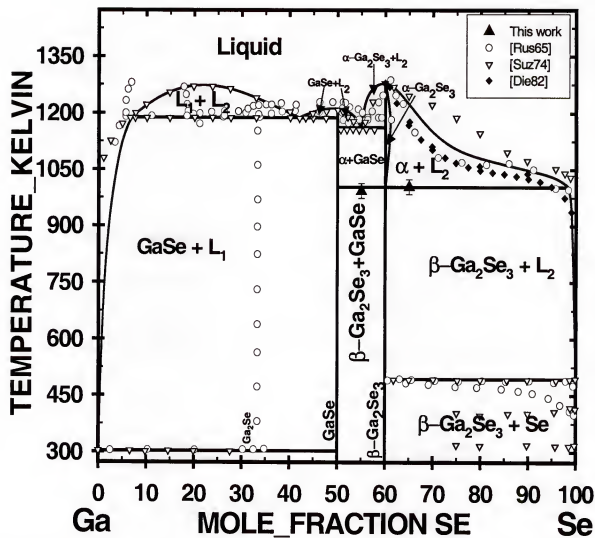
Figure 6.8 Evaluated phase diagram for Ga-Se system with EMF results and other experimental data.
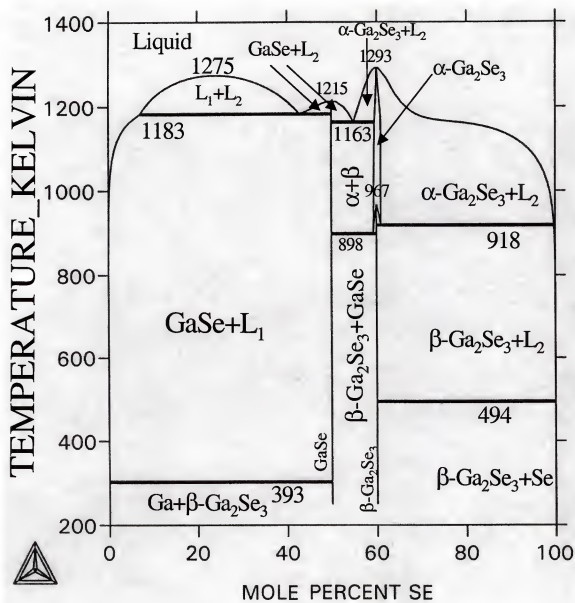
Figure 6.9 Calculated phase diagram of the Ga-Se system.
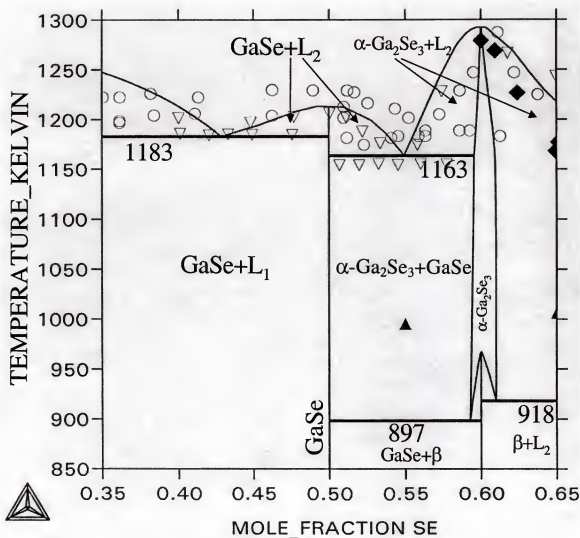
Figure 6.10 Comparison between the calculated Ga-Se phase diagram and various experimental data from 0.35 to 0.65 mole fraction of Se.
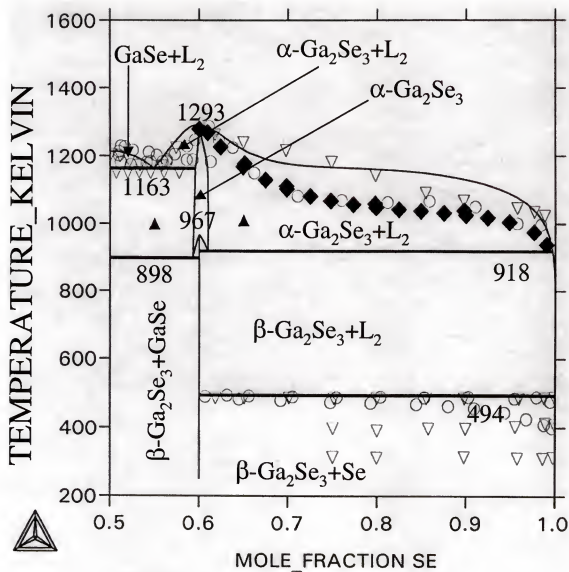
Figure 6.11 Calculated phase diagram section of Ga-Se in the vicinity of α-Ga₂Se₃, β-Ga₂Se₃ monotectic reactions.
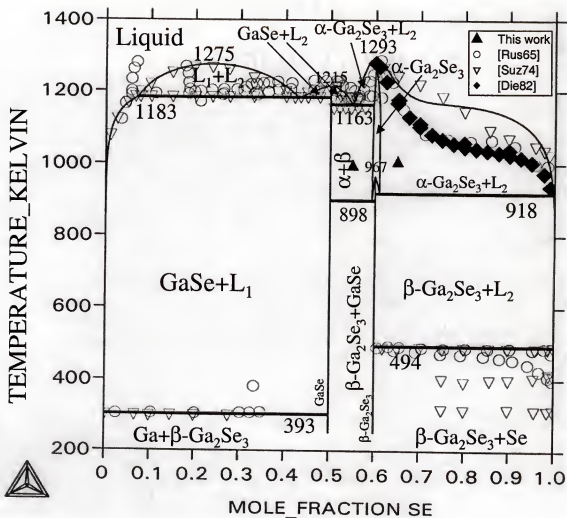
Figure 6.12 Comparison of the calculated Ga-Se phase diagram with various experimental data.

Table 6.1 EMF data for cell I (15 at% Se)

Run	T (K)	E (mV)	T (K)	E (mV)
1	971.75	9.76	990.15	6.44
	823.75	29.99	881.65	21.40
	901.25	17.24	918.95	14.83
	938.25	13.74	953.95	12.15
	974.45	9.82	980.45	8.75
2	997.05	5.75	1010.65	1.69
	864.25	25.12	803.95	28.07
	900.45	19.82	911.45	16.16
	928.15	13.20	940.15	12.62
	955.75	11.17	971.15	10.45
	983.65	8.02		

Table 6.2 EMF results for cell I (35 at% Se)

Run	T (K)	E (mV)	T (K)	E (mV)
1	831.25	67.62	842.55	62.20
	862.75	55.56	878.15	50.75
	924.85	34.30	934.74	30.40
	936.25	30.32	950.15	24.46
	978.75	15.76		
2	848.35	54.23	892.75	44.83
	868.85	53.90	910.45	39.34
	943.35	27.92	960.45	21.52
	1006.15	6.00		

Table 6.3 EMF results for cell I (45 at% Se)

Run	T (K)	E (mV)	T (K)	E (mV)
1	841.35	93.80	851.55	86.60
	868.35	75.10	888.25	63.90
	851.55	85.00	846.15	82.40
2	905.85	54.90	896.15	56.46
	919.95	43.23	945.15	34.22
	973.25	20.85	998.25	20.79

Table 6.4. Experimental results for the cell II (55 at% Se)

Run	T (K)	E (mV)	T (K)	E (mV)
		(α Ga$_2$Se$_3$)		
1	894.15	172.60	916.35	166.90
	929.15	159.90	961.45	153.30
2	823.15	190.00	863.95	178.90
	918.45	168.80	933.85	160.60
	954.05	151.40		
3	872.65	175.50	902.25	173.40
		(β Ga$_2$Se$_3$)		
1	985.55	150.70	1070.15	118.20
2	1088.95	115.40	1012.15	134.70
3	1013.25	136.00	1038.05	130.00
	1056.65	121.80	1100.25	107.80

Table 6.5 Experimental results for the cell III (65 at% Se)

Run	T(K)	E(mV)	T(K)	E(mV)
		(α Ga$_2$Se$_3$)		
1	941.05	210.5	953.45	210.9
2	918.25	233.0	977.75	203.7
		(β Ga$_2$Se$_3$)		
1	1014.55	184.3	1040.85	172.6
	1096.45	155.7	1107.05	150.6
2	994.45	194.6	1016.45	185.1
	1031.45	179.6	1044.25	171.6
	1062.15	165.4	1073.75	161.6
	1123.15	150.2		

Table 6.6 Least Squares EMF expressions of Ga from cell I, cell II, and cell III:

C,W, Ga(l), $Ga_2O_3(s)$ // YSZ // $Ga_2O_3(s)$, GaSe(s), Liquid, C,W   cell I ($0 < x_{se} < 0.5$)

C,W, Ga(l), $Ga_2O_3(s)$ // YSZ // $Ga_2O_3(s)$, GaSe(s), $Ga_2Se_3(s)$, C,W   cell II ($x_{se} = 0.55$)

C,W, Ga(l), $Ga_2O_3(s)$ // YSZ // $Ga_2O_3(s)$, $Ga_2Se_3(s)$, Liquid, C,W   cell III ($x_{se} = 0.65$)

at. % Se	EMF Expressions A+ BT (K)		T Range (K)	Precision ± mV
	A	B		
15	134.98	-0.1295	804-1011	-
35	347.30	-0.3389	831-998	-
45	493.21	-0.4842	840-998	-
55 (α-Ga_2Se_3)	417.27	-0.27477	823-962	2.32
55 (β-Ga_2Se_3)	476.63	-0.33454	986-1100	2.25
65 (α-Ga_2Se_3)	657.40	-0.46735	918-978	4.59
65 (β-Ga_2Se_3)	544.06	-0.35446	995-1123	2.17

Table 6.7 Comparison of the standard enthalpy of formation and absolute entropy of α-Ga_2Se_3.

Sr. No	$-\Delta H^o_{f, 298}$ (kJ mol^{-1})	Ref.	S^o_{298}	Ref.
1	368.6	[111]	179.9	[142]
2	439.3	[112]	98.6	This Work
3	460.2	[112]		
4	339.7	[113]*		
5	356.1	[113]+		
6	408.8	[142]		
7	405.6	This Work		

* calculated using Ref. [112]
+ calculated using Ref. [111]

Table 6.8 Lattice structures of the compounds in the Ga-Se System.

Compound	Crystal System	Lattice Parameter (Å)	E_g (eV)	Reference
GaSe	hexagonal several polytypes β:D^4_{6h} – P6$_3$/mmc γ:C^5_{3v} - R3m δ:C^4_{6v} - P6$_3$/mc ε:D^1_{3h} - P6m2	a=3.755 c=16-34 (depending on polytypes	$E_{g,direct}$=2.1275 $E_{g,indirect}$=2.103 (5.2K) $E_{g,direct}$=2.1021 (300K)	[115]
	ε-GaSe	a=3.775 c=15.94	$E_{g,direct}$=2.02 (300K)	[132]
	hexagonal($\varepsilon\beta$), trigonal(γ)	a=3.755, c=15.94		[150], [129]
			2.0 (298K)	[136]
			1.98 (298K)	[151]
	hexagonal	a=3.759 c=16.02		[105]
		a=3.74 c=15.92		[152]
		a=3.752 c=15.95		[153]
Ga$_2$Se$_3$	cubic	a=5.444		[105]
		a=5.420		[154]
		a=5.429		[155]
		a=5.446		[105]
		a=5.429		[134]
	zincblende	a=5.426 (sharp component) a=5.453 (broad component)		[125], [156]
		a$_{mean}$(rest)=5.445 ±0.002		[106]
α-Ga$_2$Se$_3$	monoclinic	a=6.6608 b=11.6516 c=6.6449		[122]
	tetragonal	a=7.760 b=11.640 c=10.822		[157]
	orthorhombic	a=7.760 b=11.640 c=10.822		[158], [159], [160]

Table 6.10 Optimized parameters according to the analytical description of the phases[+]

Phase	Parameters
Liquid	$^{\circ}G^{l}_{Ga_2Se_3} = {}^{\circ}G^{\beta}_{Ga_2Se_3} + 101190 - 78.8567T$
	$^{\circ}G^{l}_{GaSe} = {}^{\circ}G^{l}_{GaSe} + 56000 - 45.2592T$
	$^{0}L^{l}_{Ga,GaSe} = 113628 - 76.4409T$
	$^{1}L^{l}_{Ga,GaSe} = 7654$
	$^{0}L^{l}_{GaSe,Ga_2Se_3} = -1151$
	$^{0}L^{l}_{Ga_2Se_3,Se} = 42407 - 35T$
	$^{1}L^{l}_{Ga_2Se_3,Se} = -14239$
α-Ga$_2$Se$_3$	$^{\circ}G^{\alpha}_{Ga:Se} = {}^{\circ}G^{\beta}_{Ga_2Se_3} + 17190 - 17.758264T$
	$^{\circ}G^{\alpha}_{Ga:Va} = 2{}^{\circ}G^{ort}_{Ga} + 338398 + 230T$
	$^{\circ}G^{\alpha}_{Va:Se} = 3{}^{\circ}G^{tri}_{Se} + 130000$
	$^{0}L^{\alpha}_{*,Se,Va} = -629518$
	$^{0}L^{\alpha}_{Ga,Va:*} = -88127$
	$^{1}L^{\alpha}_{Ga,Va:*} = -23907$

+ Temperature (T) is in Kelvin. The Gibbs energy of the liquid phase is in J/mole of atoms. The Gibbs energy of αGa$_2$Se$_3$ is in J/mole of Ga$_2$Se$_3$. The symbol * indicates Ga, Se or Va. tri is the abbreviation of trigonal, and ort is that of orthorhombic.

β′-Ga$_2$Se$_3$ (metastable phase of zincblende by fast quenching) by		a$_o$(oct.)=5.435 a$_{mean}$(rest)=5.435		[161]
		a(even)=5.411 ±0.001		[158], [159], [160]
		a(odd)=5.44		
		a$_o$=5.446±0.005		[162]
		a$_o$(oct.)=5.433 ±0.001		[106]
β-Ga$_2$Se$_3$		a$_o$(oct.)=5.418 ±0.001		[106]
		a(even)=5.416 ±0.002		[158], [159], [160]
		a(odd)=5.43		
		a$_{mean}$=5.418 ±0.005		[155]
		a$_o$(oct.)=5.418 ±0.001		[106]
γ-Ga$_2$Se$_3$		a$_o$=5.463±0.003		[158], [159], [160]
		a$_o$=5.4595±0.0005		[106]

Table 6.9 Data sources used during the optimization

Equilibrium/Function	Reference
Phase equilibrium data	[108], [107], [105], [102], [114], [106]
Vapor pressure data	[121]
Standard Gibbs energies of pure substances	[145], [143], [144], [1]
Enthalpy of melting	[106]

Table 6.11 Experimental and calculated temperatures and compositions of the invariant reactions in the Ga-Se system.

Phases	Composition, at. % Se	Temperature [K]	Reaction Type	Reference
L_1/L_2	~23/~23	1268	Critical	[105]
	~24.3/~24.3	1279		[102]
	~24/~24	1267		[106]
	23.9/23.9	**1275**		**This work**
$L_1/L_2/GaSe$	5.5/44/50	1188	Monotectic	[105]
	8.2/42/50	1187		[102]
	7.5/45.5/50	1190		[106]
	7.1/42.9/50	**1183**		**This work**
$Ga/L_1/GaSe$	0/0/50	303	Eutectic (or peritectic)	[108]
	0/0/50	303		[105]
	0/0/50	303		[102]
	0/0/50	303		[106]
	0/0/50	**303**		**This work**
$GaSe/L_2$	50/50	1233	Congruent	[108]
	50/50	1223		[158]
	50/50	1211		[107]
	50/50	1211		[105]
	50/50	1218		[102]
	50/50	1210		[106]
	50/50	**1215**		**This work**
$GaSe/L_2/\alpha-Ga_2Se_3$	50/55.0/60	1185	Eutectic (or peritectic)	[108]
	50/55.1/59.4	1160		[107]
	50/55.0/60	1157		[105]
	50/55.0/60	1163		[102]
	50/55.1/-	1153		[114]
	59/55.1/-	1162		[106]
	50/54.9/59.5	**1163**		**This work**
$\alpha-Ga_2Se_3/L_2$	60/60	1293	Congruent	[108]
	60/60	1283		[158]
	60/60	1283		[107]
	60/60	1278		[105]
	60/60	1283		[102]
	60/60	1283		[114]
	60/60	1280		[106]
	60/60	**1292**		**This work**
$GaSe/\alpha-Ga_2Se_3/\beta-Ga_2Se_3$	50/~59.9/~60.2	898	Eutectoid	[106]
	50/59.3/60	**898**		**This work**
$\beta-Ga_2Se_3/\alpha-Ga_2Se_3$	60/60	1003	Polymorphic	[102]
	60/60	1003		[114]

	60.5/60.5	968		[106]
	60.0/60.0	**967**		**This work**
β-Ga$_2$Se$_3$/α-Ga$_2$Se$_3$/L$_2$	~60.7/61/-	918	Peritectic	[106]
	60/61.0/99.1	**918**		**This work**
β-Ga$_2$Se$_3$ /Se/L$_3$	60/100/100	493	Eutectic (or	[108]
	60/100/100	493	peritectic)	[105]
	60/100/100	493		[102]
	60/100/100	**494**		**This work**

Table 6.12 Experimental and calculated standard enthalpies of formation ($\Delta H^{\circ}_{f,298}$) of the intermediate phases, GaSe and βGa$_2$Se$_3$ at 298.15 K in the Ga-Se system (kJ/mol)

Compound	$-\Delta H^{\circ}_{f,298}$	Method	Reference
GaSe	143.5	Unknown	[112]
	159.0	Evaluation	[144],This work
Ga$_2$Se$_3$	439.3	Combustion	[119]
	460.2	Combustion	[119]
	368.6	Calorimetry	[118]
	355.6	Estimation	[113]
	405.9	Evaluation	[145],This work

THERMOCHEMISTRY AND GIBBS ENERGY ASSESSMENT OF CuGaSe$_2$

Introduction

The chalcopyrite ternary compounds CuGaSe$_2$ and CuInSe$_2$ show potential as alternative semiconductors for solar cell applications. The high absorption coefficient of visible light and direct band gap energy of 1.7 eV [163] for CuGaSe$_2$ and 1.0 eV [69],for CuInSe$_2$ [164] makes CIGS based solar cell applications one of the most popular and promising research fields in the area of photovoltaic power systems. The CIS based materials have already found commercial production with predictions of large market potential in near future. Although the most commercial units are usually produced in the poly-crystalline form with bulk production methods, the best efficiency solar cells can be made up of combination of a range of thin layers of semiconductors with improved light absorbance and electrical properties. The thin film process is advantageous in terms of cost efficiency and flexibility in substrate materials and geometrical configuration as well as the capability of in-situ process control. The gallium, sodium and sulfur addition in the structure of CIS based solar cell materials enables to adjust band gap energy as well as other electronic properties of semiconducting layers such as defect chemistry and conductivity. It was experimentally proven that gallium addition increased the cell efficiencies of CIS based solar cells considerably.

The compound GuGaSe$_2$ was first synthesized by Hahn et al. [60]. A number of experimental studies on the phase relations of the Cu-Ga-Se system as well as the pseudo-binary section of Cu$_2$Se-Ga$_2$Se$_3$ system exist in the literature. Most of the

experimental data are from DTA and XRD measurements [114], [165]. A summary of thermochemistry and thermodynamic stability of the ternary compounds in the Cu-In-Se system was given in Chapter 5. The pseudo-binary sections of Cu_2Se-In_2Se_3 and Cu_2Se-Ga_2Se_3 systems show characteristic similarities; however, Cu-Ga-Se system is relatively less studied and considerable uncertainty still exists especially for selenium-rich sections of phase equilibria. The binary systems of Cu-Ga, Ga-Se and Cu-Se have already been assessed; however, the stability of ternary compounds and phase diagram along Cu_2Se, Ga_2Se_3 line have not been critically assessed. The unstable results of our preliminary EMF experiments performed for ternary compounds in Ga_2Se_3–rich composition ranges suggest that the pseudo-binary section may be analogous to CIS, which includes non-stoichiometric and large homogeneity range compounds. The instability may be explained by the occurrence of a ternary-liquid phase equilibrium along the pseudo-binary line between $Cu_xGa_ySe_z$ and GaSe, which is analogous to the observations during CIS experiments. There is not much experimental information on the equilibrium nature of ternary compounds with GaSe pseudo-binary line.

Phase diagram of Cu_2Se-Ga_2Se_3 shows similarities to the Cu_2Se-In_2Se_3 system. The $Cu_1Ga_5Se_8$ compound was reported in a few publications with various homogeneity ranges. Another large homogeneity range compound that can be represented as $Cu_1Ga_3Se_5$ formula similar to $Cu_1In_3Se_5$ is also reported. This phase is interpreted to be stable between 70 and 88 % mole Ga_2Se_3 compositions in the pseudo-binary section of Cu_2Se-Ga_2Se_3. However, the limits of these ternary compounds are not well described in the literature. In general, there is not much thermochemical data on these ternary compounds. Although a few phase diagram studies and attempts of clear determination

and assessment of X-Ray data on these ternary compounds exist, wide inconsistency between some phase diagrams with previous data especially of the pseudo-binary section of Cu_2Se-Ga_2Se_3 creates reasonable doubts considering the difficulties in distinguishing large homogeneity range compound X-Ray spectra with pertinent binaries.

There are no reports available in the literature on the thermodynamic properties of $CuGaSe_2$ except the standard enthalpy of formation, $\Delta H^o_{f,298}$ [100]. Hence, the present study has been undertaken to determine the thermodynamic stability of the $CuGaSe_2$ phase with the help of solid oxide electrolyte EMF method and the results will be compared with that of $CuInSe_2$.

Literature Review

The ternary $CuGaSe_2$ compound crystallizes in chalcopyrite structure and the phase diagram of Cu-Ga-Se systems shows many characteristic similarities with other chalcopyrite I-II-VI$_2$ compounds. One of the most extended phase diagram studies was reported by Mikkelsen [114]. The phase diagram of ternary Cu-Ga-Se system was studied by DTA and X-Ray measurements. In addition to two ternary solid solutions which lie at the two edges of Cu_2Se-Ga_2Se_3 pseudo binary line, only a chalcopyrite $CuGaSe_2$ solid solution was observed, which does not agree with some earlier interpretations of δ solid solution phase extending between 71 mol% to 89 mol% Ga_2Se_3. The liquidus was found to include two regions of liquid immiscibility, one which extends from the Cu-rich immiscibility originating from the Cu-Se binary to the Ga-rich immiscibility originating from the Ga-Se binary, and the other is related to the Se-rich immiscibility created by Cu-Se binary phase region. X-Ray powder diffraction patterns of samples quenched after an 850 °C anneal showed a single cubic phase with a non-linear decrease in lattice parameter

from 78-100 mol% Ga_2Se_3. This result was interpreted as the existence of no two-phase regions at 850 °C. It was stated that no reflection peaks were observed other than the peaks related to zincblende space group. However, it was also mentioned that three solid solutions were postulated for the analogous region of the Cu-Ga-S system although it was not supported by X-Ray analysis. The Ga_2Se_3-rich part of the constructed pseudo-binary phase diagram was described with zincblende solid solution; however, no detailed explanation for the large value of Cu_2Se solubility in Ga_2Se_3 phase was suggested.

Palatnik and Belova [165] studied the phase equilibria between 40 to 100 mol % Ga_2Se_3 along the pseudo-binary section of $Cu_2Se-Ga_2Se_3$. No phase relations for the Cu_2Se rich section are given. Numerous DTA data were interpreted to indicate that the chalcopyrite phase extended from 50 to 65 mol% Ga_2Se_3. A solid solution that is stable between 71 to 89 mol% Ga2Se3 was also reported. This compound, which was denoted by the symbol δ, can be represented by the chemical formula of $Cu_1Ga_3Se_5$ or $Cu_1Ga_5Se_8$. Another solid solution, which lies between 91 to 100 mol% Ga_2Se_3 is also reported, which is in disagreement with some of the earlier X-Ray diffraction results. This phase is specified by the symbol ϵ in the phase diagram.

Bodnar and Bologa [166] reported that $CuInSe_2$ and $CuGaSe_2$ referring to $A^I-B^{III}-C^{VI}$ compounds, crystallize in chalcopyrite structure and are analogues to $A^{II}-B^{VI}$ compounds. $CuInSe_2$ and $CuGaSe_2$ compounds and $CuIn_xGa_{1-x}Se_2$ solid solutions were synthesized from elements in double quartz ampoules in a vertical furnace. The compositions of the $CuInSe_2$ and $CuGaSe_2$ ternary compounds and the $CuIn_xGa_{1-x}Se_2$ solid solutions were tested by chemical analysis. The homogeneity and structure of the investigated compounds and solid solutions were determined by an X-Ray method. The

ternary compounds CuInSe$_2$ and CuGaSe$_2$ and the CuIn$_x$Ga$_{1-x}$Se$_2$ solid solutions were found to crystallize in chalcopyrite structure. The lattice parameters for CuInSe$_2$ (a=5.782 $\pm$ 0.002Å, c=11.620 $\pm$ 0.005Å) and CuGaSe$_2$ (a=5.616 $\pm$ 0.002Å, c=11.016$\pm$ 0.005Å) are found to be close. The phase transformation temperatures were determined from DTA measurements. Annealed alumina was used as reference material and both heating and cooling measurements were performed. The thermal investigations showed two thermal transformation points for each ternary compound. It was observed that CuGaSe$_2$ experienced phase transformations at 1045 and 1080 °C, and CuInSe$_2$ experienced at 810 and 986 °C. Complying phase transformations were also found for solid solutions over the whole composition range. Figure 7.1 summarizes the experimental data measured along CuInSe$_2$-CuGaSe$_2$ phase line. The phase transformation at 1045 °C for CuGaSe$_2$ was assumed to be related to cation-cation disordering by analogous assessment of Palatnik and Rogacheva [167] that was referred for the phase transformation of CuInSe$_2$ at 810 °C. The phase transformation temperature of 1045 °C is consistent with value of 1050$\pm$5 °C by the earlier report of Palatnik and Belova [165] which is represented by the peritectic phase reaction.
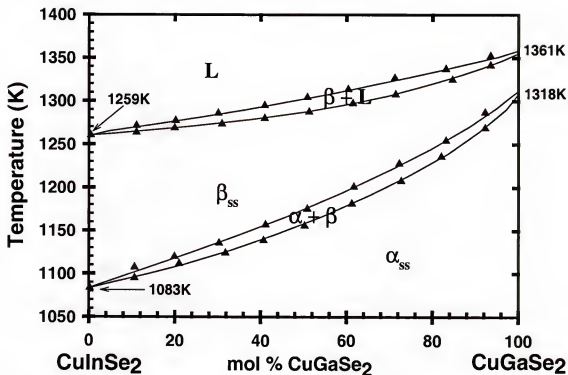
Figure 7.1 The phase diagram of CuInSe$_2$-CuGaSe$_2$ system by Bodnar [166]

Jitsukawa [168] investigated the pseudo-binary phase diagrams of Cu$_2$Se-CuGaSe$_2$ and CuSe-CuGaSe$_2$ systems for single, high quality crystal growth of CuGaSe$_2$. The single crystals were precipitated by solution Bridgman method with nearly stoichiometric compositions. By using differential thermal analysis (DTA) and X-Ray diffraction (XRD) and electron probe micro analyzer (EPMA), phase diagrams of Cu$_2$Se-CuGaSe$_2$ and CuSe-CuGaSe$_2$ pseudo-binary systems were constructed. Then the crystal growth of CuGaSe$_2$ was performed on the basis of measured phase diagram data. A better reaction path to grow large crystals was suggested to be by CuSe instead of Cu$_2$Se. A peritectic reaction temperature between sphalerite + liquid phase to chalcopyrite phase is found to be 1054 °C, which is in very good agreement with earlier results. The eutectic line was determined from DTA signal to be 996 °C. The eutectic line, peritectic

temperature and temperature of liquidus line are about 20 ºC higher than the data of

Mikkelsen [114]. In contrast, Palatnik and Belova [165] did not report a eutectic reaction

between liquid and chalcopyrite-CuGaSe$_2$+Cu$_2$Se(ss) and their composition at the

peritectic point also differs from the results of Jitsukawa [168]. The comparison of

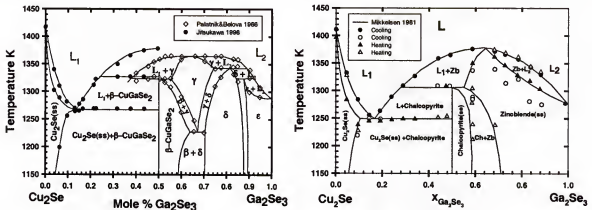various experimental data measured along the pseudo-binary of Cu$_2$Se-Ga$_2$Se$_3$ is given in

Figure 7.2.

Figure 7.2 The comparison of various experimental data along Cu$_2$Se-Ga$_2$Se$_3$ pseudo-binary.

Matsuhita [169] investigated the chemical reaction processes forming a single

phase in the CuIn$_x$Ga$_{1-x}$Se$_2$ system, as well as the intermediate products, using differential

thermal analysis (DTA) and powder X-Ray diffraction. The CuGaSe$_2$ (x=0) and CuInSe$_2$

(x=1) compounds showed phase transition points at 1060 and 815 ºC, which is also

consistent with the earlier reports.

A few reports were published for the effects of sodium on the efficiency of thin

film Cu(In,Ga)Se$_2$ solar cells. In general two assumptions are suggested for high solar

conversion efficiency of the solar cells fabricated by using soda-lime glass as a substrate:

first, the soda lime glass has better matching thermal expansion coefficient than other

glass substrates which helps better film growth, and second the sodium diffusion from the substrate improves the grain growth and electrical property of thin films. However, there is no general conclusion on how the diffusion mechanism influences the defect chemistry and defect structure or electrical properties.

Tanaka [170] investigated if the sodium effects also occur in the thin films containing In(Ga) rich layers on the surface of absorber layer of $Cu(In,Ga)Se_2$. Thin films of $Cu(In,Ga)_2Se_{3.5}$ were prepared by radio frequency sputtering from stoichiometric $CuIn_xGa_{1-x}Se_2$ (x=0.6) and Na_2Se mixture target. The X-Ray results showed that the lattice parameters of Cu:(In+Ga):Se=1:2:3.5 films were slightly smaller than that of $Cu(In,Ga)Se_2$. Besides the peaks appearing for chalcopyrite structure $Cu(In,Ga)Se_2$, an additional peak was observed. The similar sodium effects were found for In(Ga) rich thin films. The optical band gap of $Cu(In_{0.6}Ga_{0.4})Se_{3.5}$ thin film was found as 1.36 eV, which is larger than that of 1.24 eV. Both p and n type conduction were observed.

A few reports on the electrical and optical properties were published. Schroeder [171] studied hole transport and doping states in epitaxial $CuIn_{1-x}Ga_xSe_2$. The temperature dependent mobility, resistivity, and carrier concentration measurements were made on epitaxial grown single crystal thin films of $CuIn_{1-x}Ga_xSe_2$ by a hybrid sputtering and evaporation process on GaAs substrates. A general discussion for the relationship between defects and deviation from stoichiometric compositions was presented. It was suggested that the lack of dependence on the I/III for I/III-rich samples prove that electrically active defects may not be the ones that are responsible for deviations from stoichiometry in these materials.

Experimental

Materials and Synthesis

High purity Ga (99.9999 mass%, Johnson Matthey), Ga_2O_3 (99.99 mass%, Johnson Matthey), CuSe (purity better than 99.5 mass%, Johnson Matthey, USA), GaSe and Cu_2Se (purity greater than 99.99 mass%, Johnson Matthey, USA) were used as the starting materials. The ternary compound $CuGaSe_2$ was synthesized by heating a mixture of CuSe and GaSe stoichiometric 1:1 mole ratio in a silica ampoule sealed under a rotary vacuum of the order of 1kPa. This silica ampoule was heat treated in stages at 973K for 94hr., 1353K for 71 hr., 1273K for 95 hr., 1073K for 47 hr., 973K for 44 hr., followed by annealing at 873K for 116 hr. This procedure was repeated twice to ensure the completeness of reaction as confirmed by powder X-Ray diffraction (XRD) within the 5 mass % limit of its detection of impurity phases. A mixture of $CuGaSe_2$ / Cu_2Se / Cu / Ga_2O_3 in equi-molar ratio was compacted into pellets and heated at 1000K in purified Argon to 24hrs. and followed by XRD analysis to verify their co-existence.

EMF Measurements

The following galvanic cell was studied over the range 818 to 1053K:

W, Ga(l), Ga_2O_3(s) // YSZ // Ga_2O_3(s), Cu_2Se(s), $CuGaSe_2$(s), Cu, C, W   I

where YSZ denotes 15 mass % yittria (Y_2O_3) stabilized zirconia (ZrO_2). High density graphite cups were used to contain the test electrode materials. The absence of asymmetric potentials due to the graphite cup was tested by measuring the symmetrical cell with identical Ga(l) / Ga_2O_3(s) electrodes. A nearly null EMF was measured over the range 800 to 1100K, thereby showing the absence of significant errors arising from asymmetric potentials. Purified Argon was used as a blanket gas for the electrodes of the cell. The equilibrium nature of the cell EMFs was verified from almost identical readings

(within the experimental scatter) even on varying the relative amounts of the four components as seen from the two batches of test electrodes. The reversibility of the EMF readings was ascertained by their reproducibility in thermal cycling as well as micro-polarization. Other experimental details are the same as published elsewhere[35], [172].

Results and Discussion

The EMF results of $CuGaSe_2$ experiments showed similar behavior with $CuInSe_2$ experiments. After 600 °C, the stability of measurements was greatly diminished although this temperature lies in the working temperature range of solid electrolyte. According to the overall cell reaction in the test electrode, $Cu+CuGaSe_2$ coexistence as a product of half cell reactions was assumed. However, there is no phase diagram or stability information on the $Cu-CuGaSe_2$ system except Cu-Ga-Se solid-liquid phase diagram assessment at 1000 °C. Analogous to $CuInSe_2$ ternary phase relations, Mikkelsen [114] presented Cu(ss)-$CuGaSe_2$ two phase region at lower temperatures; however, his data at 1000 °C shows no coexistence or equilibrium between the two phases. It is interpreted that $Cu-CuGaSe_2$ phase system may behave similarly to $Cu-CuInSe_2$ in terms of two phase coexistence which was stable only to 600 °C. After 600 °C the different solid solution and liquid equilibria are assumed to be stable which explains the unstable results of the stoichiometric range EMF experiments.

The EMF data on cell I from two independent series of measurements are listed in Table 7.1 and plotted in Figure 7.3. The least-squares expression for these values of EMF over the range of 818-1053K can be given as:

$$(EMF \pm 3.3) \quad (mV) \quad = 366.7 - 0.1824 \ T \ (K) \tag{7.1}$$
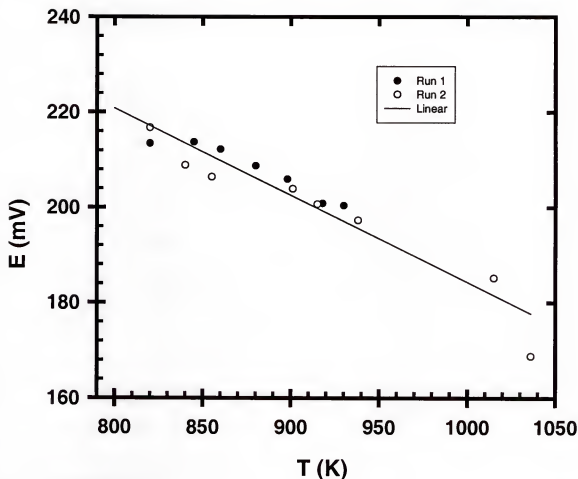
Figure 7.3 EMF results for cell I.

The two half-cell reactions of cell I can be represented as:

$$Ga(l) + 3/2 \; O^{2-} \leftrightarrow \frac{1}{2} \; Ga_2O_3(s) + 3 \; e^{-1} \tag{7.2a}$$

$$\frac{1}{2} \; Ga_2O_3(s) + 2Cu_2Se(ss) + 3 \; e^{-1} \leftrightarrow CuGaSe_2(s) + 3Cu(s) + 3/2 \; O^{2-} \tag{7.2b}$$

For the passage of 3 equivalent charge per mole of ternary compound, the over-all cell reaction could be represented as:

$$2Cu_2Se(ss) + Ga(l) \leftrightarrow CuGaSe_2(s) + 3Cu(s) \tag{7.3}$$
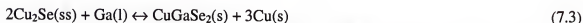
Thus, the standard Gibbs energy change for reaction given in Equation 7.3, ΔG_R yields the following expression:

$$\Delta G_R = \Delta G^o{}_f (CuGaSe_2,s) - 2 \, \Delta G^o{}_f (Cu_2Se,ss) \tag{7.4}$$

$$\Delta G_R \text{ (kJ/mol)} = 86.59 - 0.12341 \, T(K) \tag{7.5}$$

Cu-Se system was recently optimized by Chang [1]. In Chapter 5, the more recent value of the Gibbs energy function of $Cu_2Se(ss)$ was used. This function was obtained from a reassessment work by Shen [86]. From this data and combining with reference data for elements from Barin [85], the standard Gibbs energy of formation of Cu_2Se is calculated as

$$(\Delta G^o{}_f \, Cu_2Se,ss \,) \text{ (kJ/mol)} = -59.265 - 0.0053 \, T(K) \quad (853 \text{ to } 988K) \tag{7.6}$$

Substituting the Equation 7.5 and 7.6, the following expression for the standard Gibbs energy of formation of $CuGaSe_2$ is obtained:

$$(\Delta G^o{}_f \, CuGaSe_2) \text{ (kJ/mol)} = -224.67 + 0.0422 T(K) \tag{7.7}$$

In Chapter 5, the stability of $CuInSe_2$ using the co-existence mixture, Cu_2Se / $CuInSe_2$ / Cu / In_2O_3 was measured. Further, phase relations for the pseudo-binary line for Cu_2Se-In_2Se_3 were optimized and the Gibbs energy for stoichiometric α and δ-$CuInSe_2$ was calculated from the measured data. The expressions were 5.15 and 5.16 were given as:

$$G_{\alpha - CuInSe_2} = -0.2813 \, T(K) - 142.32 \text{ kJ/mol} \tag{5.15}$$

$$G_{\delta - CuInSe_2} = -0.2899 \, T(K) - 133.23 \text{ kJ/mol} \tag{5.16}$$

From combination of Equation 5.15 and 7.6, the following expression for the standard Gibbs energy of formation of α-$CuInSe_2$ can be derived.

$$(\Delta G^o{}_f \, \alpha\text{-}CuInSe_2 \,) \text{ (kJ/mol)} = -218.05 + 0.0439 \, T(K) \tag{7.8}$$

A comparison is made in Table 7.2 on the $\Delta G^o{}_f$ of $CuInSe_2$ and $CuGaSe_2$. For a better appreciation of the comparison, the same set of data is also plotted in Figure.7.4.

The Gibbs energy functions for $CuInSe_2$ and $CuGaSe_2$ are also plotted in Figure 7.5. The slope difference for the Gibbs formation energy curves between In and Ga ternaries in Figure 7.4 seem to be minimal. The ΔG^o_f values at 1000 K show that the ternary $CuGaSe_2$ compound is slightly more stable than the $CuInSe_2$ compound (8 kJ/mol), which is consistent with the current phase diagram information. Since there is not much data published on the Gibbs energy of $CuGaSe_2$ compound, a comparison with other data can not be made. It was observed that the range of errors during the EMF experiments widened for selenium rich compositions in all regions above 800K for both $CuInSe_2$ and $CuGaSe_2$ studies. For the stoichiometric $CuInSe_2$ and $CuGaSe_2$ experiments, complete stability in measurements was not achieved, which was partly due to selenium high vapor pressure and lack of equilibrium between the products of half cell reactions in the conductivity regions of solid electrolyte. The experiments were repeated many times for reproducibility; however, most of the time the fluctuation was observed and the results of some runs stretched out long ranges. Hence some of the measured data was eliminated based on the knowledge obtained from general trends of previous experiments.
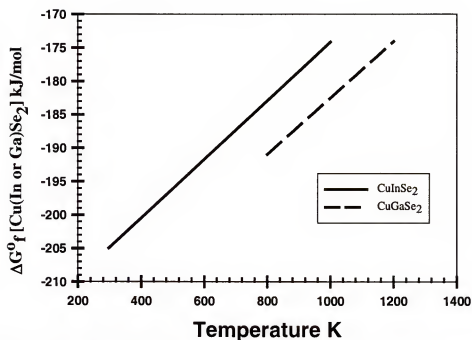
Figure 7.4 Standard Gibbs energy of formation of Cu(In or Ga)Se$_2$.

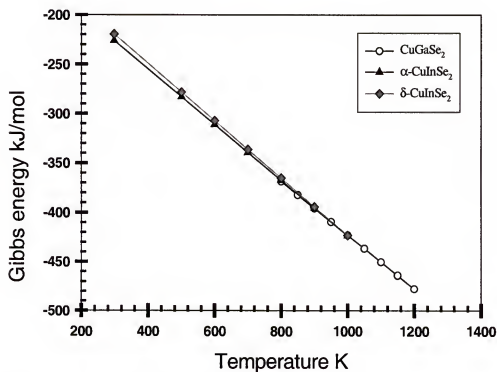Figure 7.5 Gibbs energy of Cu(In or Ga)Se$_2$ compounds.

No third-law analysis could be carried out on account of reliable S^o_{298} and C^o_P data on $CuGaSe_2$. Berger et al. [99] determined a value of 316.7 kJ/mol and 267.4 kJ/mol for $\Delta H^o_{f,298}$ of $CuGaSe_2$ and $CuInSe_2$ by Mass Spectrometry. And also Glazov et al [100] estimated the values of $\Delta H^o_{f,298}$ of both the ternary compounds by using modified version of the two equations mentioned in [173]. These values are compared in Table 7.3.

Table 7.1 EMF data for cell I

Run	T (K)	E (mV)	T (K)	E (mV)
1	820	213.444	898	205.953
	845	213.719	918	200.847
	860	212.242	930	200.406
	880	208.786		
2	820	216.714	938	197.311
	840	208.878	1015	185.213
	855	206.451	1036	168.845
	901	203.948		
	915	200.683		

Table 7.2 ΔG^{o}_{f} of ternary compounds of CuInSe$_2$ and CuGaSe$_2$

Compounds	ΔG^{o}_{f} (kJ mol^{-1}) A+ BT (K)		T Range (K)	ΔG^{o}_{f} (kJ mol^{-1}) at 1000 K	Ref.
	A	B			
CuInSe$_2$	-218.05	0.0439	949-1044	-174.15	This Work
CuGaSe$_2$	-224.67	0.0422	818-1053	-182.51	This Work

Table 7.3 Comparison of $\Delta H^{o}_{f,298}$ of CuGaSe$_2$ and CuInSe$_2$

Solid Phase	Method	$-\Delta H^{o}_{f,298}$ (kJ mol^{-1})	Reference
CuGaSe$_2$	Mass Spectrometry	316.7	[99]
	Calculated	324.7	[173]
	Calculated	295.8	[173]
CuInSe$_2$	Mass Spectrometry	267.4	[99]
	EMF	201.0	[This work]
	Calculated	260.2	[173]
	Calculated	268.6	[173]

Ga Activity Measurements in Cu-Ga Melts

The general characteristics of Cu-Ga binary phase equilibria are well established by Hansen [11], Kittl [174], and Subramanian [175]. Binary phase equilibria have most recently been assessed by Subramanian [175]. An earlier determination of enthalpy of mixing of liquid binary measurements by Predel and co-workers [176], [177] were used in Subramanian`s [175] calculations. The enthalpy data were combined with the excess mixing energies of the liquid Cu-Ga alloys at 1000K from Predel [176]. From this, the expression of excess entropy of mixing in the liquid phase was obtained. A general solution model that is analogous to general representation of Redlich-Kister model was used. The following excess Gibbs energy function was used by Subramanian`s [175]:

$$G^{ex} = x(1-x)[(H_o - S_o T) + (H_o - S_o T)x + (H_o - S_o T)x^2] \quad (j/mol) \qquad (7.9)$$

The optimized parameters by Subramanian [175] for solution phases are summarized in Table 7.4.

Table 7.4 Optimized excess Gibbs energy parameters for Cu-Ga system according the formula $G^{ex} = x(1-x)[(H_o - S_o T) + (H_o - S_o T)x + (H_o - S_o T)x^2]$ (J/mol) by Subramanian [175].

Phase	H_o	H_1	H_2	S_o	S_1	S_2
L	-72225	101296	-41045	-9.158	44.264	-41.045
α	-73684	63694	0	0	0	0
β	-77033	61058	0	8.281	-25.941	0
γ	15937	-507108	775218	21.859	-91.967	0
ζ	-72559	79484	0	7.812	0	0

The liquid phase for Cu and Ga elements were taken as the reference state. As a result, the pure element reference state Gibbs energy functions for solution phases, which were reported according to the formula G=A+BT, is given in Table 7.5.

Table 7.5 Lattice stability parameters reported by Subramanian [175] according to the formula G=A+BT (J/mol) for the Cu-Ga system.

Phase	A		B	
	Cu	Ga	Cu	Ga
L	0	0	0	0
α	-13054	5021	9.623	8.368
β	-9498	0	8.786	8.368
γ	-9498	0	8.786	8.368
ζ	-12427	-2092	10.878	11.381

In general, the calculated phase diagram and thermodynamic data by Subramanian [175] show reasonable agreement with the literature data. However, the Ga-rich section of the lower temperature region of phase diagram shows some discrepancy with the experimental results. The plotted phase equilibrium section does not reveal whole liquidus line sections above 70 Ga mol%. Hence, a new EMF experiment was designed to directly measure the Ga activity in the liquid phase. The results of these activity measurements are then combined with recent phase diagram information to verify the consistency of previous data assessments.

The optimization results of Subramanian [175] were re-organized in this study to calculate liquid activities and binary phase equilibria. The general Redlich-Kister model and its slight modifications were used to describe solution phases. In order for rational

comparison, the same values for reference states in solution phases and optimization parameters that correspond to pure elements Gibbs energy functions were adopted. The general Redlich-Kister representation for the solution phase excess Gibbs energy expressions with different number of coefficients were used: The adapted parameters, based on the formula of $G^{xs} = x_A x_B \sum_{i=0}^{n} K_i (x_A - x_B)^i$, are given in Table 7.6.

Table 7.6. Adapted thermodynamic parameters of Subramanian [175] according to the Redlich-Kister model $G^{xs} = x_A x_B \sum_{i=0}^{n} K_i (x_A - x_B)^i$ (J/mol).

Phase	K_o	K_1	K_2
Liquid	-31838.3-2.71275*T	-30125.5+1.6095*T	-10261.3+10.2613*T
α	-41837	-31847	0
β	-46504+4.6895*T	-30529-12.9705*T	0
γ	-43812.5+24.1245*T	-134055-45.9835*T	193804.5
ζ	-32817-7.812*T	-39742	0

Experimental

Materials and Synthesis

High purity Ga (99.9999 mass%, Alfa Aesar), gallium (III) oxide (Ga_2O_3) (99.99 mass%, Alfa Aesar), and Cu powder (purity better than 99.999 mass%, Puratronic), were used as the starting materials. Three different Cu-Ga compositions were prepared by grinding mixtures of Cu and Ga elements. The ground samples were placed in alumina crucibles, which were also placed inside quartz ampoules. The quartz ampoules were then sealed under vacuum on the order of 10 Pa. The alumina crucibles were used to prevent

quartz ampoule breaking inside the furnace during the heat treatment. The 60 , 90 and 99 at. % Ga samples were heated to 900 °C (1200K) for 92 hours. The samples of 60 and 90 at. % Ga were annealed at 800 °C for 31 hr. The 99 atomic % Ga was annealed at 350 °C for 90 hr. The samples were then slowly cooled to room temperature. The reference electrode materials were prepared from the mixture of Ga and Ga_2O_3 according to 4/1 weight ratio. The test electrode materials were prepared by mixing the annealed samples with Ga_2O_3 powder with the same weight ratio.
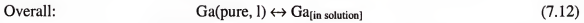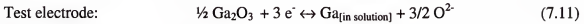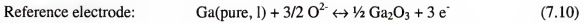
EMF Measurements

The following galvanic cell was studied over the range 800 to 1100 K.

W, Ga(l), Ga_2O_3(s) // YSZ // Ga_2O_3(s), Cu-Ga(l), C, W   II

where YSZ denotes 15 mass % yittria (Y_2O_3) stabilized zirconia (ZrO_2). High density graphite cups were used to contain the test electrode materials. The absence of asymmetric potentials due to the graphite cup was tested by measuring the symmetrical cell with identical Ga(l)/Ga_2O_3(s) electrodes. Nearly null EMF was measured over the range 800 to 1100K, thereby showing the absence of significant errors arising from asymmetric potentials. Purified Argon was used as a blanket gas for the electrodes of the cell. The equilibrium nature of the cell EMFs was verified from almost identical readings even on varying the relative amounts of the four components as seen from the two batches of test electrodes. The reversibility of the EMF readings was ascertained by their reproducibility in thermal cycling as well as micro-polarization.

Results and Discussion

The electrochemical half-cell reactions for cell II, which was employed for the liquid phase activity measurements can be represented schematically as:

Reference electrode: $Ga(pure, l) + 3/2\ O^{2-} \leftrightarrow \frac{1}{2}\ Ga_2O_3 + 3\ e^-$ (7.10)

Test electrode: $\frac{1}{2}\ Ga_2O_3 + 3\ e^- \leftrightarrow Ga_{[in\ solution]} + 3/2\ O^{2-}$ (7.11)

Overall: $Ga(pure, l) \leftrightarrow Ga_{[in\ solution]}$ (7.12)

where $Ga_{[pure,\ l]}$ and $Ga_{[in\ solution]}$ represent the pure liquid gallium and gallium in the Se-rich liquid phase.

Applying first and second laws of thermodynamics for a reversible electrochemical cell, the Gibbs energy change of the system by passing 3 equivalent of electrical charge, which is equal to the reversible electrical work done on the system, can be represented by the following expression:

$$\Delta G_R = -3FE = \Delta G_R^o + RT\ \ln \frac{a_{Ga_{[in\ solution]}}}{a_{Ga(pure,\ l)}}$$ (7.13)

If pure liquid Ga was chosen as the reference state, then the activity of Ga in Se-rich liquid could be represented by the following expression:

$$a_{Ga[in\ solution]} = \exp[(-3FE)/RT]$$ (7.14)

EMF and activity curves are given in Figure 7.6 and Figure 7.8 for cell I with 90 at. % Ga sample, respectively. Figures 7.7, and 7.9 show the experimental data and activity curve for 99 at. % Ga composition correspondingly. The samples with 60 % Ga composition did not stable measurements of the EMF and they are not be included here. The reason for those unstable measurements thought to be a result of a problem in the Argon purification system. The measurements for 90 and 99 Ga mol % samples also showed a lot of fluctuation; however, the sample points with very large discrepancy were eliminated by repeating the runs and comparing the general trend of EMF data. The

results for activity measurements given in Figures 7.8 and 7.9 reveal good agreement with the recent assessment by Subramanian [175].
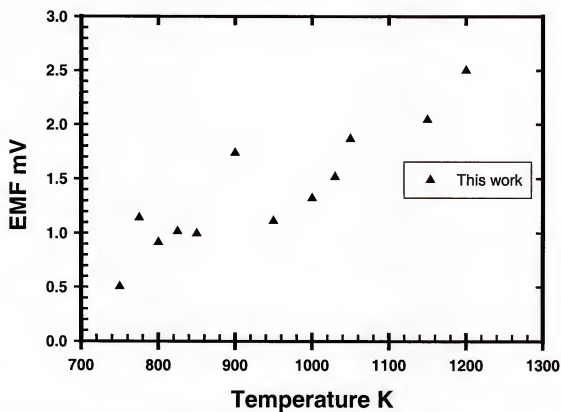

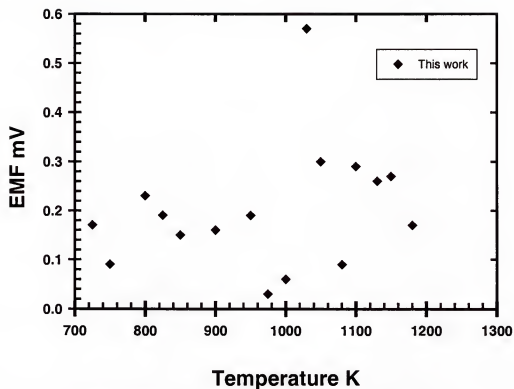Figure 7.6 EMF results of the liquid phase activity for 90 at. % Ga.

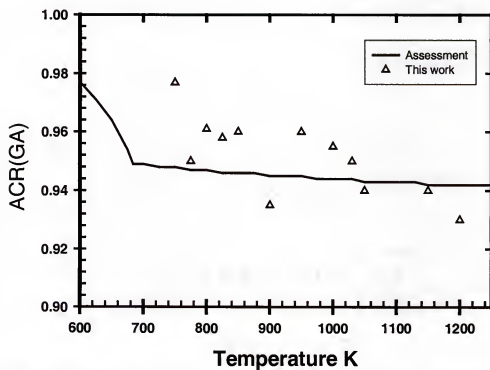Figure 7.7 EMF results of the liquid phase activity for 99 at. % Ga.

Figure 7.8 Comparison of measured Ga activity in the liquid phase with assessment by Subramanian [175] for 90 at. % Ga.
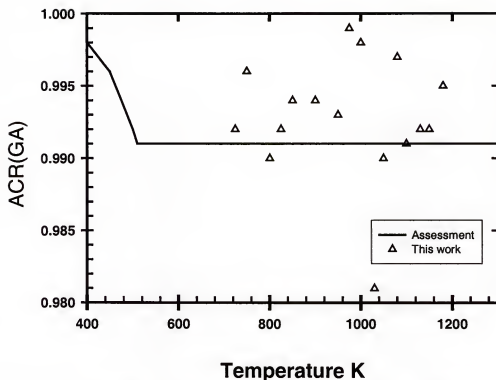
Temperature K

Figure 7.9 Comparison of measured Gallium activity in the liquid phase with assessment by Subramanian [175] for 99 at. %Ga.

Conclusion

Solid state EMF experiments were performed for selected compositions in the Cu-Ga-Se system. Experimental studies and literature data have been critically assessed and compared with a previous assessment of CuInSe$_2$ system. A comparison is made in Figure 7.4 on the Gibbs energy of formation functions of CuInSe$_2$ and CuGaSe$_2$. It was found that the standard molar entropy of formation values were of similar order. The nearly equal slopes of In and Ga ternaries can also be readily seen from Fig. 7.4. The ΔG^o_f values at 1000K showed that the ternary CuGaSe$_2$ compound is slightly more stable than the CuInSe$_2$ compound, which is consistent with the current phase diagram information.

A critical assessment of the phase diagram and thermodynamic data for the Cu-Ga binary system was also performed. The phase diagram and thermodynamic properties of Cu-Ga binary system have been critically assessed based on the available experimental and evaluated phase equilibrium and thermodynamic data. The recent phase diagram assessment by Subramanian [175] was taken as a starting model and his phase diagram was assumed directly. A EMF experiment was designed to measure liquid phase solution parameters. The liquid phase Ga activity for compositions of 60 at. %, 90 at. %, and 99 at. % Ga were measured. The measured activity data were compared with the current assessment results. The results of activity measurements given in Figures 7.7 and 7.9 reveal good agreement with the recent assessment by Subramanian [175]. Analogous to our ongoing effort to optimize ternary Cu-Ga-Se system and its binaries, the liquid solution model of Subramanian [175] was slightly altered to better represent complex behavior of liquid phase. A liquid model that originates from ionic solution theory that perfectly agrees with the results of Subramanian [175] was employed. The solution parameters and solution models optimized by Subramanian [175] adopted and the phase diagram was recalculated with new ionic model. The regular solution model was used by Subramanian [175] to describe the Gibbs energy of α-solid solution, β-Cu_3Ga, γ-Cu_2Ga, and ξ-Cu_7Ga_2 phases. For the β-Cu_3Ga, α-FCC and ξ-Cu_7Ga_2 phases, 2 coefficients were used. For the γ-Cu_2Ga defect compound, 3 coefficient model was applied. The new model for the liquid phase was described by a slightly different model that originates from the ionic sublattice model, which is schematically described as $(Cu^{+1}, Ga^{+3})_p (Va^{-4})_q$. The calculated phase diagram and thermodynamic data show reasonable agreement with the data available in the literature and our latest EMF results. Figure 7.4. shows the most

recent calculation of Cu-Ga phase diagram by combining the optimized solid solution parameters of Subramanian [175] and slightly altered new ionic liquid model.
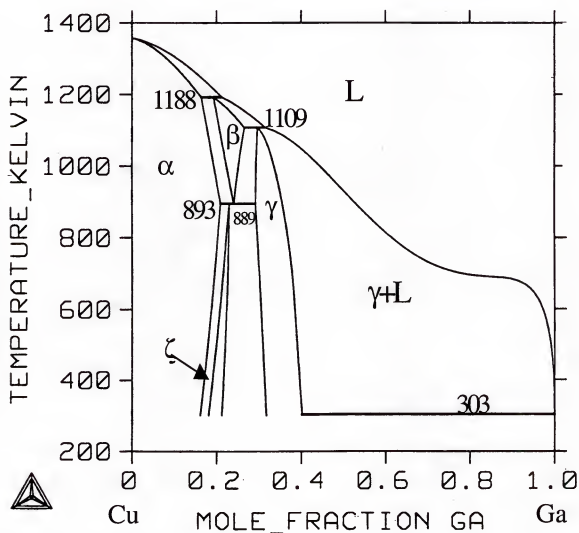

Figure 7.10 Calculated Cu-Ga binary phase diagram.

Table 7.7 Measured EMF data for 90 at. % Ga sample for cell II

Run	T (K)	E (mV)	T (K)	E (mV)
1	1200	2.50	900	1.74
	1150	2.04	850	1.00
	1050	1.87	825	1.02
	1030	1.52	800	0.91
	1000	1.32	775	1.14
	950	1.11	750	0.50

Table 7.8 Measured EMF data for 99 at. % Ga sample for cell II

Run	T (K)	E (mV)	T (K)	E (mV)
1	1180	0.17	975	0.03
	1150	0.27	950	0.19
	1130	0.26	900	0.16
	1100	0.29	850	0.15
	1080	0.09	825	0.19
	1050	0.30	800	0.23
	1030	0.57	750	0.09
	1000	0.06	725	0.17

REFERENCES

[1]   C.-H. Chang, Ph.D. Dissertation, University of Florida, Gainesville, FL 1999.

[2]   T. Godecke, T. Haalboum, and F. Ernst, *Zeitschrift fur Metallkunde*, vol. 91, pp. 651-662, 2000.

[3]   H. Okamoto, *Journal of Phase Equilibria*, vol. 12(6), pp. 702, 1991.

[4]   N. Saunders, A. P. Miodownik, *Calculation of Phase Diagrams (CALPHAD)* 1998.

[5]   L. Kaufman and H. Bernstein, *Computer Calculation of Phase Diagrams with Special Reference to Refractory Metals*, New York, 1970.

[6]   U. R. Kattner, *JOM*, vol. 49(12), pp. 14-19, 1997.

[7]   R. T. DeHoff, *Thermodynamics in Materials Science*, New York, 1993.

[8]   O. Redlich and A. T. Kister, *Industrial and Engineering Chemistry*, vol. 40, pp. 345-348, 1948.

[9]   R. A. Swalin, *Thermodynamics of solids*, 2d ed., New York: J. Wiley 1972.

[10] N. F. Mott, R. W. Guerney, *Electronic Processes in Ionic Crystals*, Clarendon Press, Oxford 1940.

[11] M. Hansen and K. Anderko, *Constitution of Binary Alloys*, New York: McGraw-Hill, pp. 582, New York, 1958.

[12] R.D. Heyding, *Can. J. Chem.*, vol. 44(10), pp. 1233-1236, 1966.

[13] R.M. Murray and R.D. Heyding, *Can. J. Chem.*, vol. 53, pp.878, 1975.

[14] G.P. Bernardini and A. Catani, *Miner. Deposita.*, vol. 3(4), pp. 375-380, 1968.

[15] G.P. Bernardini, F. Corsini, and R. Trosti, *Period. Miner.*, vol. 41(3), pp. 565-586, 1972.

[16] Z. Ogorelec, B. Mestnik, and D. Devcic, *J. Mater. Sci.*, vol. 7(8), pp. 967-969, 1972.

[17] B.P. Burylev, N.N. Fedorova and L. Sh. Tsemekhman, *Russ. J. Inorg. Chem.*, vol. 19(8), pp. 1249-1250, 1974.

[18]   A.A. Babitsyna, T.A. Emelyanova, M.A. Chernitsyna and V.T. Kalinnikov, *Russ. J. Inorg. Chem.*, vol. 20(11) pp. 1711-1713, 1975.

[19]   D. J. Chakrabarti and D.E. Laughlin, *Bulletin of Alloy Phase Diagrams*, vol. 2(3), pp. 305-315, 1981.

[20]   V.M. Glazov, A.S. Pashinkin, and V.A. Fedorov, *Inorganic Materials*, vol. 36(7), pp 641-652, 2000.

[21]   G. Sorokin, *Izv. Vyssh. Uchebn. Zaved. Fiz.*, vol. 6, pp. 158, 1961.

[22]   G.A. Efendiev, M. Ya. Bakirov, and E.S. Zaidova, *Inorg. Mater.*, vol. 5(8), pp. 1244-1245, 1969.

[23]   G.P. Sorokin, G.Z. Idrichan, L.V. Dergach, E.V. Kovtun and Z.M. Sorokina, *Inorg. Mater.*, vol. 10(b), pp. 834-838, 1974.

[24]   T.A. Bither, C.A. Prewitt, J.L. Gillson, P.E. Bierstedt, R.B. Flippen, and H.S. Yound, *Solid State Commun.*, vol. 4, pp. 533-535, 1966.

[25]   A. L. N. Stevels and J. Jellinek, *Rec. Trav. Chim.*, vol. 90, pp. 273-283, 1971.

[26]   W. Borchert and I. Patzak, *Heidelb. Beitr. Min. Petr.*, vol. 4, pp. 434-442, 1955.

[27]   A. D. Bugvava, A.P. Zhirnova, R.R. Shvangiradzc, and P.G. Yudin, *Izv. Akad. Nauk SSSR Neorg. Mater.*, 16(7), pp. 1292-1295, 1980.

[28]   V. N. Konev and V.A. Kudinova, *Inorg. Mater.*, vol. 9(7), pp. 1008-1011, 1973.

[29]   G. Lorenz and C. Wagner, *J. Chem. Phys.*, vol. 26, pp. 1607-1608, 1957.

[30]   M. Singh and S. Bhan, *Progress in Crystal Growth and Characterization*, vol. 20, pp. 217, 1990.

[31]   N. Frangis, C. Manolikas, and S. Amelinckx, *Phys. Stat. Sol.(a)*, vol. 126, pp. 9, 1991.

[32]   R.B. Shafizade, I. Ivanova and M. M. Kazinets, *Thin Solid Films*, vol. 55, pp. 211-220, 1978.

[33]   O. Milat, Z. Vucic and B. Ruscic, *Solid State Ionics*, vol. 23, pp. 37, 1987.

[34]   H. Rau and A. Rabenau, *J. Solid State Chemistry*, vol. 1, pp. 515-518, 1970.

[35]   T. J. Anderson, T.L. Aselage, and L.F. Donaghey, *J. Chem. Thermodyn.*, vol. 15, pp. 927-940, 1983.

[36]   I. Barin and O. Knacke, in *Thermochemical Properties of Inorganic Substances*, Springer-verlag, Berlin, 1973.

[37]   K. A. Askerova, N.A. Alieva, T. Rh. Azizov, A.S. Abbasov, and F.M. Mustafayev, *Izv. Akad. Nauk. Azerb. SSR*, vol. 6, pp. 137-139, 1976.

[38]   K. C. Mills, *Thermodynamic Data for Inorganic Sulphides, Selenides and Tellurides,* Butterworth, London 1974.

[39]   P. Rahlfs, *Z. Physik. Chem.*, vol. B31, pp. 157, 1936.

[40]   W. Borchert, *Z. Krist.*, vol. 106, pp. 5, 1945.

[41]   P. D. Heyding and R.M. Murray, *Can. J. Chem.*, vol. 54, 841, 1976.

[42]   A. Tonejc and A.M. Tonejc, *J. Sol. Stat. Chem.*, vol. 39, pp. 259, 1981.

[43]   M. Oliveria, R.K. McMullan, and B.J. Wuensch, *Sol. Stat. Ionic*, pp. 28-30, pp. 1332, 1988.

[44]   T. Sakuma, K. Sugiyama, E. Matsubara, and Y. Waseda, *Mater. Trans. JIM*, vol. 30(5), pp. 365, 1989.

[45]   K. Yamamoto and S. Kashida, *J. Sol. Stat. Chem.*, vol. 93, pp. 202, 1991.

[46]   Kovtun, and Z.M. Sorokina, *Izv. Akad. Nauk. SSSR Neorg. Mater.* vol. 10(6), pp. 969, 1974.

[47]   P. F. Pierret, *Semiconductor Device Fundamentals*, 1996.

[48]   M.Y. Rigan, V.I. Tkachenko, N.P. Stasyuk, and L.G. Novikova, *Inorganic Materials*, pp. 304, 1991.

[49]   L.A. Mechkovski, S.A. Alfer, I.V. Bodnar, and A.P. Bologa , *Thermochimica Acta*, 93, pp. 729, 1985.

[50]   S.H. Wei, L.G. Ferreira, and A. Zunger, *Physical Review*, vol. 45(5), pp. 2533, 1992.

[51]   L. Shay and J. H. Wernick, *Ternary Chalcopyrite Semiconductors*, Pergamon, Oxford, 1975.

[52]   M.L. Fearheiley, K. J. Bachman and C. A. Herrington, *J of Crystal Growth* submitted.

[53]   K.J. Bachmann, F.S.L. Hsu, F.A. Thiel, and H. M. Kasper, *J. Electro. Mater.*, vol. 6, pp. 431, 1977.

[54]   L. M. Khriplovich, I. E. Paukov, W. Moller, and Kuhn, *Russ. J. Phys. Chem.*, vol. 58, pp. 619, 1984.

[55]   Z. Range, *Naturforsch., B: Anorg. Chem*, vol. 23, pp. 1262, 1968.

[56]   M.F. Kotkata and M.S. Al-Kotb, *Proc. Of the Int`l Conf. on Cond. Matter. Phys.
       & Appl*, pp. 262-265, 1992.

[57]   L.S. Palatnik, E.I. Rogacheva, Izvestiya Akademii Nauk SSSR, *Neorganischke
       Materialy*, vol. 2(3), pp. 478-484, 1966.

[58]   H. Neumann, *Cryst. Res. Technol.*,vol. 29(7), pp. 985-994, 1994.

[59]   M.L. Fearheiley and K. J. Bachmann, *Journal of Electronic Materials*, vol. 14(6),
       1985.

[60]   H. Hahn, G. Frank, W. Klinger, A. D. Meyer, and G. Storger, *Z. Anorg. Allg.
       Chem.*, vol. 271, pp. 153, 1953.

[61]   H. Matsuhita, S. Endo, and T. Irie, *Japanese Journal of Applied Physics Part 1
       Regul Pap Short Note*, vol. 30(6), pp. 1181-1185, 1991.

[62]   M.F. Zargarova, P.K. Babaeva, D.S. Azhdarova, Z.D. Mekhtieva, and S.A.
       Mekhtieva, *Inorganic Materials*, vol. 32, pp. 282, 1995.

[63]   J. B. Mooney and R. H. Lamoreaux, *Solar Cells*, vol. 16, pp. 211, 1986.

[64]   R. H. Lamoreaux, K. H. Lau, and R. D. Brittain, "Final report," SERI Subcontract
       XZ-2-02001, 1983.

[65]   H. Neumann, *Crystal Res. Technol.*, vol. 18, pp. 665, 1983.

[66]   S. Nomura, H. Matsuhita and T. Takizawa, *Japanese Journal of Applied Physics*,
       vol. 30, pp. 3461-3464, 1991.

[67]   A. Rockett, R. W. Birkmire, *Journal of Applied Physics* 70 (7), 1991.

[68]   D. Cahen and R. Noufi, *J. Phys. Chem. Solids*, vol. 53, pp. 991-1005, 1992.

[69]   K.J. Bachmann, M.L. Fearheiley, and Y.H. Shing, *Tran, Appl. Phys.Letters*, vol.
       44, pp. 407, 1984.

[70]   J.C.W. Folmer, J.A. Turner, R. Noufi, and D. Cahen, *J. Electrochem. Soc.,* vol.
       132(6), pp. 1319, 1985.

[71]   M.L. Fearheiley, *Solar Cells*, vol. 16, pp. 91, 1986.

[72]   R. Lesuer, C. Djega-Mariadassau, P. Charpin, and J. H. Albany, *Inst. Phys. Conf.
       Ser.*, vol. 35, pp. 15, 1977.

[73]   L. S. Palatnik, Y. F. Komnik, and E. I. Rogacheva, *Ukr. Fiz. Zh.*, vol. 9, 862,
       1964.

[74] V. I. Tagirov, N. F. Gakhramanov, A. G. Guseinov, F. M. Aliev, and G. G. Guiseinov, *Sov. Phys. Semicond.*, vol. 14, pp. 831, 1980.

[75] C. Manolikas, J. van Landuyt, R. de Ridder, and S. Amelinckx, *Phys. Status Solidi A*, vol. 55, pp. 709, 1979.

[76] H. W. Schock, *Advances in Solid State Physics*, vol. 34, pp. 147-161, 1994.

[77] T. Hanada, A. Yamana, Y Nakamura and O. Nittono, *Technical Digest of the International PVSEC-9*, 1996.

[78] B. Schumann, G. Kuhn, U. Boehnke, and H Neels, *Sov. Phys. Crystallogr.*, vol.26(6), pp. 678, 1981.

[79] T.I. Koneshova, A.A. Babitsyna, and V.T. Kalinnikov, *Inorganic Materials*, vol. 18(9), pp. 1267, 1983.

[80] U.C. Boehnke and G. Kuhn, *J. Mater. Sci.*, vol. 22, pp. 1635, 1987.

[81] T. J. Anderson, and L.F. Donaghey, *J. Chem. Thermodyn.*, vol. 9, pp. 603, 1977.

[82] T. J. Anderson, T.L. Aselage, and L.F. Donaghey, *J. Chem. Thermodyn.*, vol. 15, pp. 927, 1983.

[83] Y. Feutelais, B. Legendre, S. Misra and T. J. Anderson, *Journal of Phase Equilibria*, vol. 15, pp. 171-177, 1994

[84] F. Sommer, *Zeitschrift fur Metallkunde*, vol. 73, pp. 72, 1982.

[85] Barin and O. Knacke, in *Thermochemical Properties of Inorganic Substances*, Springer-Verlag, Berlin, 1973.

[86] J.Y. Shen to be published Private Communication.

[87] L.S. Palatnik and E.I. Rogacheva, *Soviet Physics Doklady*, vol. 12, pp. 503, 1967.

[88] I.V. Bodnar and B.V. Korzun, *Mat. Res. Bull.*, vol. 18, pp. 519, 1983.

[89] L. Garbato, F. Ledda and A. Rucci, *Prog. Crystal Growth and Charact.*, vol. 15, pp. 1-41, 1987.

[90] S. H. Wei, Private Communication.

[91] C. H. Chang, Private Communication.

[92] C. Mallika, A. Davydov, C.H. Chang, and T.J. Anderson, *J. Chem. Thermodyn., (Communicated)*, 1998.

[93] D. Cahen and R. Noufi, *J. Phys. Chem. Solids*, vol. 52, pp. 947, 1991.

[94]   O. Redlich and A. Kister, *Ind. Eng. Chem.*, vol. 40, pp. 345, 1948.

[95]   Hillert, M.; Staffanson, L.I., *Acta Chim. Scand.*, 24, pp. 3618, 1970.

[96]   Sundman, B.; Agren, J., *J. Phys. Chem. Solids*, vol. 42, pp. 297, 1981.

[97]   M. Hillert and L.I. Staffanson, *Acta Chim. Scand.*, vol. 24, pp. 3618, 1970.

[98]   B. Sundman and J. Agren, *J. Phys. Chem. Solids*, vol. 42, 297, 1981.

[99]   L. I. Berger, S.A. Bondar, V.V. Lebedev, A.D. Molodyk, and S.S. Strel'chenko, *Nauka I Tekhnika*, pp.248, 1973.

[100]   V. M. Glazov, V. V. Lebedev, A. D. Molkyn, and A. S. Pashinkin, *Inorganic Materials*, vol. 15, pp. 1865, 1979.

[101]   E. Gombia, F. Leccabue, and C. Pelosi, *Mater. Lett.*, vol. 2, pp. 429, 1984.

[102]   K.J. Bachmann, H. Goslowsky, and S. Fiechter, *J. Cryst. Growth*, vol. 89, pp. 160, 1988.

[103]   J. Ward, K. Ramanathan, F. Hasoon, T. Coutts, J. Keane, T. Moriarity, and R. Noufi, *National Center for Photovoltaics Program Review Meeting*, 2001 (Lakewood, CO), pp. 14-17.

[104]   R. Ollitraut-Fichet, J. Rivet, and E. J. Flahaut, *Journal of Solid State Chemistry*, vol. 33, pp. 49-61, 1980.

[105]   H. Suzuki and R. Mori, *Japanese Journal of Applied Physics*, vol. 13, pp. 417-423, 1974.

[106]   J. Dieleman, F. H. M. Sanders, and J. H. J. Van Dommelen, *Philips J. Res.*, vol. 37, pp. 204-229, 1982.

[107]   J. Dieleman and A. R. C. Engelfriet, *Journal of the Less-Common Metals*, vol. 25, pp. 231-233, 1971.

[108]   P.G.M. Rustamov, B.K. Babaeva, and N.P. Luzhnaya, *Inorg. Mater.*, vol. 1, pp. 775, 1965.

[109]   K. A. Sharifov, T. Kh. Azizov, I. Ya. Aliev, and A. S. Abbasov, *Expanded Summary of Reports (in Russian)*, Sixth All Union Conf. On Calorimetry, Metsniereba, Tbilisi, , pp. 104, 1973.

[110]   A. P. Zefirov, *Thermodynamic Properties of Inorganic Substances (in Russian)*, Atomizdat, Moscow, 1965.

[111]   G. V. Naumov, B. N. Ryzhenkov, and I. L. Khodakovskii, *Hand book of Thermodynamic Values (in Russian)*, Atomizdat, Moscow, 1971.

[112] M. Kh. Karaapetyants and M.L. Karapetyants, *Principal Thermodynamic Constants of Inorganic and Organic Substances (in Russian)*, Khimiyn, Moscow 1968.

[113] B. P. Burylev, *Izv. Akad. Nauk. SSSR, Neorganicheskie Materialy*, vol. 13, pp. 919-920, 1977.

[114] J. C. Mikkelsen, Jr., *Journal of Electronic Materials*, vol. 10(3), pp. 541-558, 1981.

[115] N. C. Fernelius, *Prog. Crystal Growth and Charact.*, vol. 28, pp. 275-353, 1994.

[116] K. K. Mamedov, I. G. Kerimov, V. N. Kostryukov, and M. I. Mekhtiev, *Soviet Physics-Semiconductors*, vol. 1, pp. 441-442, 1967.

[117] S. Jandl and J. L. Brebner, B. M. Powell, *Physical Review B* , vol. 13, pp. 686-693, 1976.

[118] K. A. Sharifov and T. Kh. Azizov, *Russian Journal of Physical Chemistry*, vol.41, pp. 645, 1967.

[119] H. Hahn and F. Burow, *Angew. Chem.*, vol. 68, pp. 382, 1956.

[120] S. N. Gadzhiev and K. A. Sharifov, Collected Papers, *Voprosy Metallurgii i Fiziki Poluprovodnikov*, Moscow, pp. 43, 1961.

[121] J. C. Mikkelsen and G. B. Stringfellow, *Journal of Physical Chemistry of Solids*, vol. 44(12), pp. 1141-1145, 1985.

[122] D. Lübbers and V. Leute, *Journal of Solid State Chemistry*, vol. 43 pp. 339-345, 1982.

[123] P. C. Newman, *J. of Phys. Chem. Solid*, vol. 23, pp. 19, 1962.

[124] P. C. Newman, *J. of Phys. Chem. Solids*, vol. 24, pp. 45, 1963.

[125] A. Tonejc, S. Popovic and B. Grzeta-Plenkovic, *Journal of Applied Crystallography*, vol. 13, pp. 24-30, 1980.

[126] N. A. Goryunova, Slozhnie Almazopodobnie Poluprovodniki.: Sovetskoe radio, Moskva, 1968.

[127] J. F. Sanchez-Royo, D. Errandonea, and, A. Segura, *Journal of Applied Physics*, vol. 83, pp. 4750, 1998.

[128] M. Khalid Anis and A. R. Piercy, *Applied Physics*, vol. 17, pp. 1229-1232, 1984.

[129] R. Minder, G. Ottoviani, and C. Canali, *Journal of Physical Chemistry of Solids*, vol. 37, pp. 417-424, 1976.

[130] I. I. Dobynde, A. I. Bobrysheva, I. M. Razdobreev, and Y. G. Shekun, *Phys. Stat. Sol. (b)*, vol. 147, pp. 717, 1988.

[131] L. E. Ludviksson, J. W. Rumaner, Jr. Rogers, F. S. Ohuchi, *Journal of Crystal Growth*, vol. 151, pp. 114-120, 1995.

[132] S. Erkoc, K. Allahverdi, and Z. Ibrahim, Solid State Communications, vol. 90, pp. 553-556, 1994.

[133] O. Lang, A. Klein, C. Pettenkofer, and W. Jaegermann, *Journal of Applied Physics*, vol. 80, pp. 3817-3821, 1996.

[134] J. E. Palmer, T. Saitoh, T. Yodo, and M. Tamura, *Journal of Applied Physics*, vol. 74, pp. 7211-7222, 1993.

[135] L. Thanh Vinh, M. Eddrief, J. E. Mahan, A. Vantomme, J. H. Song, and M.-A. Nicolet, *Journal of Applied Physics*, vol. 81, pp. 7289-7294, 1997.

[136] S. Shigetomi, T. Ikari, and H. Nakashima, *Journal of Applied Physics*, vol. 76, 310-314, 1994.

[137] S. Shigetomi, T. Ikari, and H. Nakashima, *Journal of Applied Physics*, vol. 80, pp. 4779-4781, 1996.

[138] M. A. Hernandez, M. V. Andres, A. Segura, V. Munoz, *Optics Communications*, vol. 118, pp. 335-337, 1995.

[139] G. Micocci, A. Serra, and A. Tepore, *Journal of Applied Physics*, vol. 81, pp. 6200, 1997.

[140] G. Micocci, A. Serra, and A. Tepore, *Journal of Applied Physics*, vol. 82, pp. 2365-2369, 1997.

[141] B. Gurbulak, M. Yildirim, S. Tuzemen, H. Efeoglu, and Y. K. Yogurtcu, *Journal of Applied Physics*, vol. 83, pp. 2030, 1998.

[142] I. Barin and G. Platzki, *Thermochemical data of Pure Substances*, VCH Publishers, Inc., New York, Ny (USA), 1992.

[143] A. T. Dinsdale, *CALPHAD*, vol.15, pp. 317, 1991.

[144] I. Barin and G. Platzki, *Thermochemical Data of Pure Substances*, 3rd ed., Weinheim, 1995.

[145] K.C. Mills, *Thermodynamic Data for Inorganic Sulphides, Selenides and Tellurides*, Butterworth, London, 1974.

[146] M.Hillert and L.I.Staffanson, *Acta Chim. Scand.*, vol. 24, pp. 3618, 1970.

[147] B. Sundman and J.Agren, *J.Phys.Chem.Sol.*, vol. 42, pp. 297, 1981.

[148] I. Ansara, N. Dupin, H. L. Lukas, and B. Sundman, in *Applications of Thermodynamics in the Synthesis and Processing of Materials* , eds: P.Nash and B.Sundman , The Minerals, Metals & Materials Society, pp. 273, 1995.

[149] B. Sundman, B. Jansson, and J.O. Andersson, *CALPHAD*, vol. 9, pp. 153, 1985.

[150] P. de La Breteque, Gallium, *Bulletin d`Infornation et de Bibliographie*, Vol. 9, pp. A15 Alusuisse-France SA, 13 Marseille, 1970.

[151] Z. D. Ristovski and M. D. Dramicanin, *Applied Optics*, vol. 36, pp. 648-653, 1997.

[152] K. Schubert, E. Dorre, and J. M. Kluge, *Zeitschrift fur Metallkunde*, vol. 46, pp. 216, 1955.

[153] H. Hahn, *Angew. Chem.*, vol. 65, pp. 538, 1953.

[154] N. Goryunova and V. Grigoreva, *Soviet Physics-Tech. Phys. 1*, pp. 2094, 1956.

[155] H. Hahn and W. Klinger, *Z. Anorg. Chem.*, vol. 259, pp. 135, 1949.

[156] S. Popovic, B. Celustka, Z. Ruzic-Toros, and D. Broz, *Phys. Stat. Sol. (a)*, vol. 41, pp. 255-262, 1977.

[157] M. Y. Khan and S. Z. Ali, *J. Appl. Cryst.*, vol. 10, pp. 70-71, 1977.

[158] L. S. Palatnik and E. K. Belova, *Inorg.Mater.*, vol. 2, pp. 657, 1966.

[159] L. S. Palatnik and E. K. Belova, *Inorg.Mater.*, vol. 1, pp. 1703-1707, 1965.

[160] L. S. Palatnik. E. K. Belova, and A. A. Koz`ma, *Sov. Phys. Doklady*, vol. 9, pp. 1014-1017, 1965.

[161] J. C. Wooley and P. Keating, *J. Less-Common Metals*, vol. 3, pp. 194-201, 1961.

[162] G. Ghemard, R. Ollitraut-Fichet, and J. Flahaut, *Formes Desordonnees. Structure monoclinique.*, C. R. Acad. Sci. Paris 282C, pp. 831-834, 1976.

[163] J. L. Shay, B. Tell, H.M. Kasper, and L. M. Schiavone, *Physical Review*, B5, pp. 5003, 1972.

[164] L. L. Kazmerski, F.R. White and G.K. Morgan, *Appl. Phys. Letters*, vol. 29, pp. 268, 1976.

[165] L. S. Palatnik and E.K. Belova, *IZV. Akad. Nauk. SSSR. Neorgan. Mater.*, vol. 3, pp. 2194, 1967.

[166] I. V. Bodnar and A. P. Bologa, *Crystal Res. & Technology*, vol. 17, pp. 339-344, 1982.

[167] L. S. Palatnik, E.I. Rogacheva, Izvestiya Akademii Nauk SSSR, *Neorganischke Materialy*, vol. 2 , pp. 659, 1966.

[168] H. Jitsukawa, H. Matsushita, T. Takizawa, *Journal of Crystal Growth*, vol. 186, pp. 587-593, 1998.

[169] H. Matsushita, H. Jitsukawa, T. Takizawa, *Journal of Crystal Growth*, vol. 166, pp. 712-717, 1996.

[170] T. Tanaka, Y. Demizu, and A. Yoshida, *Journal of Applied Physics*, vol. 81(11), pp. 7619-7622, 1997.

[171] D. J. Schroeder, J. L. Hernandez, G. D. Berry, and A. Rockett, *Journal of Applied Physics*, vol. 83(3), pp. 1519-1526, 1998.

[172] T. J. Anderson and L.F. Donaghey, *J. Chem. Thermodyn.*, vol. 9, pp. 603-615, 1977.

[173] J. C. Phillips and J. A. Van Vechten, *Phys. Review*, vol. B2, pp. 2147, 1970.

[174] J. E. Kittl and T. B. Massalski, *J. Inst. Materials*, vol. 93, pp.182, 1964.

[175] P. R. Subramanian, T. B. Massalski, and D. E. Laughlin, *Acta Metall.*, vol. 36(4), pp. 937-943, 1987.

[176] B. Predel and D. W. Stein, *Acta Metall*, vol. 20, pp. 515, 1972.

[177] B. Predel and U. Schallner, *Zeitschrift fur Metallkunde*, vol. 63, pp. 119, 1972.

[178] K. Sugiyama, K. Mori, M. Tajima, and H. Miyake, *Journal of Crystal Growth*, vol. 118, pp. 41-48, 1992.

[179] S. N.Gadzhiev and K.A.Sharifov, *Dokl. Akad. Nauk SSSR*, vol. 136, pp. 1339, 1961.

[180] K. Mitchell, C. Eberspacher, J. Ermer, and D. Pier, in *Conf. Rec. 20th IEEE PVSC, IEEE , NY.*, pp. 1384, 1988.

[181] C.H. Chang, A. Davydov, B. J. Stanbery and T.J. Anderson, 25th Photovoltaic Specialists Conf., Washington, D.C., pp. 849, 1996.

[182] K.D. Becker, and S. Wagner, *Physical Review B*, vol. 27(a), pp. 5240, 1983.

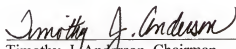[183] O. Kubaschewskii and C. B. Alcock, *Metallurgical Thermochemistry*, 5th ed., 1979.

[184]   H. Neumann, *Solar Cells*, vol. 16, pp. 399, 1986.

[185]   D. Cahen and Y. Mirovsky, *J. Phys. Chem.*, vol. 89, pp. 2818, 1985.

[186]   K. C. Mills, *Thermodynamic data for inorganic sulphides, selenides and Tellurides*, Butterworths, London, 1974.

[187]   G. P. Vassilev, B. Daouchi, M. C. Record and J. C. Tedenac, 1997, Private Communication.

[188]   R. Pankajavalli, M. Ider, B.J. Stanbery and T.J. Anderson (Private Communication)

[189]   T. Mayer, A. Klein, O. Lang, C. Pettenkofer, and W. Jaegermann, *Surface Science*, vol. 269/270, pp. 909-914, 1992.

[190]   M. C. Kuchta and G. Parkin, *Inorganic Chemistry*, vol. 36, pp. 2492-2493, 1997.

[191]   É. G. Zhukov and S. A. Dembovskii, *Izv. Akad. Nauk. SSSR, Neorganicheskie Materialy*, vol. 16, pp. 37-41, 1980.

[192]   H. J. Moore, D. L. Olson, and R. Noufi, *Journal of Electronic Materials*, vol. 27, pp. 1334-1340, 1998.

[193]   T. Wadsten, *Thermochimica Acta*, vol. 29, pp. 261-264, 1979.

[194]   O. M. Uy, D. W. Muenow, P. J. Ficalora, and J. L. Margrave, *Trans. Far. Soc.*, vol. 64, pp. 2998-3005, 1968.

[195]   K. K. Mamedov, M. A. Aldzhanov, I. G. Kerimov, V. N. Kostryukov, and M. I. Mekhtiev, *Soviet Physics-Solid State*, vol. 20, pp. 22-25, 1978.

[196]   J. C. Mikkelsen, Jr., *J. Solid State Chemistry*, vol. 40, pp. 312, 1981.

[197]   L.-Bornstein, *Numerical Data and Functional relationships in Science and Technology*, Eds. K.K. Hellwege and O. Madelung, Vol. 2, Springer-Verlag, Berlin, pp. 525, 1983.

[198]   J. J. Van Laar, *Z. Phys. Chem.*, 63, 216-253, 1908.

[199]   G. Sorokin, Y. Pashev and P. Oush, *Sov. Phys. Solid St.*, vol. 7, pp. 1810-1811, 1965.

[200]   G. Gattow and A. Schneidener, *Z. Anorg. Allgem. Chem.*, vol. 286, pp. 296-306, 1956.

[201]   K. G. Skeoch and R.D. Heyding, *Can. J. Chem.*, vol. 51, pp. 1235-1238, 1973.

[202]   J. B. Wagner and C. Wagner, *J. Chem. Phys.*, vol. 26, pp. 1602-1606, 1957.

[203] V. Piacente & P. Scardala, *J. of Mater Sci. Lett.*, vol. 13(18), pp. 1343-1345, 1994.

[204] P. R. Subramanian, and D. E. Laughlin, Bulletin of Alloy Phase Diagrams,, vol. 10(5), pp. 554-568, 1989.

[205] T. Godecke, T. Haalboum, and F. Ernst, *Zeitschrift fur Metallkunde*, vol. 91, pp. 622-634, 2000.

[206] T. Godecke, T. Haalboum, and F. Ernst, *Zeitschrift fur Metallkunde*, vol. 91, pp. 635-650, 2000.

Muhsin Ider was born in Ankara, Turkey, on March 17, 1971. He received his B.S. Degree from the Department of Chemical Engineering, Hacettepe University in 1993. He pursued his undergraduate project under Tulin Kutsal in the biochemistry lab in metal ion treatment of industrial wastes by using micro-organisms. He worked as graduate teaching assistant at the same department between 1993 and 1995. He studied the mathematical modeling of a membrane separation process by perva-poration method. He won a scholarship from the Ministry of Education of Turkey in 1995 for graduate studies in the United States. He studied English between 1995 and 1996 at Middle East Technical University. He started his graduate study in 1996 at the University of Florida. He joined Dr. Tim Anderson`s group in December 1996 and began his graduate research in thermochemistry and EMF measurements in Cu-In-Ga-Se system. He is interested in phase diagrams of compound semiconductors, solar cells and fuel cell technology. He will join the Chemical Engineering faculty at Kocatepe University in Afyon upon completion of this dissertation.

I certify that I have read this study and that in my opinion it conforms to acceptable standards of scholarly presentation and is fully adequate, in scope and quality, as a dissertation for the degree of Doctor of Philosophy.

Timothy, J. Anderson, Chairman
Professor of Chemical Engineering

I certify that I have read this study and that in my opinion it conforms to acceptable standards of scholarly presentation and is fully adequate, in scope and quality, as a dissertation for the degree of Doctor of Philosophy.

Oscar. D. Crisalle
Associate Professor of Chemical
 Engineering

I certify that I have read this study and that in my opinion it conforms to acceptable standards of scholarly presentation and is fully adequate, in scope and quality, as a dissertation for the degree of Doctor of Philosophy.

Fan Ren
Professor of Chemical Engineering

I certify that I have read this study and that in my opinion it conforms to acceptable standards of scholarly presentation and is fully adequate, in scope and quality, as a dissertation for the degree of Doctor of Philosophy.

Robert. T. DeHoff
Associate Professor of Materials Science
 and Engineering

This dissertation was submitted to the Graduate Faculty of the College of Engineering and to the Graduate School and was accepted as partial fulfillment of the requirements for the degree of Doctor of Philosophy.

May 2003

Pramod P. Khargonekar
Dean, College of Engineering

Winfred M. Phillips
Dean, Graduate School